State-Dependent Diffusion of Brownian Particles Near a Boundary Wall

by

Mpumelelo Matse

B.Sc., University of Swaziland, 2012
PgDip., African Institute for Mathematical Sciences, 2013

Thesis Submitted in Partial Fulfillment
of the Requirements for the Degree of

Master of Science

in the
Department of Physics
Faculty of Science

SIMON FRASER UNIVERSITY
Fall 2015

APPROVAL

Name: Mpumelelo Matse

Degree: Master of Science
(Physics)

Title of Thesis: *State-Dependent Diffusion of Brownian Particles Near a Boundary Wall*

Examining Committee:

Chair: Eldon Emberly (Associate Professor)

John Bechhoefer
Senior Supervisor
Professor

David Sivak
Supervisor
Assistant Professor

Barbara Frisken
Internal Examiner
Professor

Date Defended: 16 December 2015

ABSTRACT

Brownian motion refers to the erratic random movement of microscopic particles suspended in a fluid. In a simple fluid, Brownian motion exhibits two key properties: the mean-squared displacement (MSD) increases linearly with time (the proportionality constant is the diffusivity D) and the displacement distribution is Gaussian. Although a linear MSD was initially assumed to always imply Gaussian displacements, recent experiments show that non-Gaussian displacements can coexist with a linear MSD in complex environments. Chubynsky et al. [PRL **113**, 098302, 2014] have argued that such behavior arises when D has temporal and/or spatial fluctuations that are convolved together and form a non-Gaussian distribution. Experiments to date have been in complex settings where direct measurements of $D(x,t)$ have not been possible. Here, we report experiments on a simple system where $D(x,t)$ is known: the Brownian motion of a colloidal sphere near a boundary wall. By choosing the particle size carefully, we ensure that the bead explores a wide range of D. We observe a linear MSD curve and non-Gaussian displacements for vertical motion and directly confirm the proposed mechanism of Chubynsky et al. for such "diffusing diffusivity."

Keywords: diffusivity, diffusing-diffusivity, mean-squared displacements, non-Gaussian

DEDICATION

To God and my mother!

ACKNOWLEDGEMENTS

This thesis, the result of a period of labour and patience, would not be what it is today without the involvement of all of those who, in a way or another, contributed their valuable assistance to lead it to the end. First and foremost, I offer my thanks to Almighty God, who offered me protection and good health throughout the thesis. I am also very grateful to my supervisor Professor John Bechhoefer who, despite the multiple duties, dedicated his time providing corrections to this thesis. He has been a constant source of encouragement and enthusiasm during my research. In my daily work, I have been blessed with a friendly and cheerful group of fellow students. Special thanks go to Momčilo Gavrilov, who constantly assisted me with my experiments, and Paul Omelchenko, who introduced me to the experiment setup I started developing. Finally, I acknowledge SFU and NSERC for financial support.

Contents

List of Tables

List of Figures

Chapter 1

Introduction

In this work, we study the statistical properties of a Brownian colloidal sphere near a flat wall. Our goal is to explore experimentally, in a simple setting, the consequences of a fluctuating diffusion constant. Brownian diffusion is a basic model in soft matter and biophysics. Historically, "Brownian motion" refers to the inherent, incessant motion of microscopic particles of matter when suspended in a fluid, a phenomenon first given serious consideration by the Scottish botanist Robert Brown in 1827 [1]. Using a microscope, Brown was investigating the fertilization process in plants when he noticed a "rapid oscillatory motion" of microscopic particles within the pollen grains suspended in water under the microscope. Such motions had been observed prior to Brown but only in organic molecules, and their origin was credited to some mysterious force that was characteristic of living matter. Brown was the first to show that the problem was one of physics, not biology, since he verified that the diffusion did not arise from the living origin of the particles. Brown tried many particles, even "a fragment of the Sphinx" [1]. Upon this discovery, he reported,

> "While examining the form of these particles immersed in water, I observed many of them very evidently in motion...These motions were such as to satisfy me, after frequently repeated observation, that they arose neither from currents of the fluid, nor from its gradual evaporation, but belonged to the particle itself." (Brown 1828)

By the late 19th century, interest in Brownian motion grew among theoretical and experimental physicists, who searched for a consistent explanation of its various characteristics. In 1905, Albert Einstein, driven by a desire to show that the physics of statistical fluctuations supports the atomic hypothesis of matter, gave an illuminating quantitative theory of Brownian motion. In his first Brownian-motion paper, *On the motion of particles suspended in a resting fluid demanded by the molecular theory of heat*, he wrote [2]

"It is possible that the movements to be discussed here are identical with the so-called 'Brownian molecular motion'; However, the information available to me regarding the latter is so lacking in precision, that I can form no judgment in the matter.". (Einstein 1906)

Einstein's theory of Brownian motion inspired experimental work by Jean Perrin in 1908 that provided estimates of Avogadro's number [3]. Perrin's work quickly convinced the remaining skeptics of the concept of the atomic hypothesis, and he received the Nobel Prize in Physics in 1926. After Einstein's 1905–1906 papers, theoretical and experimental work on Brownian motion advanced rapidly. We summarize four key characteristics of Brownian motion found in the work pioneered by Einstein and von Smoluchowski [4]:

(I) *Thermal origin and stochastic nature of the motion*

Einstein proposed that Brownian diffusion results from the quasi-random, microscopic interactions of the suspended particle with thermally excited molecules forming the liquid. His results offered firm evidence for the atomistic hypothesis of matter and were supported by experimental work by Perrin [5]. From the equipartition theorem of statistical mechanics, the temperature T of a fluid is equal to the average kinetic energy of the constituent molecules. In three dimensions,

$$\frac{3}{2}\, k_B T \;=\; \frac{1}{2}\, m \,\langle v^2 \rangle \;, \tag{1.1}$$

where k_B is the Boltzmann constant, m the mass of the molecule, and v its speed. In thermal equilibrium, the molecules of the surrounding fluid are in spontaneous and continuous motion, with the typical "thermal velocity" $v_{\text{thermal}} = \sqrt{3k_BT/m}$. The observed Brownian diffusion therefore reflects thermal fluctuations that are observable at our scale [6]. The physical system can be viewed as "large molecules" in a solution, the large molecules being the Brownian or colloidal particles.

The minimum and maximum permissible sizes of the particle to be considered Brownian are not distinctly defined. For the minimum size, a Brownian particle should be significantly larger than the linear dimension of a solvent molecule, which is ≈ 1 nm. The upper limit to the size of a Brownian particle is set by the requirement that it exhibits measurable thermal motion. This implies a maximum size of $\approx 10\ \mu$m.

Owing to the very large number of solvent molecules in collision with each Brownian particle, Einstein realized that the theoretical analysis of Brownian motion should be based on probability theory. He assumed that the particle's position is a Markov process in time; i.e., it changes state according to a transition rule that depends only on the

current state. Brownian motion as a mathematical random process was first constructed rigorously by Norbert Wiener [7] in a series of papers starting in 1918. The stochastic description of Brownian diffusion processes was further developed by Langevin, Fokker, Planck, Klein, Uhlenbeck and Ornstein, and Kramers [8].

(II) *Self-similarity of the trajectories:* Brownian diffusion mechanism was found to generate fractal structures. This property of the trajectories was first observed in the experimental work of Perrin in 1913 [5]. Today, it is referred to as statistical *self-similarity*: if one studies the Brownian paths with a finer spatial resolution, they conserve the same appearance and statistical properties. This self-similarity comes from the microscopic origin of the movement: a displacement of the particle corresponds to a transient anisotropy in the variation of momentum due to the very large number of random collisions of the fluid molecules with the particle. This self-similarity property, therefore, holds at time scales longer than the collision time between the solvent molecules ($\approx 10^{-14}$ m). This also explained the failure in previous experimental attempts to determine the instantaneous velocity of the particles at time scales much longer than the time between collisions [8]. Perrin concluded that the instantaneous velocity was a badly defined observable because of its dependence on the scale at which the motion is analyzed [5, 8].

(III) *Mean-squared displacements that are linear in time:* Investigations of the particle trajectories from experiments reveal that the average displacement $\langle x(t) \rangle$ vanishes owing to isotropy of the overall random motion: Displacements in one direction happen as frequently as displacements in the opposite direction. In analyzing the properties of the motion, neither the displacement nor the velocity is of any use for its quantitative description. However, a third quantity, the mean-squared displacement (MSD) $\langle \Delta x^2(t) \rangle$, is a relevant observable. Einstein predicted, and then Perrin confirmed, that Brownian particles, at long times and for d spatial dimensions, obey the law

$$\langle \Delta x^2(t) \rangle = 2dD\Delta t \ , \tag{1.2}$$

indicating a linear relationship of the MSD with the elapsed time Δt. The proportionality constant D defines the *diffusivity* or the diffusion constant for the Brownian particle. Diffusion satisfying this proportionality law is called *normal diffusion*. The observation that the MSD increases linearly with time lag explained why the attempts to measure the velocity at diffusion time scales were unsuccessful: If this relationship holds down to very small time scales, then the particle path would be non-differentiable, and the velocity is not well-defined. Einstein later realized that, at the shortest time scales, the law of statistical independence of the displacements should break down [6]. Indeed recently, Raizen *et al.* [9, 10] measured the instantaneous velocity of a Brownian particle both

in a liquid and a gas at short time scales on the order of 10 ns. They succeeded in observing the instantaneous velocity of the particle and verified that the velocities obey the Maxwell-Boltzmann distribution.

(IV) *Gaussian distribution of displacements:* One important result from Einstein was that for the free diffusion of a Brownian particle in a homogeneous medium, the probability density of the displacements Δx is Gaussian. In one dimension,

$$P(\Delta x, \Delta t) = \frac{1}{\sqrt{4\pi D \Delta t}} \exp\left(-\frac{\Delta x^2}{4D\Delta t}\right) , \tag{1.3}$$

where Δt is the elapsed time. One can derive Eq. (1.3) using the statistical independence of the increments. Indeed, when Brownian paths are viewed as a succession of steps, the Central Limit Theorem implies that the long-time dynamics have to be Gaussian.

As we mentioned earlier, normal diffusion has the characteristic scaling $\langle r^2 \rangle \sim t$, with independent spatial increments. Recent experiments in non-homogeneous and complex systems [11, 12, 13], however, reveal deviations from normal diffusion, in that diffusion is either faster or slower than normal. Diffusion processes that scale as

$$\langle r^2 \rangle \sim t^\gamma, \quad \gamma \neq 1 , \tag{1.4}$$

are termed as *anomalous*. The scaling index γ classifies the diffusion as normal diffusion when $\gamma = 1$ and anomalous when $\gamma \neq 1$. The case $\gamma > 1$ defines super-diffusive processes, and the case $\gamma < 1$ defines sub-diffusive processes. Such an anomaly in the diffusion can be theoretically analyzed by treating the Brownian agent as a random walker. Anomalous diffusion can arise in several situations: divergence of the average duration of the time steps, infinite variance of the displacements and divergence of the correlation time. These scenarios led to the implementation of different models to explain anomalous diffusion [14, 15], all based on the random-walk description of Brownian motion.

A fascinating conclusion drawn from previous experiments is that the linearity of the MSD with time can be associated with Gaussian distribution of displacements. The initial assumption was that time-linear MSD always imply Gaussian distribution of displacements. However, recent experiments show that this is not always the case [16, 17, 18, 19, 20]. Granick and his group [18, 19] observed that the MSD can be *linear* even though the distribution is *non-Gaussian*. They considered a number of complex systems: colloidal beads on phospholipid bilayer tubes [18], colloidal beads in entangled actin suspensions [18], and liposomes in a nematic solution of aligned actin filaments [19]. In all three systems, the MSD was found to be precisely linear in the elapsed time over the experimental time range, $\Delta t \approx 1$ s to a few seconds. However, the displacements are non-Gaussian distributed for small Δt. For larger Δt, they smoothly revert

back to Gaussian. The non-Gaussian density functions typically have exponential tails whose decay lengths λ grow as $\sqrt{\Delta t}$. Very recent experiments by Bhattacharya et al. [21] observed similar behavior for diffusion of tracer molecules on polymer thin films and in simulations of a 2D system of discs. Another experiment from Granick's group [20] shows non-Gaussian diffusion in mixtures of hard spheres of different sizes. The general conclusion was that the nature of the displacement distribution does not completely determine the MSD.

A recent paper by Chubynsky and Slater [22] describes such *anomalous yet Brownian* diffusion behavior in terms of a *diffusing diffusivity* model. They proposed that such diffusion anomalies arise in heterogeneous systems where the environment of the diffusing particles changes slowly in space and time. An example of such a situation is one where the diffusivity has temporal and/or spatial fluctuations. A suitable system is one in which the environment gradually changes in space and time, so that $D = D(\mathbf{r}, t)$. Over length and time scales smaller than those of these heterogeneities, the local environment is described by an approximately constant diffusivity characterized by locally Gaussian dynamics. Over long time and length scales, non-Gaussian diffusion results from the convolution of these localized Gaussian, independently diffusive processes. This approach corresponds to breaking down complex processes into diffusive processes, each described by a constant diffusivity [18]. Hence, the distribution of diffusivities will determine the shape of the non-Gaussian distribution curves. By the Central Limit Theorem, the distribution should revert back to a Gaussian at times much greater than the correlation time of the fluctuations of the diffusivity. In previous experiments, the fluctuations in D that drive this diffusing-diffusivity mechanism are unknown.

In this thesis, I pose the following question:

> "*Can this non-Gaussian yet normal diffusion be experimentally observed in a simpler system where the complexity comes from known fluctuations in the diffusivity?*"

Let us consider a simple system characterized by a space-dependent diffusivity, the Brownian motion of a colloidal sphere near a flat rigid wall. For this system, theoretical and experimental studies [23, 24, 25] have shown that the diffusivity decreases anisotropically with distance from the wall, owing to the alteration of the hydrodynamic interaction between the sphere and the fluid generated by the wall's boundary conditions [24]. Our goal is to investigate, theoretically and experimentally, the dynamics of this wall-hindered diffusion system and to explore the emergence of non-Gaussian diffusion. We first explore this system theoretically to study the statistical properties of the displacement distribution curves at different time scales and search for experimental parameters that reveal non-Gaussian dynamics driven by complexity due to diffusivity fluctuations only, coexisting with time-linear MSD. We then study the system experimentally, for the setting of near-wall motion of a Brownian bead in water under the influence of gravity and electrostatic double-layer forces.

The chapters of the thesis are organized as follows: Chapter 2 serves as a concise theoretical background relevant to the work. Chapter 3 discusses the wall-hindered diffusion system and the simulations of the system, which provide guidelines for the choice of experimental parameters that bring about fascinating properties of space-dependent diffusion. Chapter 4 focuses on the second part of my research, the implementation of the experimental technique for studying the system. Finally, in Chapter 5, we conclude with a summary and outlook.

Chapter 2

Theoretical Background

There are several approaches to understanding the underlying mathematical concepts of Brownian diffusion, as described in Chapter 1. The choice of approach one employs depends on the system being analyzed and the goals of the investigation. For this study, we adopt both the Langevin and Fokker-Planck approaches to study Brownian motion near a wall. Our discussion will focus on describing individual spherical Brownian particles. Because of their experimentally accessible time and length scales, hard-sphere colloids are an ideal model system to study nonlinear behaviors in far-from-equilibrium systems [8].

This chapter is organized into four sections: Section 2.1 introduces the Langevin equation concept. The interactions of a colloidal sphere with a rigid wall is considered in Sec. 2.2. In Sec. 2.3, we discuss the modified overdamped Langevin equation describing the motion of a Brownian sphere close to the wall. Section 2.4 introduces the Fokker-Planck equation as a tool to gain insight into the *diffusing-diffusivity* dynamics of the particle.

2.1 Langevin equation

2.1.1 General Langevin equation

For a single free Brownian particle, Langevin started from the equation of motion given by Newton's second law, assuming that the particle experiences two forces from the surrounding solvent molecules:

(i) Viscous drag $-\gamma v$: the deterministic force coming from hydrodynamic friction. Here, v is the velocity and γ is coefficient of friction governed by Stokes' law [2]; i.e., $\gamma = 6\pi\eta a$, for a sphere of radius a in a fluid with dynamic viscosity η.

(ii) Rapidly fluctuating force $\xi(t)$: the thermal *noise* that causes random motions of the suspended particle due to the thermal impacts of the liquid molecules on the particle.

This is the residual force exerted by the heat bath after the frictional force has been subtracted.

The resulting equation of motion for a mass m diffusing in an unbounded fluid medium in one dimension reads

$$m\frac{d^2x(t)}{dt^2} \;=\; -\gamma\frac{dx(t)}{dt} \;+\; F_{\rm ext} \;+\; \xi(t)\;, \tag{2.1}$$

where $F_{\rm ext}$ includes any other external forces. Equation (2.1) is called a *stochastic differential equation* reflecting the presence of the stochastic noise term. To determine the trajectories from Eq. (2.1), we need to know the statistical properties of the noise ξ.

Owing to the large number of independent collisions of different fluid molecules on the particle, the resulting random force is equally likely to push in one direction as in the other. The average over all realizations of the force thus vanishes:

$$\langle\xi\rangle = 0\;. \tag{2.2}$$

Here, $\langle\cdot\rangle$ denotes the ensemble average.

Time scales considered in the study of Brownian motion are set by the resolution of the experiment or theory, and observables are averaged over the time intervals that set the time scale. The smallest time scale considered is the collision time between the solvent molecules, $\tau_{\rm solvent}$. This solvent time scale is $\approx 10^{-14}$ s for a latex sphere of radius 1 μm. The Langevin equation, together with the statistical properties of the random force, is valid on time intervals much greater than $\tau_{\rm solvent}$. It is essential also to specify the relevant time scales for the hydrodynamic regime of the translating sphere. We consider the momentum relaxation time τ_m, the characteristic time taken by the Brownian sphere to lose its perturbed momentum arising from thermal fluctuations. In the absence of external forces, the equation of motion for the translating sphere with mass m and friction coefficient γ reads

$$m\dot{v} - \gamma v = 0\;, \tag{2.3}$$

implying the momentum relaxation time

$$\tau_m = \frac{m}{\gamma}\;. \tag{2.4}$$

In terms of the particle size a and mass density ρ, and the fluid's viscosity η, the momentum relaxation time is

$$\tau_m = \frac{\frac{4}{3}\pi\rho a^3}{6\pi\eta a} = \frac{2}{9}\frac{\rho}{\eta}\,a^2\;. \tag{2.5}$$

For a colloidal latex sphere, diffusing in water, with size in the range $a = 0.1$–10 μm, the momentum relaxation time falls in the range $\tau_m \approx 10^{-10}$–10^{-6} s. The average $\langle \xi(t)\xi(t')\rangle$ at two distinct times t and t' vanishes if the time differences $|t-t'|$ are larger than τ_{solvent}. The shortest time scale considered for Brownian diffusion of colloidal particles is τ_m. Since $\tau_{\text{solvent}} \ll \tau_m$, it is a reasonable approximation to take the limit $\tau_{\text{solvent}} \to 0$. This gives the time-correlation function

$$\langle \xi(t)\xi(t')\rangle = q\delta(t-t') \,, \tag{2.6}$$

where q is the measure of the strength of the fluctuation force and is referred to as the *fluctuation strength*. The delta (δ) function forces the average energy of the colloidal particle to be finite, as required by the equipartition law [26]. By the fluctuation-dissipation theorem [26], the fluctuation strength is given by

$$q = 2D\gamma^2 \,. \tag{2.7}$$

We have introduced the diffusion constant, or *diffusivity*,

$$D = \frac{k_B T}{\gamma} = \frac{k_B T}{6\pi\eta a} \,, \tag{2.8}$$

where η is the fluid dynamic viscosity and a is the particle radius. Equation (2.8) is the famous *Stokes-Einstein relation* for a translating sphere in an infinite fluid medium [2].

2.1.2 Overdamped Langevin equation

We define the third significant time scale for our system, the characteristic *diffusion time scale*

$$\tau_a = \frac{a^2}{6D} = \frac{\pi\eta}{k_B T}\, a^3 \,, \tag{2.9}$$

which is the time taken by the particle to diffuse a distance equal to its radius a. We rescale time, velocity, and the stochastic and external forces as

$$t' = \frac{t}{\tau_a}, \quad v' = \frac{\tau_a}{a}\, v, \quad \xi' = \frac{1}{\gamma}\frac{\tau_a}{a}\xi \,, \quad F'_{\text{ext}} = \frac{1}{\gamma}\frac{\tau_a}{a}F_{\text{ext}} \,, \tag{2.10}$$

respectively. The Langevin Eq. (2.1) then transforms to

$$\left(\frac{\tau_m}{\tau_a}\right)\, \frac{dv'}{dt'} \;=\; -v' \;+\; \xi' \;+\; F'_{\text{ext}} \,. \tag{2.11}$$

We have just expressed the time and position in new units corresponding to the minimum resolution for the coarsened description of the system. For a typical colloid of size $a \approx 0.1-1$ μm translating in water, τ_a falls within the range $\tau \approx 10^{-3}$–10^{0} s. Since $\tau_m \ll \tau_a$, the inertial term on the left-hand-side of the Langevin Eq. (2.1) can be set to zero in the diffusion time scale,

which defines the overdamped limit. The diffusive dynamics is then described by the *overdamped Langevin equation*,

$$0 \;=\; -\gamma \frac{dx}{dt} \;+\; F_{\text{ext}} \;+\; \xi \;. \tag{2.12}$$

Below, in Sec. 2.3.1, we will see that we must be careful in dropping the inertial term. The latter constitutes a *singular* perturbation and accounting for its effects, even when small, can sometimes be important.

2.2 Near-wall effects

In this work, we explore the Brownian motion of a single colloidal sphere near a flat wall, as shown in Fig. 2.1. Examples of compact, rigid spheres investigated in experiments include polystyrene (latex) and amorphous silica particles. If the colloidal sphere diffuses close to a rigid planar wall, the drag due to fluid viscosity increases, and its diffusion constant consequently decreases. The corrections to the sphere diffusivity due to the alteration of the hydrodynamics and the sphere-wall interactions will be considered below.

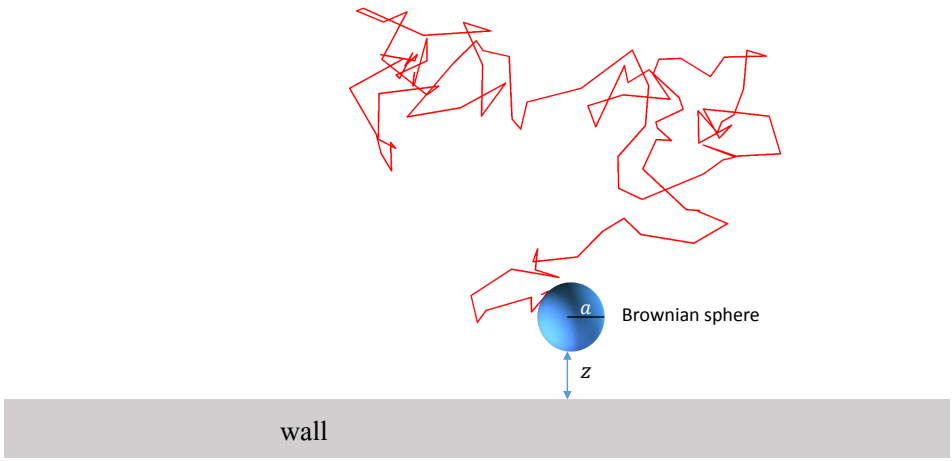

Figure 2.1: Brownian sphere diffusing at a height z above a rigid wall.

2.2.1 Hindered Diffusion

For a freely diffusing Brownian sphere in an unbounded fluid medium, the diffusion coefficient is given by Eq. (2.8). When the sphere diffuses near a planar wall, diffusion is hindered. This effect has been studied by several groups theoretically and experimentally [23, 27, 28]. As the particle diffuses towards the wall, its diffusivity D is reduced and becomes anisotropic.

These effects can be understood by considering the Navier-Stokes flow u of the fluid around

the sphere and the *no-slip boundary condition*, which states that at a solid boundary, the fluid will have zero velocity relative to the boundary. In this situation, the no-slip boundary condition is applied at the surface of the sphere, i.e., $u = u_{\text{sphere}}$, and the solution to the Navier Stokes Equation leads to the drag force $F_0 = 6\pi\eta a u$ [24]. However, there is an additional no-slip

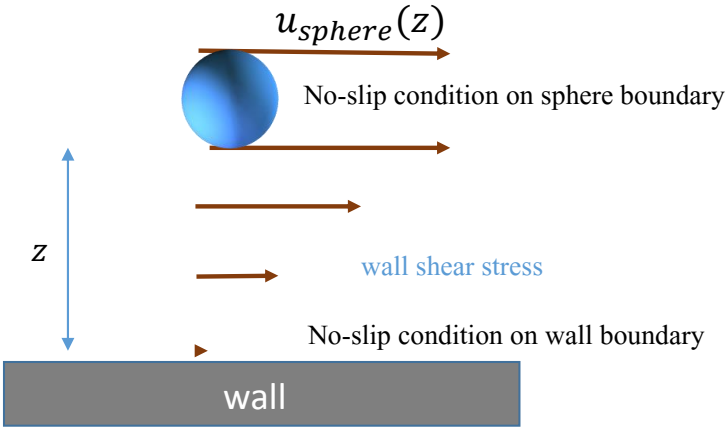

Figure 2.2: Typical flow on the surface of the sphere u_{sphere} with reference to a wall.

condition imposed by the wall, which alters F_0 appreciably when the sphere diffuses close to the wall. For this case, the flow around the sphere, with reference to the wall, is shown in Fig. 2.2. The flow profile decreases towards the wall, and it vanishes at the wall. Hence, the presence of the wall introduces the shear force

$$F \propto \eta \frac{\partial u}{\partial z} \tag{2.13}$$

because of the development of near-wall velocity gradients. Owing to the no-slip condition on the surface of the sphere, the drag force will increase inversely with distance towards the wall as a result of additional hydrodynamic pressure arising from these velocity gradients. The particle then experiences a local drag force that depends on both the distance z from the wall and the direction of motion, and its diffusion is hindered.

We can separate the drag force into independent components for motion parallel and perpendicular to the wall, thanks to the linearity of the Navier-Stokes equations. We express the drag force as a function of the height z from the wall,

$$F_D^{\parallel}(z) = \frac{F_0}{\lambda_{\parallel}(z)}; \qquad \text{and} \qquad F_D^{\perp}(z) = \frac{F_0}{\lambda_{\perp}(z)}, \tag{2.14}$$

where $\lambda_{\parallel}$ and $\lambda_{\perp}$ are, respectively, dimensionless z-dependent parallel and perpendicular correction factors to the drag force due to the presence of the wall. In other words, the diffusion

coefficients for parallel and perpendicular motion relative to the wall are

$$D_{\parallel}(z) \;=\; D_0\,\lambda_{\parallel}(z) \qquad \text{and} \qquad D_{\perp}(z) \;=\; D_0\,\lambda_{\perp}(z)\,, \tag{2.15}$$

where D_0 is diffusion constant far away from the wall. Generally, the wall-hindered drag forces given in Eqs. (2.14) are difficult to solve. There is an exact series solution for $\lambda_{\perp}$, found by Brenner [24]:

$$\lambda_{\perp}^{-1} = \frac{4}{3}\sinh[\alpha]\sum_{n=1}^{\infty}\frac{n(n+1)}{(2n-1)(2n+3)}\left[\frac{2\sinh[(n+1)\alpha]+(2n+1)\sinh[\alpha]}{4\sinh^2[(n+1/2)\alpha]-(2n+1)^2\sinh^2[2\alpha]}-1\right], \tag{2.16}$$

where $\alpha = \cosh^{-1}(z/a)$, with z the distance from the wall to the bottom of the sphere. A useful second-order Pade approximation to Eq. (2.16) is [29]

$$\lambda_{\perp}(z) \;=\; \frac{6z^2+2az}{6z^2+9az+2a^2}\,. \tag{2.17}$$

The most commonly used representations of $\lambda_{\parallel}$ are all approximate. The representations are derived via the *method of reflections*, an iterative series-solution technique that decomposes the velocity and the pressure fields into a linear superposition of terms of successively higher order in the number of wall and sphere boundary interactions. In this method, it is assumed that the motion of the Brownian sphere near a wall induces a pressure and velocity distribution in the adjacent fluid. The terms in the expansion are constrained to alternately satisfy the boundary conditions on both the sphere and the wall. The solutions for the parallel correction factor obtained with this method are usually expressed as a power series in $a/(a+z)$. Using this method, one finds [24]

$$\lambda_{\parallel}(z) \cong 1-\frac{9}{16}\left(\frac{a}{a+z}\right)+\frac{1}{8}\left(\frac{a}{a+z}\right)^3-\frac{45}{256}\left(\frac{a}{a+z}\right)^4-\frac{1}{16}\left(\frac{a}{a+z}\right)^5+\mathcal{O}\left(\frac{a}{a+z}\right)^6. \tag{2.18}$$

Plots of the parallel and perpendicular diffusivity of the sphere with height from the wall are shown in Fig. 2.3. The diffusivity is significantly reduced at heights on the order of the particle's radius. For the investigations reported in this thesis, the most important feature of Fig. 2.3 is that $D_{\perp}(z\to 0)=0$, whereas $D_{\parallel}(z\to 0)\approx 0.3\,D_0$.

2.2.2 Sphere-wall interactions

In order to understand the near-wall dynamics of the Brownian particle, we need to study the external forces that act on it. In our system, these forces come from the interaction of the sphere with the wall and from the gravitational field. There are several well-developed theories that describe the interactions in such colloidal systems. Moreover, there are accurate direct measurements of the forces acting between the particles as a function of the surface separation

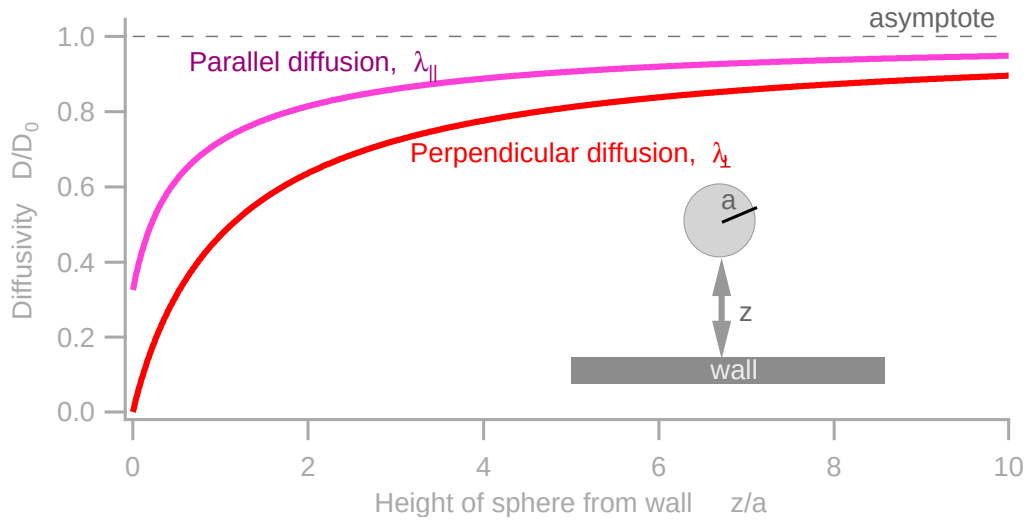

Figure 2.3: Anisotropic corrections to the diffusivity.

in liquids [28]. In this work, we assume that the Brownian sphere does not interact with other Brownian spheres. This is the case for very dilute suspensions.

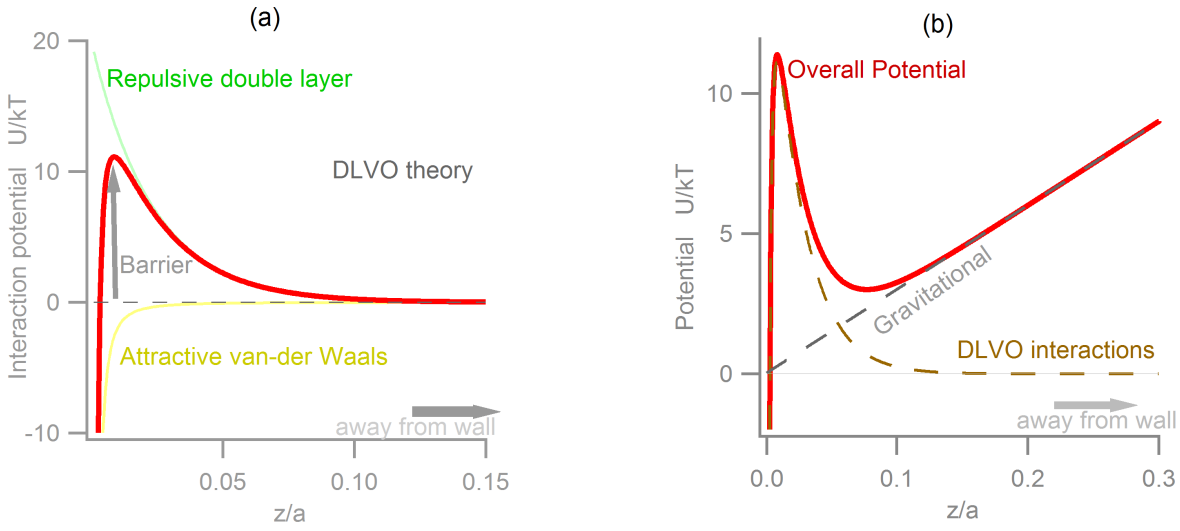

Figure 2.4: Sphere potential energy due to the wall and gravity. (a) Attractive van der Waals potential and the repulsive double-layer potentials come from the wall. (b) The gravitational potential is included. All these interactions act in the direction perpendicular to the wall.

Our description of the wall interactions are obtained from the DLVO theory, a theory named after Derjaguin, Landau, Verwey, and Overbeek [30], which assumes that the forces between two surfaces separated by the liquid arise from two main contributions: the attractive van der Waals forces and the repulsive electrical double-layer forces, as shown in Fig. 2.4(a). Besides the

electrostatic and van der Waals interactions, other "non-DLVO" forces in a solvent are present. They become important at very small distances to the wall. In our study, these short-range forces are not relevant because the particle never gets close enough to the wall to be affected by them. In addition to the DLVO forces, the gravitational forces also affect the particle's dynamics. We next consider each one the the interactions.

Double-layer forces

The surface of the colloidal particle and the wall in a liquid may carry ionized chemical groups, leading to repulsive double-layer forces. The repulsive electrostatic double-layer forces prevent the Brownian particles from sticking to each other and to the surface of the wall.

Surface charges can originate from different mechanisms, such as ionization of surface groups, specific adsorption of ions from solution onto a previously uncharged surface, or isomorphic substitutions. Since the system is electrically neutral as a whole, the fluid must contain an equivalent charge of the opposite sign. When the wall or sphere surface is negatively charged, free negatively charged ions are released from the fluid close to the surface, while positive ions are attracted towards the surface. Consequently, a double-layer charge distribution forms near the surface (see Fig. 2.5). It should be noted that the resulting double-layer interaction potential

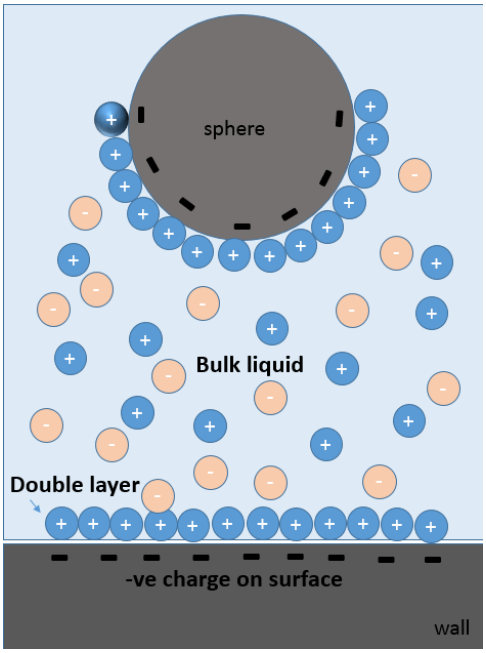

Figure 2.5: A Brownian sphere immersed in the liquid is surrounded by an electric double layer. The same applies to the wall. One of the double layers is formed by the charge that accumulates at the surface of the particles. Another layer is formed by the excess of oppositely charged ions in the solution. The charge density decreases gradually with increasing distance into the bulk liquid phase.

is not a Coulomb repulsion (which goes as $1/z$) but is screened by the free ions in the fluid. Its approximate form is [30]

$$U_{\rm dl} \;=\; B\, e^{-z/\lambda_D}\;, \tag{2.19}$$

where l_D is the *Debye length*, which measures the effectiveness of the screening – the extent of double-layer interaction effects. The Debye length is given by

$$l_D \;=\; \sqrt{\frac{\varepsilon\varepsilon_0 k_B T}{2\cdot N_A e^2 I}}\;, \tag{2.20}$$

with N_A the Avogadro number, e the elemental electric charge, ε the dielectric permittivity of the solvent, ε_0 the relative dielectric permittivity of free space. Also, I is the ionic concentration of the solvent, given by $I = \frac{1}{2}\sum_i c_i Z_i^2$, where c_i is the molecular concentration and Z_i the valence of ion i. Screening is more efficient (i.e., l_D becomes smaller) for larger concentrations of free ions in the solvent. Adding salt, for example, can reduce the double-layer repulsion. The prefactor B measures the strength of the double-layer potential and is given by

$$B = 16\varepsilon a \left(\frac{k_B T}{e}\right)^2 \tanh\left(\frac{e\psi_1}{4k_B T}\right)\tanh\left(\frac{e\psi_2}{4k_B T}\right)\;, \tag{2.21}$$

where ψ_1 and ψ_2 are the Stern potentials of the substrate surface and the particle surface, respectively. Typically, $B \approx 10$–$50\ k_B T$ [30].

Van der Waals forces

Van der Waals forces between two molecules include three different contributions: the force between two permanent dipoles (*Keesom orientation force*), the force between a polar and a non-polar molecule (*Debye induction force*), and the *dispersion force* or *induced dipole-dipole force*, which acts between all atoms and molecules, including neutral ones. These forces are very short ranged and are usually attractive. They can be screened by longer-ranged, repulsive double-layer forces coming from the charges on the surfaces. For near-wall diffusion experiments, one can add salt to the fluid to reduce the Debye length and bring the sphere closer to the wall. However, this can lead to van der Waals interactions between the particles and the wall (the particles stick to the wall), and coagulation of the particles (the particles stick to each other), a situation that can be inhibited by steric stabilization [30].

Gravitational Interaction

In addition to the sphere-wall interactions already mentioned, the sphere diffuses under the influence of the gravitational potential

$$U_{\rm g} \;=\; \Delta mgz \;=\; \frac{4}{3}\pi\Delta\rho g a^3 z\;, \tag{2.22}$$

where $\Delta\rho$ is the mass density difference between the fluid and the sphere. We define the *gravitational decay length*,

$$l_g = \frac{k_B T}{\Delta m g} \;=\; \frac{3k_B T}{4\pi\Delta\rho g a^3}\;, \tag{2.23}$$

as the typical distance moved by the particle due to the gravitational potential against the thermal forces. For $l_g \gg a$, the particle does not feel the gravitational force. In the system we study, we require that the particle size be of the order of the decay length. This ensures that gravity is strong enough that the particle stays close to the wall, yet weak enough that it explore an interesting range of distances from the wall. We, therefore, use gravity to position the particle with respect to the horizontal wall.

The overall potential, including gravitation interaction, is illustrated in Fig. 2.4(b). It is given by

$$U(z) = U_{\rm vdw} \;+\; U_{\rm dl} \;+\; U_{\rm g}\;. \tag{2.24}$$

Clearly, close to the wall, the gravitational forces can be neglected and the DLVO theory can correctly describe the physics of the system. At distances far away from the wall ($z/a > 0.1$ in Fig. 2.4), DLVO forces can be neglected, and the particle feels only the gravitational force. In later discussion, we will ignore van der Waals forces since they are very short-ranged (order of a few nanometers) and, they are masked by the longer-ranged double-layer forces (effective to about 50 – 100 nm in our experiments).

2.3 Langevin equation for wall-hindered diffusion

Having determined the external forces acting on the particle, we revisit the Langevin formulation (Eq. 2.12) of the system's dynamics. We integrate the one-dimensional, overdamped Langevin equation over a time Δt,

$$\Delta x_i \;=\; -\frac{1}{\gamma(z)}\,\frac{\partial U(z)}{\partial x_i}\Delta t \;+\; \sqrt{2D(z)\Delta t}\,\xi_R\;, \tag{2.25}$$

where Δx_i and Δt are the space and time increments, respectively. Here, x_i refers to any of the rectangular coordinates (x, y, z), and ξ_R is a Gaussian random variable satisfying $\langle\xi_R\rangle = 0$ and $\langle\xi_R^2\rangle = 1$, with no correlation between different time intervals. The function $D(z)$ represents

the height-dependent diffusivity, parallel or perpendicular according to the displacements being considered. The particle diffuses freely along x and y, but there are external forces along z that come from the repulsive double-layer and gravitational potentials discussed earlier. As discussed in Sec 2.2.2, we neglect the van der Waals forces. Hence,

$$U(z) \;=\; Be^{-z/l_D} + \frac{4}{3}\pi\Delta\rho g a^3 z\,; \qquad D(z) = D_{\parallel,\perp}(z), \tag{2.26}$$

with all parameters explained previously. The wall is assumed to be located at $z = 0$.

2.3.1 Noise-induced drift

In the absence of external forces, the overdamped Langevin equation reduces to

$$\Delta x_i \;=\; \int_{t_0}^{t_0+\Delta t} \sqrt{2D(z)}\,\xi(t')\,dt'\,. \tag{2.27}$$

The space dependence of the diffusion coefficient introduces multiplicative noise for displacements in the direction direction normal to the wall: Since the noise term is not a well-defined function, Eq. (2.27), as it stands, is meaningless unless one specifies the time at which the noise strength $\sqrt{2D(z)}$ should be evaluated during the integration of Eq. (2.27) over the time interval $[t_0, t_0 + \Delta t]$. The physics depends on the noise calculus employed, and the requirement that the long-time thermal equilibrium be consistent with the Boltzmann distribution places an additional constraint on the Langevin equation.

The diffusion coefficient appearing in Eq. (2.25) can generally be represented by $D(z+\alpha\Delta z)$ [equivalently, $D(z(t_0 + \alpha\Delta t))$], for some $\alpha \in [0, 1]$. The value of α chosen determines the time at which the noise term is evaluated within the interval $[t_0, t_0 + \Delta t_0]$ [31, 32]. One has to decide which value of α should be employed in order to specify completely the Langevin equation. If we ignore the external forces, the perpendicular equation becomes

$$\Delta z \;=\; \sqrt{2D(z + \alpha\Delta z)\Delta t}\,\xi_R\,. \tag{2.28}$$

Expanding the diffusion coefficient to first order, we get

$$D(z + \alpha\Delta z) \;\approx\; D(z) + \alpha\frac{dD}{dz}\Delta z + \mathcal{O}(\Delta z^2)\,. \tag{2.29}$$

Substituting this into Eq. (2.28) gives

$$\begin{aligned}
\Delta z \;&\approx\; \sqrt{2\left[D(z)+\alpha\frac{dD}{dz}\Delta z\right]\Delta t}\,\xi_R \;=\; \xi_R\,\sqrt{2D(z)\Delta t}\left(1+\alpha\,\frac{dD}{dz}\frac{\Delta z}{D(z)}\right)^{\frac{1}{2}} \\
&\approx \xi_R\,\sqrt{2D(z)\Delta t}\left(1+\frac{\alpha}{2}\frac{dD}{dz}\frac{\Delta z}{D(z)}\right) \\
&= \xi_R\,\sqrt{2D(z)\Delta t}\left(1+\frac{\alpha}{2}\frac{dD}{dz}\,\frac{\left[\xi_R\sqrt{2D(z)\Delta t}+\mathcal{O}(\Delta t^1)\right]}{D(z)}\right) \\
&= \sqrt{2D(z)\Delta t}\,\xi_R \;+\; \xi_R^2\alpha\,\frac{dD}{dz}\Delta t \;+\; \mathcal{O}(\Delta t^{\frac{3}{2}}).
\end{aligned} \tag{2.30}$$

Taking $\Delta t = N\delta t$, where δt is some smaller time displacement satisfying the last line of Eq. (2.30), we note that the fluctuation term is negligible for $\delta t \to 0$. Hence, within the time interval Δt, we can replace ξ_R^2 with its average value 1 so that the full overdamped Langevin equation for perpendicular motion becomes

$$\Delta z = \alpha\,\frac{dD}{dz}\Delta t \;-\frac{\Delta t}{\gamma(z)}\,\frac{\partial U(z)}{\partial z} \;+\; \sqrt{2D(z)\Delta t}\,\xi_R\,. \tag{2.31}$$

The additional α term is deterministic and implies a drift of the Brownian particle in the direction of the diffusivity gradient. The drift is known as *spurious flow, spurious drift,* or *noise-induced drift*. The resulting noise-induced drift velocity,

$$v_{\rm ni} \;=\; \alpha\,\frac{dD}{dz}\,, \tag{2.32}$$

is expected to vanish when $\alpha = 0$. It also vanishes for horizontal diffusion, since $D_\parallel$ is independent of x and y. Different values of α lead to different solutions to Eq. (2.31). Three values have been most commonly adopted: the Itô ($\alpha = 0$), Stratonovich ($\alpha = 1/2$), and isothermal ($\alpha = 1$) conventions [33]. Although any value of α is mathematically admissible, it still remains controversial what value of α is physically more meaningful than others. The isothermal convention is appropriate for the system we are studying, since it is consistent with the equilibrium Boltzmann distribution. However, theoretical investigations reveal that starting from the underdamped Langevin equation leads naturally to the Stratonovich convention, with a drift term to be consistent with the Boltzmann distribution in equilibrium [34, 35].

The overall drift v_d in the particle's perpendicular motions comes from two contributions: noise-induced drift due to the variation in D, given in Eq. 2.32, and drift due to the external field,

$$v_d(z) \;=\; \alpha\,\frac{dD_\perp(z)}{dz} - \frac{1}{\gamma(z)}\,\frac{\partial U(z)}{\partial z}\,. \tag{2.33}$$

Hence, perpendicular motion can be presented in the compact form

$$\Delta z = v_d \Delta t \; + \; \sqrt{2D_\perp(z)\Delta t}\, \xi_R \; . \tag{2.34}$$

From now on, we will examine the perpendicular (z) dynamical equations only. Lateral (x and y) equations can be determined from the z equations by setting $v_d = 0$ and using the appropriate space-dependent diffusivity ($D_\parallel$ instead of $D_\perp$).

2.3.2 Deterministic vs. diffusive motion

The first term on the right-hand side of Eq. (2.34) leads to deterministic motion, and the last term gives rise to random motion. Equation (2.34) suggests that the noise term ($\sim \sqrt{\Delta t}$) dominates the deterministic contribution ($\sim \Delta t$) at very small time steps. The balance between these two regimes can be set by the two time scales: the one-dimensional diffusion time scale

$$\tau_{\rm a} \; = \; \frac{a^2}{2D} \; , \tag{2.35}$$

is the typical time for a particle to diffuse over a distance comparable to its own radius. The drift time scale,

$$\tau_{\rm drift} \; = \; \frac{a}{v_d} \; , \tag{2.36}$$

is the corresponding time for deterministic forces. Here, we assume that all the other length scales (l_D and l_g) are of the same order of magnitude. A standard measure of the relative importance of deterministic vs. random motion is the *Péclet number*,

$$\mathrm{Pe} \; \equiv \; \frac{\tau_{\rm a}}{\tau_{\rm drift}} \; = \; \frac{v_d a}{2D} \; . \tag{2.37}$$

Setting $D = k_B T/\gamma$, we can express the Péclet number as

$$\mathrm{Pe} \; \sim \; \frac{\gamma v_d a}{k_B T} \; , \tag{2.38}$$

which is the ratio of the work needed to drive the particle a distance a by the deterministic forces against the thermal energy. For $\mathrm{Pe} \ll 1$, the particle undergoes free Brownian motion in the normal direction, just as in parallel motion, and the drift term can be neglected in the Langevin equation (2.34). For $\mathrm{Pe} \gg 1$, the motion is deterministic, and Brownian motion can be neglected. The Péclet number will take different values for different heights of the bead.

2.4 Fokker-Planck equation

The motion of the Brownian particle can alternatively be described by the *Fokker-Planck equation*, which considers the time evolution of the particle distribution function $P(z,t)$. Instead of calculating explicit trajectories of the Brownian particle by solving the Langevin equation, we can determine the probability density $P(z,t)$ of finding the particle at a certain position z at time t, given initial conditions. The probability density is defined such that $P(z,t)\ dz$ is the probability that the position lies within the interval $[z,\ z+dz]$ at time t. The time evolution of $P(z,t)$ obeys the Fokker-Planck equation [33],

$$\frac{\partial P(z,t)}{\partial t} \ = \ -\frac{\partial}{\partial z}\left\{v_d(z)P(z,t)\right\} \ + \ \frac{\partial^2}{\partial z^2}\left\{D(z)P(z,t)\right\}. \tag{2.39}$$

The stationary solution to Eq. (2.39), found by setting $\partial_t P = 0$, is the Boltzmann distribution,

$$P_B(z) \ = \ \frac{1}{\mathcal{Z}} \ \exp\left(-\frac{U(z)}{k_BT}\right) = \ \frac{1}{\mathcal{Z}} \ \exp\left(-\frac{B}{k_BT}\ e^{-\frac{z}{l_D}} \ - \ \frac{z}{l_g}\right). \tag{2.40}$$

Here, $1/\mathcal{Z}$ is the normalization constant. From the integral formula [36]

$$\int_0^\infty \exp\left(-\beta e^{-x} - \mu x\right) dx \ = \ \beta^{-\mu}\gamma(\mu,\ \beta)\ , \tag{2.41}$$

with γ the lower incomplete gamma function [36], the normalization constant is

$$\mathcal{Z} \ = \ l_D \ \left[\frac{B}{k_BT}\right]^{-l_D/l_g} \gamma\left(\frac{l_D}{l_g},\ \frac{B}{k_BT}\right). \tag{2.42}$$

If the particle starts at $(z,t) = (z_0,t_0)$, then the initial condition for the density function is

$$P(z,t_0) \ = \ \delta(z-z_0)\ . \tag{2.43}$$

Since the drift v_d and diffusivity D are independent of time, Eq. (2.39) can be formulated as

$$\frac{\partial P(z,t)}{\partial t} = \mathcal{L}_{\rm FP}(z)\ P(z,t)\ , \tag{2.44}$$

where $\mathcal{L}_{\rm FP}$ is the time-independent Fokker-Planck operator, given by

$$\mathcal{L}_{\rm FP} \ = \ -\frac{\partial}{\partial z}\ v_d(z) \ + \ \frac{\partial^2}{\partial z^2}\ D(z)\ . \tag{2.45}$$

The formal solution to Eq. (2.44), with initial condition Eq. (2.43), is then

$$\begin{aligned} P(z,t|z_0,t_0) &= e^{\mathcal{L}_{\rm FP}(z)(t-t_0)}\ \delta(z-z_0) \\ &= \exp\left[-\frac{\partial}{\partial z}\ v_d(z)\ (t-t_0)\ +\ \frac{\partial^2}{\partial z^2}\ D(z)\ (t-t_0)\right]\ \delta(z-z_0)\ . \end{aligned} \tag{2.46}$$

2.4.1 Conditional displacements for small times

It is hard to find the exact solutions to Eq. (2.46), since the drift and the diffusivity both depend on the particle's height from the wall. In the following, we consider the case where the time $\Delta t = (t - t_0)$ is small enough that the drift and the diffusivity are approximately constant. Such a requirement for Δt depends on z since the drift and the diffusivity vary more or less sharply at different heights.

For sufficiently small Δt, the drift and diffusivity are roughly constant, and we can represent D and v_d as functions of the initial position, z_0, instead of z. Representing the δ function appearing in Eq. (2.46) as a Fourier integral, we obtain, for small Δt,

$$\begin{aligned} P(z,\Delta t|z_0) &= \exp\left[-\frac{\partial}{\partial z}\ v_d(z_0)\ \Delta t\ +\ \frac{\partial^2}{\partial z^2}\ D(z_0)\ \Delta t\right]\ \frac{1}{2\pi}\int_{-\infty}^{\infty} e^{iu(z-z_0)}\ du \\ &= \frac{1}{2\pi}\int_{-\infty}^{\infty} \exp\left[-v_d(z_0)\Delta t\ \frac{\partial}{\partial z}\ e^{iu(z-z_0)}\ +\ D(z_0)\Delta t\ \frac{\partial^2}{\partial z^2}\ e^{iu(z-z_0)}\right] \\ &= \frac{1}{2\pi}\int_{-\infty}^{\infty} \exp\left[-iu\ v_d(z_0)\Delta t\ - u^2 D(z_0)\Delta t + iu(z-z_0)\right]\ du\ . \end{aligned} \tag{2.47}$$

After a long exercise of calculus, the above reduces to [26]

$$P(\Delta z,\Delta t|z_0)\ =\ \frac{1}{\sqrt{4\pi D(z_0)\Delta t}}\ \exp\left(-\frac{[\Delta z - v_d(z_0)\Delta t]^2}{4D(z_0)\Delta t}\right)\ , \tag{2.48}$$

where $\Delta z = (z - z_0)$ is the z displacement. This is just what we might expect: a Gaussian distribution with mean $\mu(z_0) = v_d(z_0)\Delta t$ and variance $\sigma^2(z_0) = 2D(z_0)\Delta t$. For lateral motion, characterized by $v_d = 0$, we have $\mu = 0$. Therefore, the presence of the external field and noise-induced drift along z introduces asymmetry about $\langle \Delta z \rangle = 0$ in the vertical displacement distribution which vanishes with the time scale Δt. Indeed, Mauricio et al. [37] observed this asymmetry for colloidal particles close to a plane wall. The height-conditional n-th moments

of the displacements can be shown to be [26]

$$\mu^n(z_0) = \langle (\Delta z)^n | z_0 \rangle \;=\; \left[-i\sqrt{D(z_0)} \right]^n \;\times\; \mathrm{H}_n \left[\frac{1}{2} i \; v_d(z_0) \sqrt{\frac{\Delta t}{D(z_0)}} \right] \;, \tag{2.49}$$

where $\mathrm{H}_n(x)$ are the Hermite Polynomials (H_0=1, $\mathrm{H}_1 = 2x$, $\mathrm{H}_2 = 4x^2 - 2$, ...). The first four moments (conditional on z_0) are

$$\langle \Delta z | z_0 \rangle \;=\; v_d \Delta t \;, \tag{2.50a}$$

$$\langle \Delta z^2 | z_0 \rangle \;=\; 2D\Delta t \;+\; v_d^2 \Delta t^2 \;, \tag{2.50b}$$

$$\langle \Delta z^3 | z_0 \rangle \;=\; 6 v_d D \Delta t^2 \;+\; v_d^3 \Delta t^3 \;, \tag{2.50c}$$

$$\langle \Delta z^4 | z_0 \rangle \;=\; 12 v_d^2 D \Delta t^3 \;+\; 12 D^2 \Delta t^2 \;+\; v_d^4 \Delta t^4 \,, \tag{2.50d}$$

and variations $D(z)$ are slow enough. As long as $\Delta t \ll 2D/v_d^2$, the mean-squared displacement will be linear with time, and perpendicular diffusion will be free of the bounding forces, just as for parallel diffusion.

2.4.2 Diffusing diffusivity

Our interest in this work is to study the behavior of the overall diffusion of the particle. Instead of considering the small-time conditional displacements probability density $P(\Delta z, \Delta t | z_0)$, we examine the overall density $P(\Delta z, \Delta t)$ which considers all possible initial states of the system. From the law of conditional probability, the overall probability density takes the form

$$P(\Delta z, \Delta t) \;=\; \int_0^\infty P(\Delta z, \Delta t | z_0) \; P_B(z_0) \; dz_0 \;. \tag{2.51}$$

which is a sum of the Gaussian distributions $P(\Delta z, \Delta t | z_0)$ [given by Eq. (2.48)] over all the possible initial states z_0 weighted by the Boltzmann distribution $P_B(z)$. To gain an intuitive understanding of the properties of the overall displacement density function given in Eqn. (2.51), we analyze its alternative formulation in terms of the fluctuations in diffusivity:

$$P(\Delta z, \Delta t) \;=\; \int_{D_{\min}}^{D_{\max}} P(\Delta z, \; \Delta t \; | D) \; P(D) \; dD \;. \tag{2.52}$$

This form comes from the transformation relation $P_B(z_0) \; dz_0 = P(D) \; dD$, where $P(D)$ is the distribution of the particle's diffusivities over its motion. In this form, we can interpret the

system's overall diffusion as a sum of the very-short-time (Δt) Gaussian diffusion processes each identified by its diffusion constant (dependent on z_0), or variance. We expect the resulting displacements to be non-Gaussian.

At larger time scales, or at Pe $\gg 1$, the bounding potential along z also leads to different dynamics and (2.52) does not hold. The overall distribution is the convolution of two Boltzmann distributions, since the displacement $\Delta z = (z_1 - z_0)$ comes from independent draws from the Boltzmann distribution, i.e.,

$$\begin{aligned} P(\Delta z, \Delta t) &= \int_{-\infty}^{\infty}\int_{-\infty}^{\infty} dz_0\, dz_1\, P(\Delta z, z_0, z_1) \\ &= \int_{-\infty}^{\infty}\int_{-\infty}^{\infty} dz_0\, dz_1\, P(\Delta z|z_0, z_1)\, P_B(z_0)\, P_B(z_1) \\ &= \int_{-\infty}^{\infty}\int_{-\infty}^{\infty} dz_0\, dz_1\, \delta(\Delta z + z_0 - z_1)\, P_B(z_0)\, P_B(z_1) \\ &= \int_{-\infty}^{\infty} dz_0\, P_B(z_0)\, P_B(z_0 + \Delta z) \\ &= \int_{-\infty}^{\infty} dz_0\, P_B(z_0)\, P_B(z_0 - \Delta z)\,. \end{aligned} \tag{2.53}$$

The last line arises from the symmetry $P(\Delta z, \Delta t) = P(-\Delta z, \Delta t)$, which can be demonstrated by changing variables to $z = z_0 - \Delta z$ in the integral. For the bounding potential in the system we study, Eq. (2.53) is clearly non-Gaussian. If we consider only the gravitational potential, then P_B is an exponential distribution and $P(\Delta z,\ \Delta t)$ is a Laplace (bi-exponential) distribution (see Fig. 2.6). The mean-squared displacement, on the other hand, must remain linear in time as long as the Péclet number is very small. The typical displacement is taken from the sum of many random variables each taken from a Gaussian distribution, irrespective of how the diffusivities vary in space. In the next chapter, we will investigate the statistical properties of the displacements in more detail.

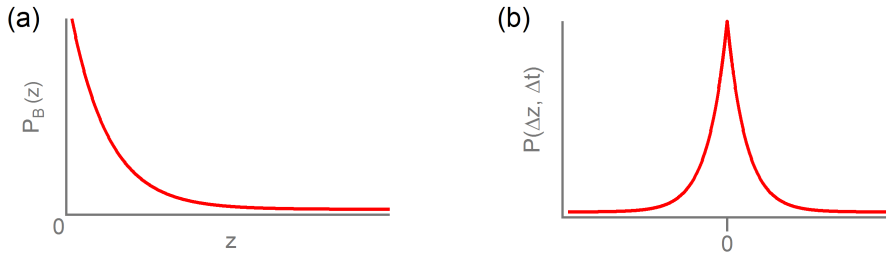

Figure 2.6: (a) Form of the Boltzmann distribution assuming a gravitational potential only. (b) The long-time stationary bi-exponential (Laplace) distribution of displacements.

Chapter 3

Computer Simulations of Brownian Diffusion Near a Wall

In this chapter, we explore numerically the dynamics of a colloidal sphere diffusing near a flat wall using the tools presented in the previous chapter. We investigate the effects of the wall and the gravitational interactions on its hindered diffusion dynamics. The results obtained are guidelines for the near-wall Brownian diffusion experiments reported in Chapter 4. Our main aim is to determine a set of experimental parameters that lead to non-Gaussian displacement distributions of the particle due to fluctuations in the diffusivity.

This chapter is organized as follows: Section 3.1 introduces the Brownian dynamics simulation algorithm used to find the bead's trajectory. In Sec. 3.3, the effect of the time intervals on the dynamics is considered, and the solutions of the Fokker-Planck equation for small time intervals is presented in Sec. 3.2. In Sec. 3.4, we investigate the effect of the particle's vertical confinement on the dynamics at very short time scales, when the displacements are not affected by the bounding potential.

3.1 Brownian dynamics simulation

We first study the characteristics of the particle's trajectory by solving the Langevin equation numerically for perpendicular and parallel motion.

3.1.1 Brownian dynamics

In Brownian dynamics simulations, particle displacements are computed based on temporal discretization of the overdamped Langevin equation given in Eq. (2.31) [38]. For a Brownian sphere close to a wall, horizontal and vertical displacements between simulation time step i and

step $i+1$, with step size $\delta t = (t_{i+1} - t_i)$ can be represented as

$$x_{i+1} \; - \; x_i \; = \; \sqrt{2D_{\parallel}(z_i)\delta t}\, \xi_R \, , \quad y_{i+1} \; - \; y_i \; = \; \sqrt{2D_{\parallel}(z_i)\delta t}\, \xi_R \tag{3.1a}$$

$$z_{i+1} \; - \; z_i \; = \; \alpha \, \frac{dD_{\perp}(z)}{dz}\bigg|_{z_i} \, \delta t \; + \; \frac{D_{\perp}(z_i)}{k_B T} \, F(z_i) \, \delta t \; + \; \sqrt{2D_{\perp}(z_i)\delta t}\, \xi_R \, , \tag{3.1b}$$

where (x, z) is the particle's position, $D_{\parallel,\perp}$ are the anisotropic diffusion coefficients defined in Chapter 2, ξ_R is a Gaussian random variable satisfying $\langle \xi_R \rangle = 0$ and $\langle \xi_R^2 \rangle = 1$, and F is the sum of all external forces. We have

$$F(z) = - \, \frac{\partial U(z)}{\partial z} \; = \; \frac{B}{l_D} \, e^{-\frac{z}{l_D}} \; - \; \frac{k_B T}{l_g} \, , \tag{3.2}$$

where l_D and l_g are the Debye and gravitational lengths, respectively, introduced in Chapter 2, and B is the double-layer strength. By choosing the system's length scale to be the particle's radius and the time scale to be the characteristic time the particle requires to diffuse its diameter $2a$ in two dimensions, $\tau_a = a^2/D_0$, we introduce the dimensionless parameters

$$\overline{\delta t} = \frac{\delta t}{\tau_a} = \frac{\delta t D_0}{a^2} \, , \tag{3.3a}$$

$$\bar{z} = \frac{z}{a}, \;\; \bar{x} = \frac{x}{a} \, , \;\; \bar{y} = \frac{y}{a} \tag{3.3b}$$

$$\bar{l}_D \; = \frac{l_D}{a} \, , \quad \bar{B} = \frac{B}{k_B T} \, , \tag{3.3c}$$

$$\bar{l}_g \; = \frac{l_g}{a} \; = \; \frac{3 k_B T}{4\pi \Delta \rho g a^4} \, . \tag{3.3d}$$

In these dimensionless units, Eqs. (3.1a) and (3.1b) become

$$\bar{x}_{i+1} \; = \; \bar{x}_i \; + \; \sqrt{2 \, \lambda_{\parallel}(\bar{z}_i) \, \overline{\delta t}}\, \xi_R \, , \quad \bar{y}_{i+1} \; = \; \bar{y}_i \; + \; \sqrt{2 \, \lambda_{\parallel}(\bar{z}_i) \, \overline{\delta t}}\, \xi_R \tag{3.4a}$$

$$\bar{z}_{i+1} \; = \; \bar{z}_i \; + \; \alpha \, \frac{d\lambda_{\perp}(\bar{z})}{d\bar{z}}\bigg|_{\bar{z}_i} \, \overline{\delta t} \; + \; \lambda_{\perp}(\bar{z}_i) \, \left[\frac{\bar{B}}{\bar{l}_D} e^{-\bar{z}_i/\bar{l}_D} - \frac{1}{\bar{l}_g} \right] \overline{\delta t} \; + \; \sqrt{2 \, \lambda_{\perp}(\bar{z}_i) \, \overline{\delta t}}\, \xi_R \, . \tag{3.4b}$$

Here, $\lambda_{\parallel,\perp} = D_{\parallel,\perp}/D_0$. In our simulations, we will investigate carefully the influence of the Debye and gravitational length parameters, $\bar{l}_D$ and $\bar{l}_g$, as well as the time parameter $\overline{\delta t}$, on the dynamics of the system. Typical values of the parameters $\bar{l}_g$ and $\overline{\delta t}$, for various bead sizes, are

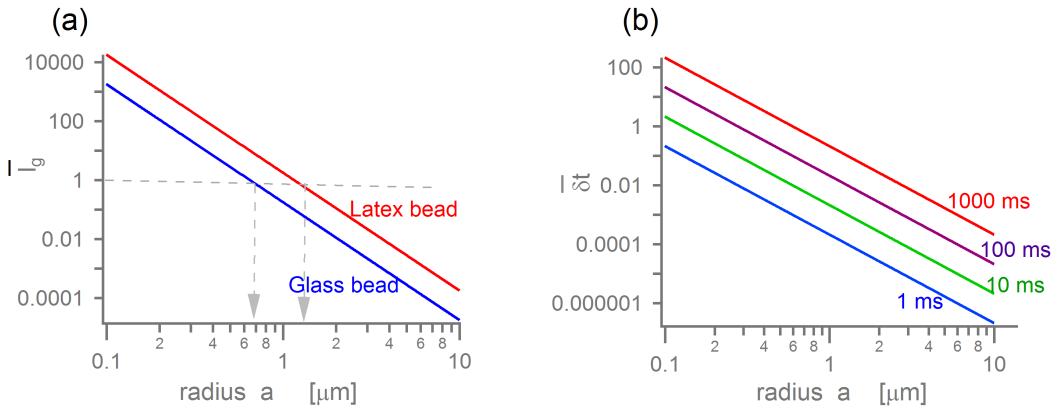

Figure 3.1: Simulation parameters vs. radius of sphere. (a) Gravitational decay length parameter $\bar{l}_g$ for a latex bead (density = 1.055 g/cc) and a glass bead (density = 2.5 g/cc) in water (density=1.0 g/cc). Dotted lines indicate that $\bar{l}_g = 1$ corresponds to different sizes for the different bead types. (b) Time step parameter $\overline{\delta t}$ for different time steps δt (diffusion in water; $\eta = 0.001$ Ns/m^2, T=293 K)

shown in Fig. 3.1.

From Eq. (3.4b), the rescaled drift velocity becomes

$$\bar{v}_d(\bar{z}) \;=\; \alpha\,\frac{d\lambda_\perp(\bar{z})}{d\bar{z}} \;+\; \lambda_\perp(\bar{z})\,\left[\frac{\bar{B}}{\bar{l}_D}e^{-\bar{z}/\bar{l}_D} - \frac{1}{\bar{l}_g}\right]\,. \tag{3.5}$$

3.1.2 Simulation time step

Numerical accuracy requires that the simulation time step be short enough that the drift function, $\bar{v}_d$, and diffusivity are essentially constant during each time period $\overline{\delta t} = \bar{t}_{i+1} - \bar{t}_i$ and spatially independent in each range $\overline{\delta z} = \bar{z}_{i+1} - \bar{z}_i$:

$$\bar{v}_d\left(\bar{z} \in [\bar{z}_i, \bar{z}_{i+1}]\right) \approx \bar{v}_d(\bar{z}_i)\;, \tag{3.6a}$$

$$\lambda_{\parallel,\perp}\left(\bar{z} \in [\bar{z}_i, \bar{z}_{i+1}]\right) \approx \lambda_{\parallel,\perp}(\bar{z}_i)\;. \tag{3.6b}$$

For parallel motion, the minimum time step required is constrained only by the particle's diffusivity, whereas the drift imposes further constraints on perpendicular motion. Since $\lambda_\parallel$ varies less rapidly than $\lambda_\perp$, we will consider only perpendicular motion, as it limits our choice of the simulation time step. One needs to take into account the fact that the dynamics strongly depends on the particle's z-position. Figure 3.2(a) shows the gradients of the drift and diffusivity as a function of height. As the bead gets closer to the wall, the drift gradient increases signif-

icantly, and the diffusivity reaches the maximum slope, which is unity. This drastic change in diffusion is more pronounced near the wall than at positions away from the wall. As a result, the choice of the simulation time step is essentially constrained by the degree of drift fluctuations very close to the wall, where $\bar{z} \ll \bar{l}_D$. The perpendicular diffusivity very close to the wall is approximately linear in the height

$$\lambda_{\perp,\text{wall}} \;\sim\; \lambda_0 \bar{z}\,, \tag{3.7}$$

with the dimensionless slope λ_0 approaching unity as $\bar{z}$ goes to 0. If we neglect the gravitational contribution, the drift very close to the wall can be approximated as

$$\begin{aligned}
\bar{v}_{d,\text{wall}} \;&=\; \frac{\lambda_0}{\bar{l}_D}\,\left[\bar{l}_D \;+\; \bar{B}\bar{z}\, e^{-\bar{z}/\bar{l}_D}\right] \\
&=\; \frac{\lambda_0}{\bar{l}_D}\,\left[\bar{l}_D \;+\; \bar{B}\bar{z}\,\left\{1 - \frac{\bar{z}}{\bar{l}_D} + \mathcal{O}\left(\left[\frac{\bar{z}}{\bar{l}_D}\right]^2\right)\right\}\right] \\
&\simeq\; \frac{\lambda_0}{\bar{l}_D}\,\left(\bar{l}_D \;+\; \bar{B}\bar{z}\right)\,.
\end{aligned} \tag{3.8}$$

At any position very close to the wall, the simulation spatial jumps, $\overline{\delta z}$, have to satisfy the constraints given in Eqs. (3.6a) and (3.6b) at any position $\bar{z}$. Constraint (3.6a) is the stronger of the constraints, since $\bar{v}'_{d,\text{wall}} = \bar{B}\lambda_0/\bar{l}_D \gg \lambda_0 = \lambda'_{\perp,\text{wall}}$ for realistic experimental parameters. We therefore require that

$$\frac{\bar{v}_{d,\text{wall}}(\bar{z} + \overline{\delta z}) - \bar{v}_{d,\text{wall}}(\bar{z})}{\bar{v}_{d,\text{wall}}(\bar{z})} \;\ll\; 1\,. \tag{3.9}$$

This condition can be rearranged to give

$$\overline{\delta z} \;\ll\; \frac{\bar{l}_D}{\bar{B}} \;+\; \bar{z}\,. \tag{3.10}$$

The required time step therefore depends on position as follows:

$$\overline{\delta t} \;\simeq\; \frac{(\overline{\delta z})^2}{2\lambda_{\perp,\text{wall}}} \;\ll\; \frac{\left(\frac{\bar{l}_D}{\bar{B}} \;+\; \bar{z}\right)^2}{2\lambda_0 \bar{z}} \;= \overline{\delta t}_{\max}(\bar{z})\,. \tag{3.11}$$

Plots of the maximum permissible time step function $\overline{\delta t}_{\max}(\bar{z})$, at different heights, are shown in Figure 3.2(b). The best choice for the simulation time step should be one that minimizes $\overline{\delta t}_{\max}$. Clearly, (3.11) has a minimum $\bar{z}_\text{m}$, satisfying

$$\left.\frac{d\overline{\delta t}_{\max}(\bar{z})}{d\bar{z}}\right|_{\bar{z}=\bar{z}_\text{m}} = 0 \quad\Longrightarrow\quad \bar{z}_\text{m} = \frac{l_D}{2\bar{B}}\,. \tag{3.12}$$

The appropriate choice of the simulation time step should be

$$\overline{\delta t} \ll \min_{\bar{z}} \left\{ \overline{\delta t}_{\max}(\bar{z}) \right\} = \left. \frac{\left(\frac{\bar{l}_D}{\bar{B}} + \bar{z} \right)^2}{2\bar{z}} \right|_{\bar{z}=\bar{z}_{\rm m}} = \frac{9}{4} \frac{\bar{l}_D}{\bar{B}} \tag{3.13}$$

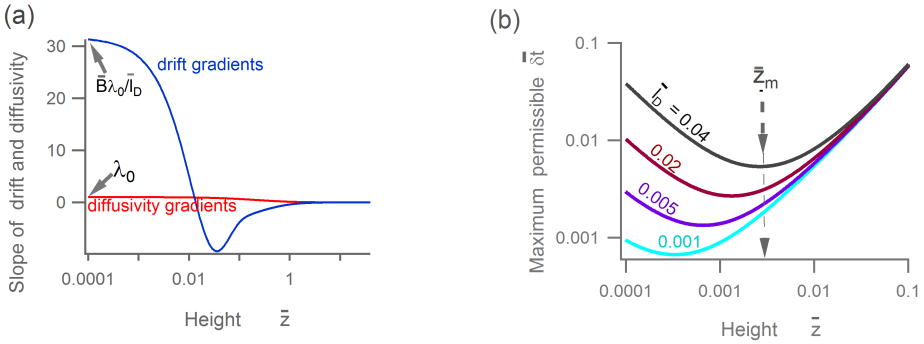

Figure 3.2: (a). Gradients of the drift and diffusivity vs. height. (b). The maximum allowed $\overline{\delta t}$ as a function of height for different Debye length $\bar{l}_D$ parameters. The scaled height $\bar{z}_m$ is for the $l_D = 0.04$ curve.

3.1.3 Numerical simulation algorithm

To simulate the particle's trajectory, I wrote a computer program in the *Igor Pro*[1] language. Having determined the simulation time step, the other parameters are set depending on the aim of the computation. The initial position for each trajectory is assumed to be known. Since the particle's long time dynamics is independent of the initial position, any choice from possible $(\bar{x}_0, \bar{z}_0)$ values can be used. We choose $\bar{x}_0 = 0$. However, for $\bar{z}_0$, one has to ensure that the particle visits that height in the duration of the trajectory. In our simulation, we choose the most-probable height, $z_0 = z_{\rm mp}$, as our initial z position, given by

$$\left. \frac{\partial U(\bar{z})}{\partial \bar{z}} \right|_{\bar{z}=\bar{z}_{\rm mp}} = 0 \quad \Longrightarrow \quad \bar{z}_{\rm mp} = \bar{l}_D \ln \left[\frac{\bar{B}}{\bar{l}_D \bar{l}_g} \right] . \tag{3.14}$$

The constraint given in Eq. (3.13) limits the computational speed of the algorithm. If a time step is too large, the particle may hit the wall after a few steps because of the greater drift and diffusion gradients near the wall. To get the trajectory for a given time step $\overline{\Delta t} > \overline{\delta t}$, we pick data points separated by about $n = \overline{\Delta t}/\overline{\delta t}$ simulation steps. In this thesis, we focus on

[1]Igor Pro, WaveMetrics Inc., USA. www.wavemetrics.com

steady-state equilibrium probability distributions. For such steady states, it is often convenient to assume ergodic motion and thus to estimate ensemble averages , denoted $\langle \cdot \rangle$, by taking long-time averages from single simulated trajectories.

3.1.4 Results

Figure 3.3 shows a portion of the particle's trajectory on the xy plane. It undergoes free Brownian diffusion because of the absence of external forces. In Fig. 3.4, we show the motion along z arising from the effect of Brownian diffusion under the confinement introduced by the gravitational and electrostatic potentials. As the particle diffuses closer to the wall, it gets pushed upwards by the double-layer force. The heights are compared with the perpendicular and normal displacements. The connection between the height of the particle and the displacements can be clearly observed for vertical motion: The more the particle moves closer to the wall, the smaller the displacements, as seen in Fig. 3.4. Hence, the particle spends more time in the regions very close to the wall than it does far away. Without an external force, this is also true for, e.g., Ito calculus, but for the isothermal calculus this effect is compensated by the noise-induced drift. For parallel motion, the displacements have less dependence on height.

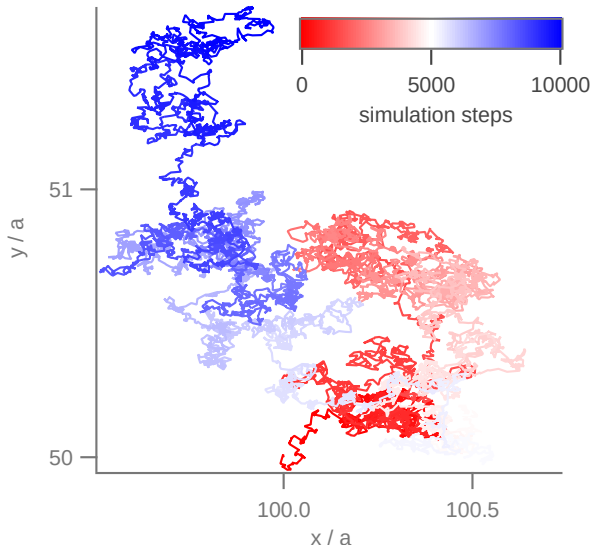

Figure 3.3: Two-dimensional simulated trajectory. ($\overline{\delta t} = 6 \times 10^{-3}$, $\bar{l}_g = 0.5$, $\bar{l}_D = 50 \times 10^{-3}$, $\bar{B} = 15$)

The height distribution, obtained from binning the particle's heights over a single trajectory, is shown in Fig. 3.5. We see that in the isothermal case, when $\alpha = 1$, the height distribution curve converges to the Boltzmann distribution. The particle spends more time close to the wall. Figure 3.6 shows the displacement distributions obtained from forming histograms of the displacements $(\bar{z}_{i+1} - \bar{z}_i)$. We see that the distributions are non-Gaussian at all time scales for

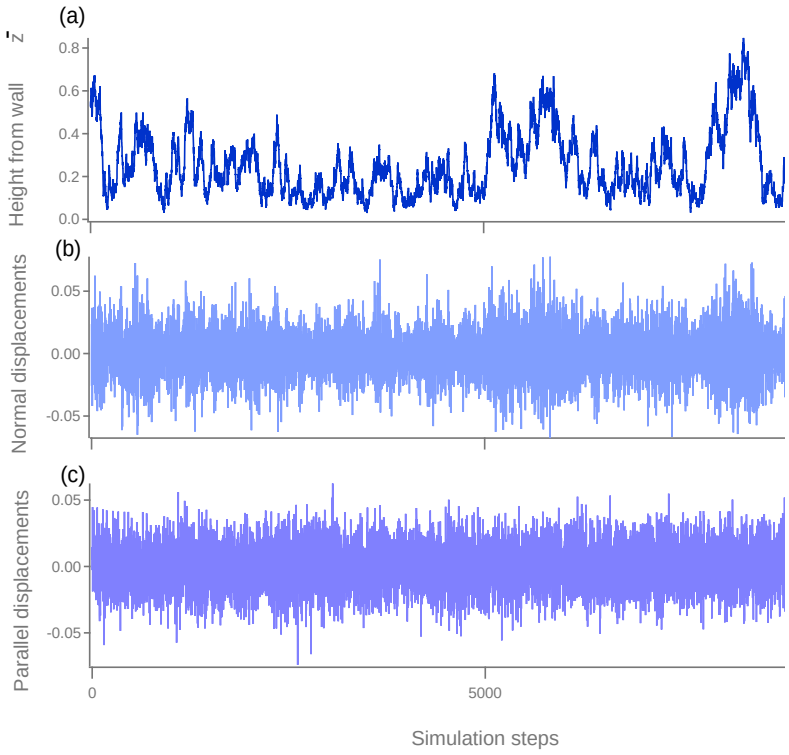

Figure 3.4: Heights and displacements (a) The particle's trajectory along z. (b) Diffusion close to the wall is characterized by small normal displacements. (c) The behavior for parallel displacements is not clearly visible. ($\overline{\delta t} = 6 \times 10^{-3}$, $\bar{l}_g = 0.05$, $\bar{l}_D = 50 \times 10^{-3}$, $\bar{B} = 15$)

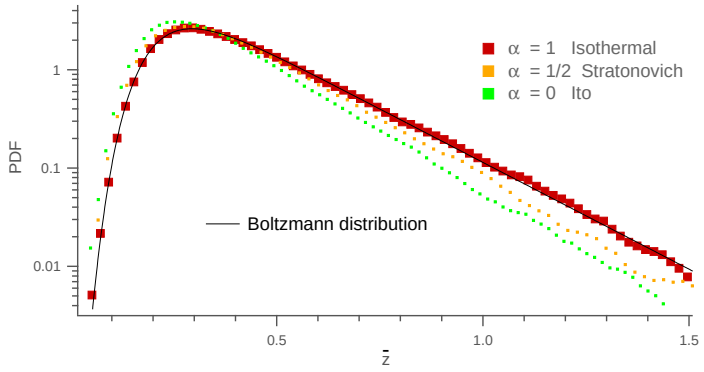

Figure 3.5: Distribution of heights of the particle. For simulations we used $\alpha = 0,\ 1/2$, and 1. Solid curve represents the expected Boltzmann distribution, which agrees with the $\alpha = 1$ simulation ($\overline{\delta t} = 6 \times 10^{-3}$, $\bar{l}_g = 0.33$, $\bar{l}_D = 50 \times 10^{-3}$, $\bar{B} = 16$).

perpendicular motion. The distribution tends to have broader tails compared to the Gaussian fits. For parallel motion, however, the distributions are approximately Gaussian.

The non-Gaussian z displacements in Fig. 3.6(a) come from two contributions: the bound-

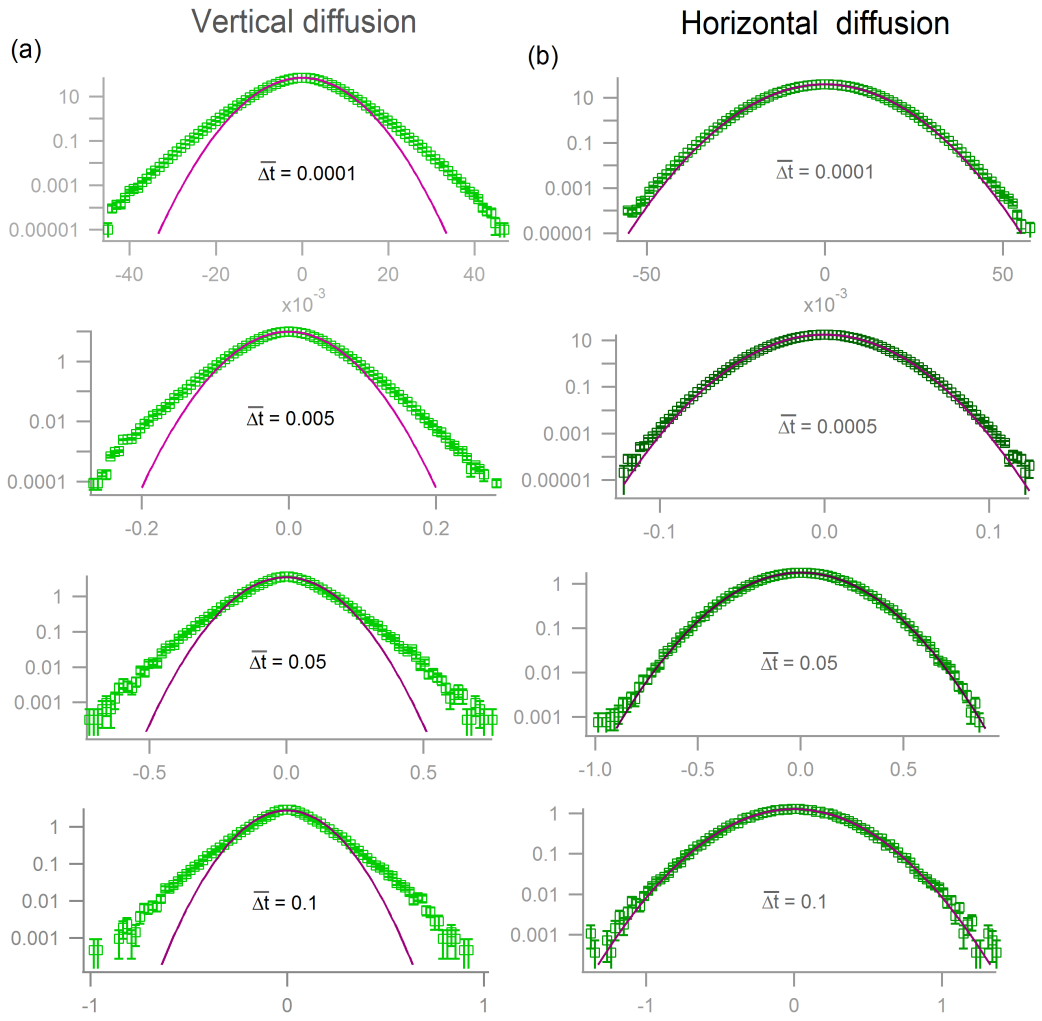

Figure 3.6: Distribution of displacements for time steps $\overline{\Delta t} = 0.0001,\ 0.005,\ 0.05$, and 0.1. (a) Distinctly non-Gaussian vertical distributions b) Nearly Gaussian horizontal displacements. ($\bar{l}_g = 0.2$, $\bar{l}_D = 30 \times 10^{-3}$, $\bar{B} = 16$)

ing potential and the spatial fluctuations in diffusivity. Parallel diffusion exhibits very nearly Gaussian dynamics for all experimentally accessible parameters. This results from the absence of external potential and the very small range of fluctuations in the parallel diffusivity, as can be seen from Figure 2.3. Hence, our only hope of observing non-Gaussian dynamics is to study perpendicular motion. However, perpendicular motion is complicated because of the bounding potential. The effect of the potential can be seen from the mean-squared displacement graphs shown in Fig. 3.7(b), which show nonlinear z mean-squared displacements at long time scales with strong dependence on the gravitational decay length. In this thesis, we are interested in identifying non-Gaussian dynamics due to diffusivity variations only, and not due to the poten-

tial. If we were able to measure non-Gaussian dynamics in horizontal motion, we would be able to conclude immediately that the non-Gaussian behavior comes from D fluctuations. But the effects are too small, and we focus instead on vertical motion. So far, it is not clear whether the non-Gaussian behavior in the vertical displacement distributions shown in Fig. 3.6(a) come from the potential only, or from both the potential and diffusivity fluctuations. Our goal is to find conditions where we can show that diffusivity fluctuations are the only cause of non-Gaussian dynamics in the vertical direction.

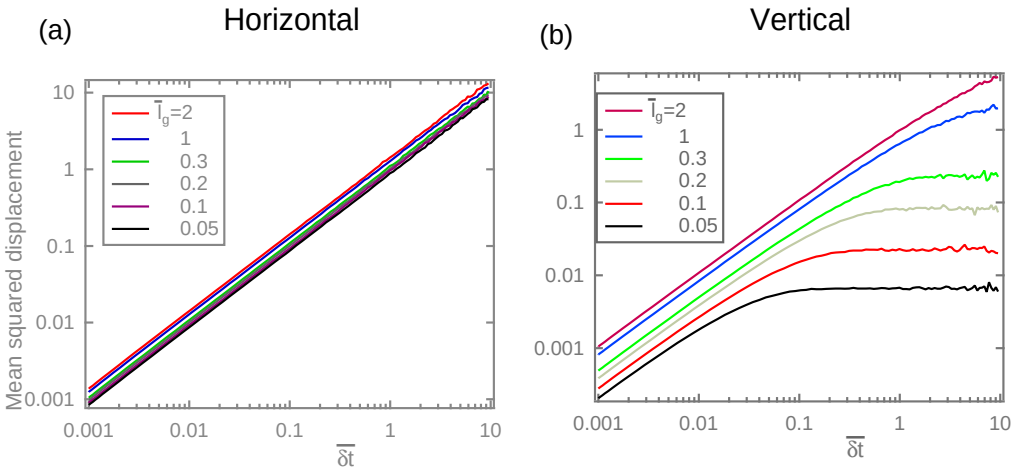

Figure 3.7: The mean-squared-displacement (MSD) vs. time steps from simulations. (a) Linear MSD for horizontal motion. (b) Vertical MSD is linear at very small time step sizes and saturates at long time steps because of the external potential.

3.2 Time Scales and non-Gaussian dynamics

We begin by investigating the role played by the time interval $\overline{\Delta t}$ in the emergence of non-Gaussian dynamics of the particle. This will enable us to understand the diffusive regimes of the system. Numerical results are from Brownian dynamics simulations.

To characterize non-Gaussianity, we determine the *excess kurtosis* of the displacements. Excess kurtosis, denoted κ, is defined as the measure of "peakedness" or flatness of the distribution relative to a normal distribution. Mathematically [39],

$$\kappa \equiv \frac{\mu_4}{(\mu_2)^2} - 3 \,, \tag{3.15}$$

where $\mu_n = \langle (\Delta \bar{z})^n \rangle$ is the n-th moment of the displacements. Normally distributed displacements have $\kappa = 0$. A distribution with positive kurtosis has heavier tails and a higher peak

than the normal distribution, whereas a distribution with negative kurtosis has lighter tails and is flatter, as illustrated in Fig. 3.8. (For the rest of the thesis, we will simply use the term *kurtosis* to refer to *excess kurtosis*.)

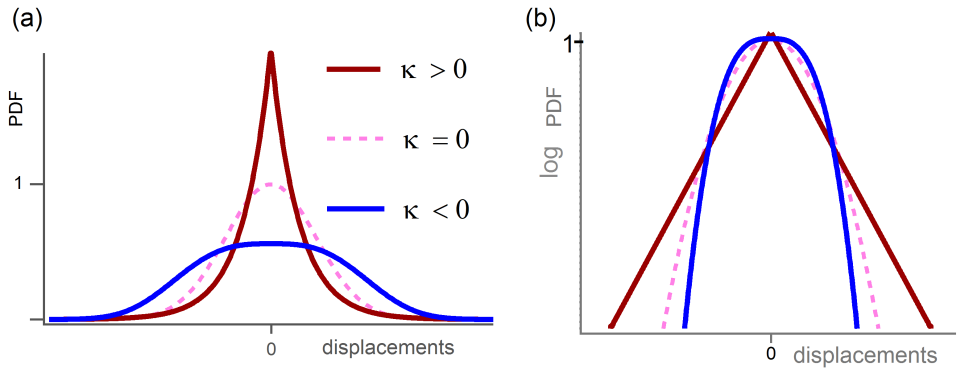

Figure 3.8: Excess kurtosis of distributions on (a) linear and (b) semi-log scales.

Figure 3.9 shows results from numerical simulations (outlined in Sec. 3.1) for the particle's dynamics at different time scales. At small time scales the kurtosis is constant [see Fig. 3.9(a)]. As the time scales get larger the presence of the bounding potential results to an increase in the kurtosis after some time step $\Delta\tau_c$. We thus classify the diffusive process into two time regimes: the diffusing-diffusivity ($\Delta t < \Delta t_c$) and the Boltzmann ($\Delta t > \Delta t_c$) regimes. In the diffusing-diffusivity regime, the non-Gaussian dynamics is driven by D fluctuations and the bounding potential has negligible influence. In this regime, the displacements are non-Gaussian; yet the MSD grows linearly with time. The non-Gaussian displacement distribution is generated by the diffusivity distribution $P(D)$ via Eq. 2.52. In Fig. 3.9(b), we investigate the kurtosis when the variation in the diffusivity is turned off for different dimensional time intervals. In this case, the absence of diffusivity fluctuations forces the kurtosis to go to zero at small time intervals corresponding to the diffusing-diffusivity regime. This confirms that the non-Gaussianity of the displacement observed in the diffusing-diffusivity regime in Fig. 3.9(a) arises solely from fluctuations in D. In the Boltzmann regime, the bounding potential dominates the D fluctuations, and the MSD saturates. At very large time steps, we can view each position measurement as an independent sample from the equilibrium Boltzmann distribution. In the long-time limit, the displacement distribution then is given by Eq. 2.53.

3.3 Displacement distributions at small times

To gain insight into the underlying statistical properties of the displacements, we simulate N trajectories and form histograms of the displacements $\Delta\bar{z} = (\bar{z} - \bar{z}_0)$. To reduce noise in the

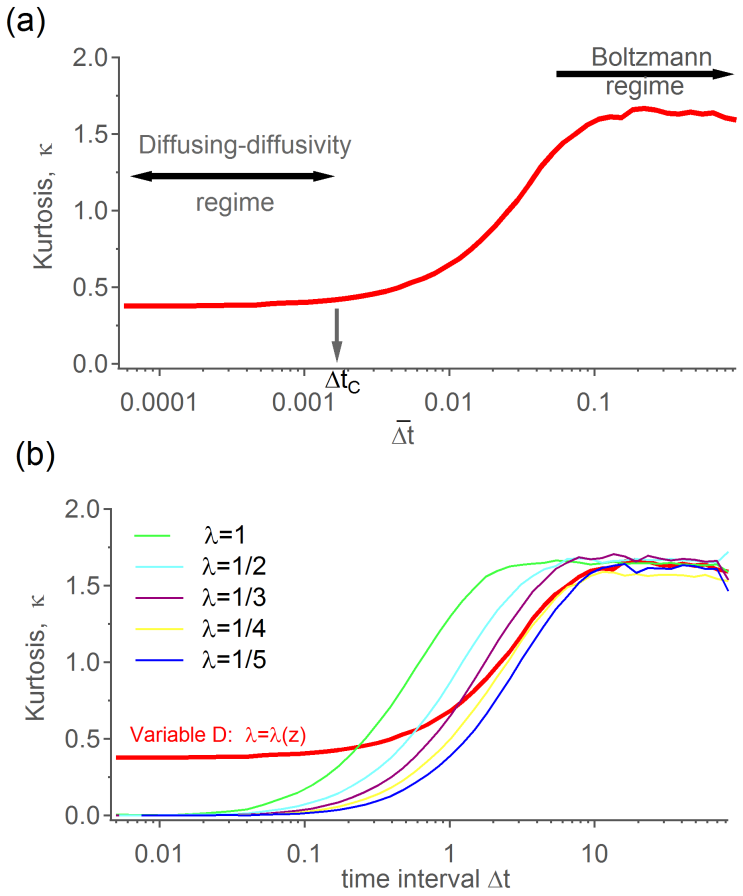

Figure 3.9: Excess kurtosis at different time steps for (a) variable D and (b) constant D values. Δt_c is the transition time scale and $\lambda = D_{\text{eff}}/D_0$ determines the constant effective diffusivity. Parameters used are $\bar{l}_g = 0.04, \bar{l}_d = 0.03$ and $\bar{B}$=15.

results, we need to simulate a very large number of trajectories. In this section, we introduce the numerical approximation of Eq. 2.52 for very small time steps, used in the diffusing-diffusivity regime. This approximation is based on Eq. (2.48) for very small fixed time steps:

$$P(\overline{\delta z}) \;=\; \int_0^\infty P(\overline{\delta z}|\bar{z}_0)\; P_B(\bar{z}_0)\; d\bar{z}_0 \;, \tag{3.16}$$

where $P_B(\bar{z}_0)$ is the Boltzmann distribution of heights and $P(\bar{z}|\bar{z}_0)$ is the conditional distribution of displacements, which is Gaussian at very short times [see Eq. (2.48)].

Figure 3.10 shows the displacement distributions obtained from integrating Eq. (3.16) over all possible starting positions, compared with results from numerical simulations of the Langevin equation. The results agree with simulations, especially at very small time steps.

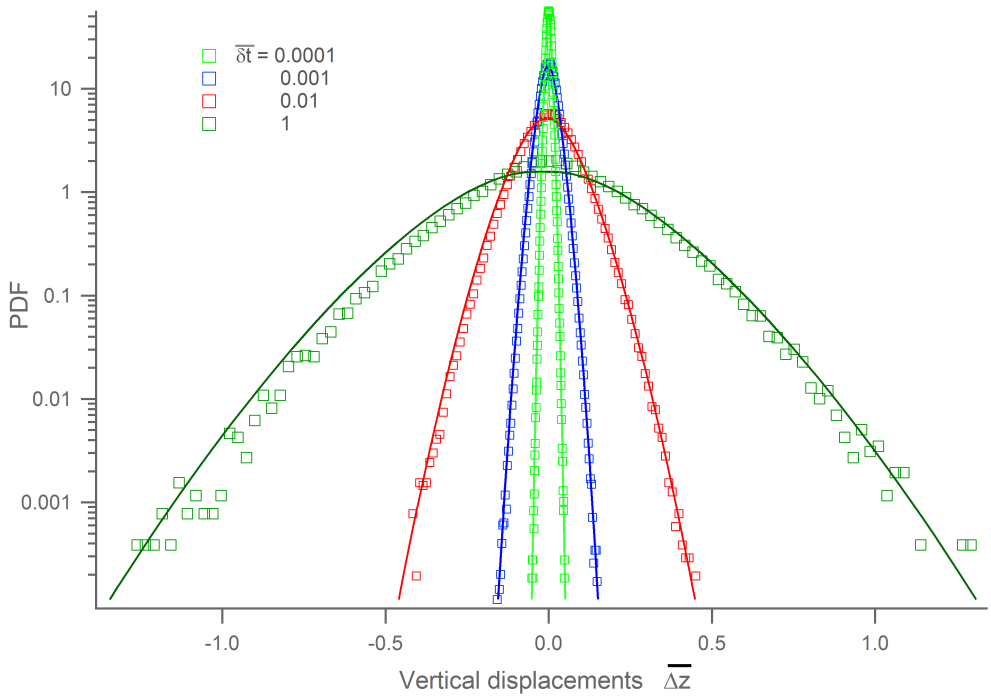

Figure 3.10: Displacement distributions from discrete-time Fokker-Planck solution method (solid lines) compared to results from discrete-time integration of the Langevin equation (data points). Parameters used are $\bar{l}_g = 0.5$, $\bar{l}_d = 0.03$ and $\bar{B} = 15$.

3.4 Diffusing-diffusivity dynamics

By analyzing the excess kurtosis at different time scales, we can classify the diffusion process based on the relative importance of diffusivity fluctuations and the external field. The most interesting scenario occurs when the diffusivity is the only contribution to non-Gaussian dynamics. In the following chapter, we will present an experiment to measure this non-Gaussian effect due solely to diffusivity fluctuations. In the experiment, we choose parameters so that the time interval lies in the diffusing-diffusivity regime. We now study the system's dynamics in the diffusing-diffusivity region, focusing on the effect of the gravitational decay length and Debye length parameters on the non-Gaussian behavior. We search for a set of parameters that

(i) eliminate the influence of the bounding potential on the displacements, so that we are in the diffusing-diffusivity regime, and

(ii) maximize non-Gaussian dynamics within the diffusing-diffusivity regime.

3.4.1 Diffusing-diffusivity parameter choice

For the dynamics to be in the diffusing-diffusivity regime, we require that the time scale be much less than the transition time; i.e., $\overline{\Delta t} \ll \overline{\Delta t_c}$. The transition time Δt_c is set by the balance between the average thermal displacement $\sqrt{\langle \Delta z^2 \rangle}_{\text{therm}} = \sqrt{2D\Delta t}$ and the average external field displacement $\sqrt{\langle \Delta z^2 \rangle}_{\text{ext}} = -\frac{1}{\gamma}\frac{\partial U}{\partial z}\,\overline{\Delta t}$. In dimensionless parameters, this gives

$$\overline{\Delta t_c} = \frac{2}{\lambda_\perp(\bar{z})\left(\frac{\bar{B}}{\bar{l}_D}e^{-\bar{z}/\bar{l}_D} - \frac{1}{\bar{l}_g}\right)^2} \,. \tag{3.17}$$

Hence, the choice of parameters depends on the height of the particle. At heights very close to the most-probable position, $\bar{z}_{mp} = \bar{l}_D \ln\left[\frac{\bar{B}}{\bar{l}_D \bar{l}_g}\right]$, almost any choice of parameters is allowed since the external forces vanish and $\overline{\Delta t_c}$ becomes very large. Next, we explore Eq. (3.17) at two regions: at heights very close to the wall and at heights away from the wall. Close to the wall, where $\bar{z} \ll \bar{l}_D$ and the gravitational potential can be neglected, Eq. (3.17) becomes

$$\overline{\Delta t_c} \;\approx\; \frac{2}{\lambda_0 \bar{z}} \left(\frac{\bar{l}_D}{\bar{B}}\right)^2 e^{2\bar{z}/\bar{l}_D} \,, \tag{3.18}$$

and the diffusivity follows $\lambda_\perp(\bar{z}) = \lambda_0 \bar{z}$. The right-hand-side of Eq. (3.18) takes a minimum at $\bar{z} = \bar{l}_D/2$. Hence,

$$\overline{\Delta t_c} \;\leq\; \frac{4e}{\lambda_0 \bar{B}^2}\, \bar{l}_D \,. \tag{3.19}$$

Away from the wall, we neglect the double-layer forces and, using $\lambda_0 \approx 1$, we get from Eq. (3.17) that the parameters required for diffusion must satisfy

$$\overline{\Delta t_c} \;\approx 2\, \bar{l}_g^2 \,. \tag{3.20}$$

From Eqs. (3.18) and (3.20), the location of $\overline{\Delta t_c}$ on the time axis is more sensitive to the Debye length than the gravitational decay length. Reducing the Debye length or the gravitational length pushes the diffusing-diffusivity region to shorter time scales.

Generally, in the experimentally-accessible parameter space, $\frac{4e}{\lambda_0 \bar{B}^2}\; \bar{l}_D \ll 2\; \bar{l}_g^2$. For overall diffusion at fixed $\overline{\Delta t}$, the requirement that $\overline{\Delta t} \ll \overline{\Delta t_c}$ is therefore set by the minimum of $\overline{\Delta t_c}$ which is attained very close to the wall. Hence, for the diffusion dynamics to exhibit diffusing diffusivity, we require that

$$\overline{\Delta t} \ll \frac{4e}{\lambda_0 \bar{B}^2}\, \bar{l}_D \,. \tag{3.21}$$

The required diffusing-diffusivity time scale is more constrained by the Debye length than by the gravitational decay length.

3.4.2 Optimizing non-Gaussian dynamics

Having established the time scales [given by relation (3.21)] for the particle to be in the diffusing-diffusivity regime, we now explore the influence of the length parameters $\bar{l}_g$ and $\bar{l}_D$ on the dynamics and look for the parameters that maximize the non-Gaussian dynamics within this regime. The influence of the double-layer potential strength $\bar{B}$ is not investigated since it is difficult to vary experimentally. We use the experimentally determined value, $\bar{B} = 15.6$, throughout this study.

Figure 3.11(a) shows the plot kurtosis for one value of the Debye length as a function of the gravitational decay length. We see that, for fixed $\bar{l}_D$, there is a corresponding gravitational decay length that optimizes the kurtosis. For a given Debye length, the motion becomes Gaussian at large decay lengths, since the particle does not feel the gravitational force. It undergoes free diffusion away from the wall where the diffusivity is almost constant, with the dominating stochastic solvent fluctuations pushing it away from the wall. As the decay length is reduced, the particle is brought closer to the wall by gravity, and the dynamics tends to become non-Gaussian on account of the diffusivity fluctuations introduced by the wall. As the gravitational decay length is reduced further, however, the particle becomes more confined by the gravitational and double-layer potential, and it diffuses over a shorter z range. This reduces the z-dependent diffusivity fluctuations, and the dynamics reverts to Gaussian. We therefore conclude that there is an optimal balance between the gravitational and double-layer forces that maximizes the non-Gaussianity (kurtosis) of the dynamics.

A family of curves of the kurtosis against the decay length for different Debye lengths is shown in Fig. 3.11(b). For very large Debye lengths, the kurtosis does not reveal a well-defined optimum for reasonable gravitational decay lengths. In this case, only extremely large $\bar{l}_g$ (too large for the particle to be considered Brownian) can reveal optimum kurtosis. Figure 3.11(c) shows kurtosis versus the Debye length for different decay length parameters. We see that shorter Debye lengths maximize non-Gaussian dynamics. At short Debye lengths, the particle is likely to diffuse very close to the wall owing to the the presence of the gravitation force. The frequent changes in the diffusivity near the wall lead to non-Gaussian dynamics, which increases continuously with decreasing height. From Fig. 3.11(c), we note that at $\bar{l}_D = 0.1$ the red curve, corresponding to $\bar{l}_g = 1$, maximizes the non-Gaussianity. At the smallest Debye length, the $\bar{l}_g = 0.2$ curve maximizes the non-Gaussianity. Hence, the right combination of $\bar{l}_D$ and $\bar{l}_g$ optimizes non-Gaussian dynamics of the particle.

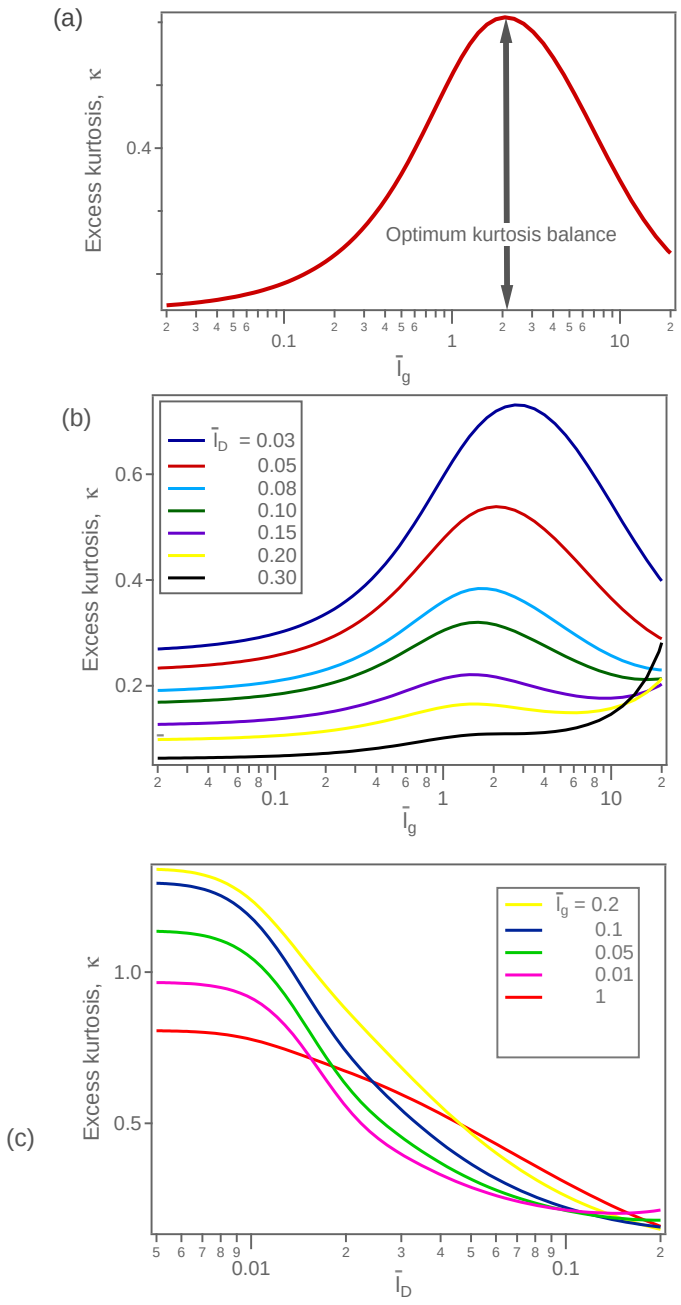

Figure 3.11: (a) Typical optimum of the kurtosis for a unique combination of the Debye length and gravitational decay length parameters. (b) Kurtosis vs. gravitational decay length for various Debye length parameters. (c) Kurtosis vs. Debye length for various gravitational decay length parameters ($\overline{\Delta t} = \overline{\delta t} = 0.0005$).

3.4.3 Non-Gaussian dynamics vs. diffusivity distribution

We have seen that a specific form of the bounding potential will optimize non-Gaussian dynamics of the Brownian particle. We now investigate the physics behind the specific choice of the optimizing parameters. Assuming that we are in the diffusing-diffusivity time regime, there should be a connection between the particle's non-Gaussian dynamics and its diffusivity distribution. The distribution of the particle's diffusivity takes the form

$$P(D) = \left\{ \frac{P_B(z)}{D_0} \left[\frac{d\lambda_\perp(z)}{dz} \right]^{-1} \right\} \Bigg|_{z=D_0\lambda_\perp^{-1}(D/D_0)}, \tag{3.22}$$

where $\lambda_\perp^{-1}(D/D_0)$ is the inverse of the diffusivity correction function $\lambda_\perp(z)$, and $P_B(z)$ is the Boltzmann distribution.

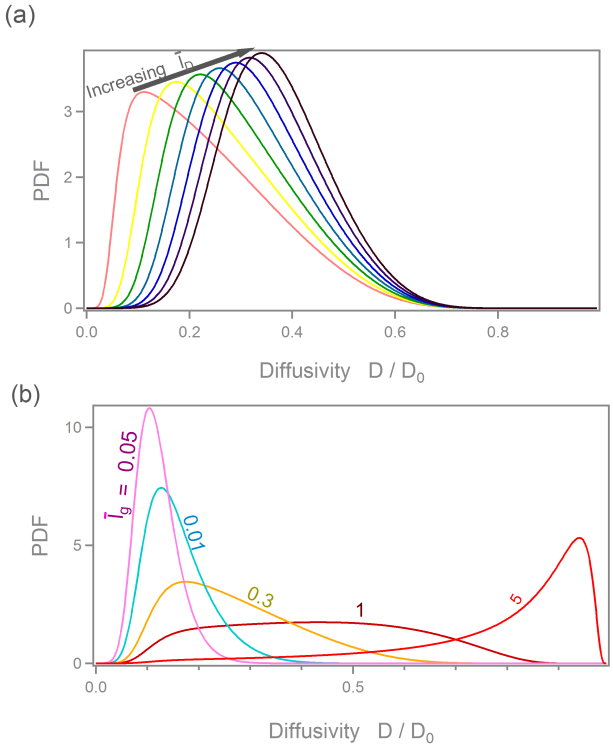

Figure 3.12: Distribution of the diffusivity for (a) various Debye lengths and (b) various gravitational decay lengths.

Figure 3.12 shows the distribution of the particle's diffusivity at different gravitational length parameters. Smaller Debye lengths and longer gravitational decay lengths result in larger spreads of the distributions. A measure of the spread of $P(D)$ will determine the non-Gaussian properties of the particle's dynamics. Larger diffusivity spreads will result in strong fluctuations in D. The spread of the distribution can be found by evaluating the variance of the diffusivity,

$\sigma_D^2 = \langle (D - \langle D \rangle)^2 \rangle$, where

$$\sigma_D^2 = \int_{D_{\min}}^{D_{\max}} (D - \langle D \rangle)^2 P(D)\, dD \,. \tag{3.23}$$

To evaluate Eq. (3.23), we need to know the range of heights explored by the particle within a certain duration of time, since the limits of the diffusion coefficient are given by $D_{\max} = D(z_{\max})$ and $D_{\min} = D(z_{\min})$. In the following, we determine the extreme heights, $z_{\min}$ and $z_{\max}$.

Extreme heights

How high will the particle go over a time $\mathcal{T}$, given length parameters $\bar{l}_D$ and $\bar{l}_g$? We start by approximating $\bar{z}_{\max}$ from the cumulative Boltzmann distribution of the particle :

$$P_c(\bar{z}) = \int_0^{\bar{z}} P_B(\bar{z}')d\bar{z}' = 1 - \exp\left(-\frac{\bar{z}}{\bar{l}_g}\right) \,, \tag{3.24}$$

where we have neglected the double-layer potential, assuming that $z_{\max}$ is at distances far away from the wall. For n measurements of the height having the random variables $Z_1, Z_2, \ldots, Z_n$, *extreme-value statistics* suggests that the cumulative probability of getting the maximum $Z_{\max}$ of the n random variables is given by [40, 41]

$$P(Z_{\max} \leq z) = P(Z_1 \leq z, Z_2 \leq z, \ldots, Z_n \leq z) = [P_c(z)]^n \,. \tag{3.25}$$

Hence, the cumulative distribution of the maximum height at very large n becomes

$$\begin{aligned} P_c(\bar{z}_{\max}) &= \left[1 - \exp\left(-\frac{\bar{z}_{\max}}{\bar{l}_g}\right)\right]^n \\ &= \left[1 - \frac{1}{n}\exp\left(-\frac{(\bar{z}_{\max} + \bar{l}_g \log[n])}{\bar{l}_g}\right)\right]^n \\ &= \exp\left[-e^{-\frac{(\bar{z}_{\max} + \bar{z}_g \log[n])}{\bar{l}_g}}\right] \,, \end{aligned} \tag{3.26}$$

where $\lim_{n\to\infty}(1 - x/n)^n = e^{-x}$. Equation (3.26) is the well-known *Gumbel* cumulative distribution function [40, 41] with mode $\mu = \bar{l}_g \log[n]$ and scaling parameter $\beta = \bar{l}_g$. The associated Gumbel density function is

$$P(\bar{z}_{\max}) = \frac{\partial P_c(\bar{z}_{\max})}{\partial \bar{z}_{\max}} = \frac{1}{\beta}\exp\left\{-\left(\frac{\bar{z}_{\max} - \mu}{\beta}\right) + \exp\left[-\frac{\bar{z}_{\max} - \mu}{\beta}\right]\right\} \,. \tag{3.27}$$

The expectation value of $\bar{z}_{\max}$ is

$$\langle \bar{z}_{\max} \rangle \;=\; \mu + \gamma\beta \;=\; \bar{l}_g \log[n] + \gamma \bar{l}_g \tag{3.28}$$

where $\gamma \approx 0.5772$ is the Euler constant. The number n can be scaled by the decay length $\bar{l}_g$ according to $n = \mathcal{T} D_0 / l_g^2$.

To find $z_{\min}$, we apply another extreme-value-statistics relation,

$$P_s(z \leq Z_{\min}) = P(z \leq Z_1, z \leq Z_2, \ldots, z \leq Z_n) = [P_s(z)]^n \;, \tag{3.29}$$

where P_s is the survival distribution function, given by

$$P(\bar{z}) \;=\; \int_{\bar{z}}^{\infty} P(\bar{z}')\, d\bar{z}' \;=\; \int_{\bar{z}}^{\infty} \frac{1}{\mathcal{Z}} \exp\left(-\bar{B} e^{-\bar{z}'/\bar{l}_D}\right) d\bar{z}' \;. \tag{3.30}$$

The gravitational force has been neglected in this case. Assuming $\bar{z}_{\min}$ to be less than the Debye length, we expand $\bar{B} e^{-\bar{z}/\bar{l}_D} \approx \bar{B} - \bar{B}\bar{z}/\bar{l}_D$. This holds true for $\bar{z} \leq \bar{z}_{\rm mp}$, where $\bar{z}_{\rm mp}$ is the most-probable height given by Eq. (3.14). We consider the displacements from the most-probable height, $\overline{\delta z}_{\rm mp} = (\bar{z}_{\rm mp} - \bar{z}) \geq 0$.

$$P_s(\overline{\delta z}_{\rm mp}) \;=\; \int_{\overline{\delta z}_{\rm mp}}^{\infty} \frac{1}{\mathcal{Z}'}\, e^{-\frac{\bar{B}}{\bar{l}_D}\overline{\delta z}'_{\rm mp}}\, d\overline{\delta z}'_{\rm mp} \;=\; \left[1 - \; e^{-\frac{\bar{B}}{\bar{l}_D}\overline{\delta z}_{\rm mp}}\right] \;. \tag{3.31}$$

Here, $\mathcal{Z}'$ is the new normalization function ensuring that $\bar{z} \leq \bar{z}_{\rm mp}$, i.e., at very small heights before the gravitational potential is felt. Therefore, the minimum height follows the cumulative distribution

$$P_c(\overline{\delta z}_{\min}) \;=\; \left[1 - \; e^{\frac{\bar{B}}{\bar{l}_D}\overline{\delta z}_{\min}}\right]^n \;. \tag{3.32}$$

where $\overline{\delta z}_{\min} \;=\; (\bar{z}_{\rm mp} - \bar{z}_{\min})$. Applying the same technique we used for obtaining $z_{\max}$ distribution in Eq. (3.26), we find the Gumbel distribution for $\bar{z}_{\min}$ with the parameters $\mu = \frac{\bar{l}_D}{\bar{B}} \log[n]$ and $\beta = -\frac{\bar{l}_D}{\bar{B}}$. Hence,

$$\langle \overline{\delta z}_{\min} \rangle \;=\; \langle (\bar{z}_{\rm mp} - \bar{z}_{\min}) \rangle \;=\; \frac{\bar{l}_D}{\bar{B}} \log[n] \;-\; \gamma \frac{\bar{l}_D}{\bar{B}} \;. \tag{3.33}$$

Using Eq. (3.14) for the most-probable height, we have

$$\bar{z}_{\min} \;=\; \bar{l}_D \ln\left(\frac{\bar{B}}{\bar{l}_D \bar{l}_g}\right) \;-\; \frac{\bar{l}_D}{\bar{B}} (\log[n] \;-\; \gamma) \;, \tag{3.34}$$

where n is now scaled by the Debye length according to $n = \mathcal{T} D_0 / l_D^2$. For a 1 μm bead diffusing in water, we obtain the typical values ($\mathcal{T} = 60$ s): $\bar{z}_{\min} = 0.04$ and $\bar{z}_{\max} = 5.3$

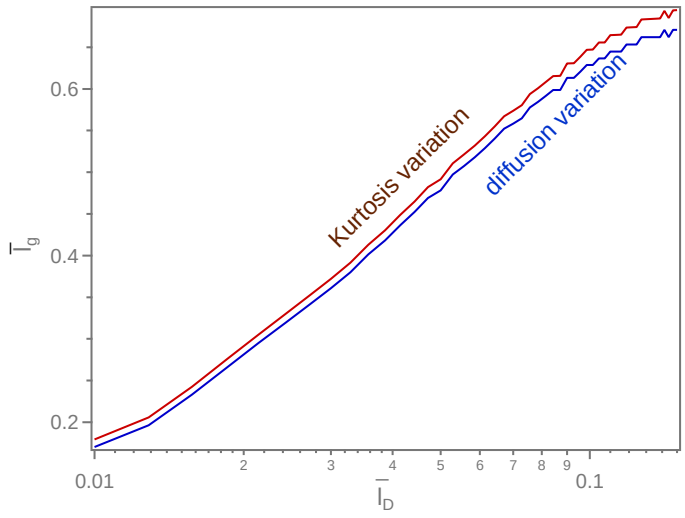

Figure 3.13: The sets of parameters that optimize the non-Gaussian dynamics and those that maximize the spread of the diffusivity distribution.

Using Eqs. (3.34) and (3.28) for the extreme values after a number of simulation steps, we construct the spread or variance of the particle's diffusivity at different sets of parameters. An interesting result is shown in Fig. 3.13. For given values of the decay length, we search for the corresponding Debye length values that optimize the kurtosis and then look for those Debye lengths that optimize the spread of the diffusivity distribution resulting from the particle's motion. We find that the two curves nearly match each other. Hence, non-Gaussian dynamics can alternatively be determined by the variance of the diffusivity fluctuations as the particle visits the possible states of the system. By maximizing this variance, we can optimize non-Gaussian dynamics.

3.4.4 Height-conditional displacements

From the previous discussion, we predicted that non-Gaussian dynamics can be determined from the variance of the diffusivity, not the height variance. The overall diffusion can be seen as a sum of diffusive processes, each with specific diffusivity at small height intervals. In this case, the non-Gaussian dynamics is also determined by the spread of ranges of heights explored by the Brownian particle. We analyze this scenario by dividing the accessible height into small intervals each with length δz, as shown in Fig. 3.14, and we study the dynamics in each interval.

Figure 3.15 shows results for the motion at very short displacements. In Fig. 3.15(a), we have the displacement distribution obtained from intervals $\overline{\delta t} = 0.1$ in succession with distance away from the wall. This was found by the path-integral methods, with limits of integration

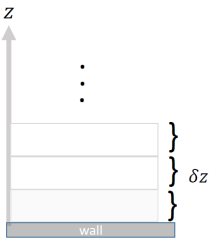

Figure 3.14: The accessible heights split into small intervals each with size δz.

set by the intervals explored. The time step size was the same for all intervals. Each individual displacement follows an approximately Gaussian distribution. The overall distribution, however, is characterized by broader tails and is clearly non-Gaussian. We claim that the non-Gaussian dynamics results from the longer range of heights the particle explores in the overall diffusion case. In Fig. 3.15(b), we look at the kurtosis at small intervals divided all the way to the wall, and each curve is for a different size of the intervals. For intervals very close to the wall, the dynamics start deviating from Gaussian. The dotted line indicates the level of the kurtosis of the overall diffusion. Interestingly, we note that an increment of size $\overline{\delta z} = 0.5$ very close to the wall has kurtosis equal to that of the overall diffusion. This implies that the range of heights is not the only variable determining the non-Gaussian dynamics, but the range of diffusivities is more significant. Thus, the height-conditional diffusive processes very close to the wall contribute more to the overall dynamics than those far away from the wall. This is caused by the stronger diffusivity fluctuations close to the wall.

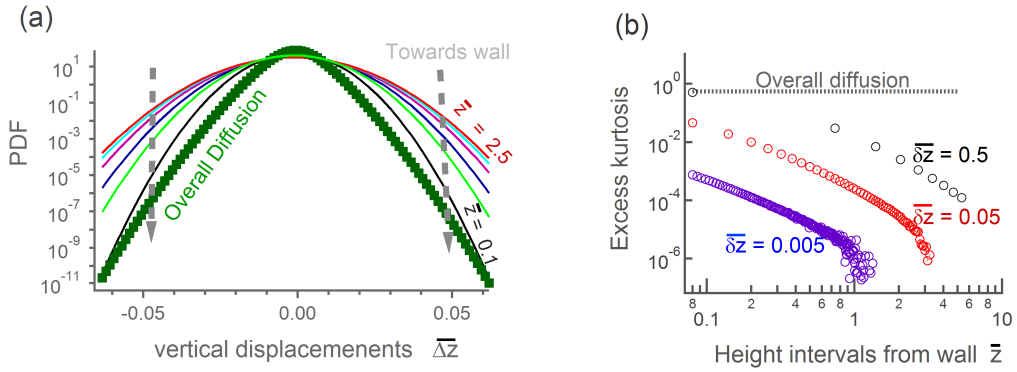

Figure 3.15: (a) Displacements from each interval tend to be Gaussian, but the overall diffusion becomes non-Gaussian. (b) Non-Gaussian dynamics is strongly dependent on the degree of fluctuations in D. ($\overline{\delta t} = 0.0001$)

3.5 Diffusing-diffusivity experiments

In Sec. 3.4, we discussed the parameter choice for maximizing non-Gaussian displacement distributions in terms of scaled parameters. Here, we consider their implication for choosing physical parameters. These optimal parameter values will be used in the experiments reported in Chapter 4. We also investigate the impact of measurement noise from experiments in our simulations.

3.5.1 Experimental choice of parameters

In the diffusing-diffusivity regime, fluctuations in D are the sole contribution to non-Gaussian dynamics. For the system to be in this regime, Eq. (3.21) requires

$$\frac{B^2}{k_BT}\,\frac{1}{\eta}\,\frac{1}{a^2 l_D}\,\Delta t \ll 24\pi e \qquad \left(\text{or } \varepsilon \equiv \frac{B^2\Delta t}{24\pi e\eta a^2 l_D k_BT} \ll 1\right). \tag{3.35}$$

In this description, the time interval Δt is set by the minimum resolution of our experiments. The radius a and the Debye length l_D can be tuned to satisfy Eq. (3.35) for a given experimental time step Δt_{exp}. In the experiment, to be discussed in Chapter 4, the experimental time step $\Delta t_{\text{exp}} = 0.033$ s, which is determined by the frame rate at which the camera acquires the images of the particle. It should be emphasized that the inequality in Eq. (3.35) is not a strong one: The derivation of Eq. (3.35) considered the extreme case when the particle is very close to the wall, $z \ll l_D$. However, the bead is less likely to be at such small heights in real experiments. We can therefore work in the regime

$$\varepsilon < 1\,. \tag{3.36}$$

The second requirement for successful diffusing diffusivity experiments is that the parameters should optimize non-Gaussian dynamics (kurtosis). As mentioned in Sec. 3.4.2, the right combination of the Debye and gravitational decay length will optimize non-Gaussian dynamics in the diffusing-diffusivity time scales. Before deciding on the choice of parameters for diffusing-diffusivity dynamics, experiments involving near-wall diffusion of latex beads (a=1.5 μm) in pure water were conducted, and some key parameters were obtained. A full discussion of the experiment will be given in Chapter 4. By fitting the distribution of the measured z-positions with the Boltzmann function, we obtained the parameters for the double-layer potential: $B/k_BT \approx 15$ and $l_D \approx 0.08$ μm. These experiments had parameters that do not satisfy Eq. (3.35) ($\varepsilon \approx 1.5$). We therefore could not tell whether the non-Gaussian displacements obtained came from the bounding potential or from D fluctuations. Three parameters could be altered from the initial experiments to satisfy Eq. (3.36): Δt_{exp}, l_D and a. However, we decided to change only the radius: Changing Δt_{exp} would be costly, since fast cameras can be

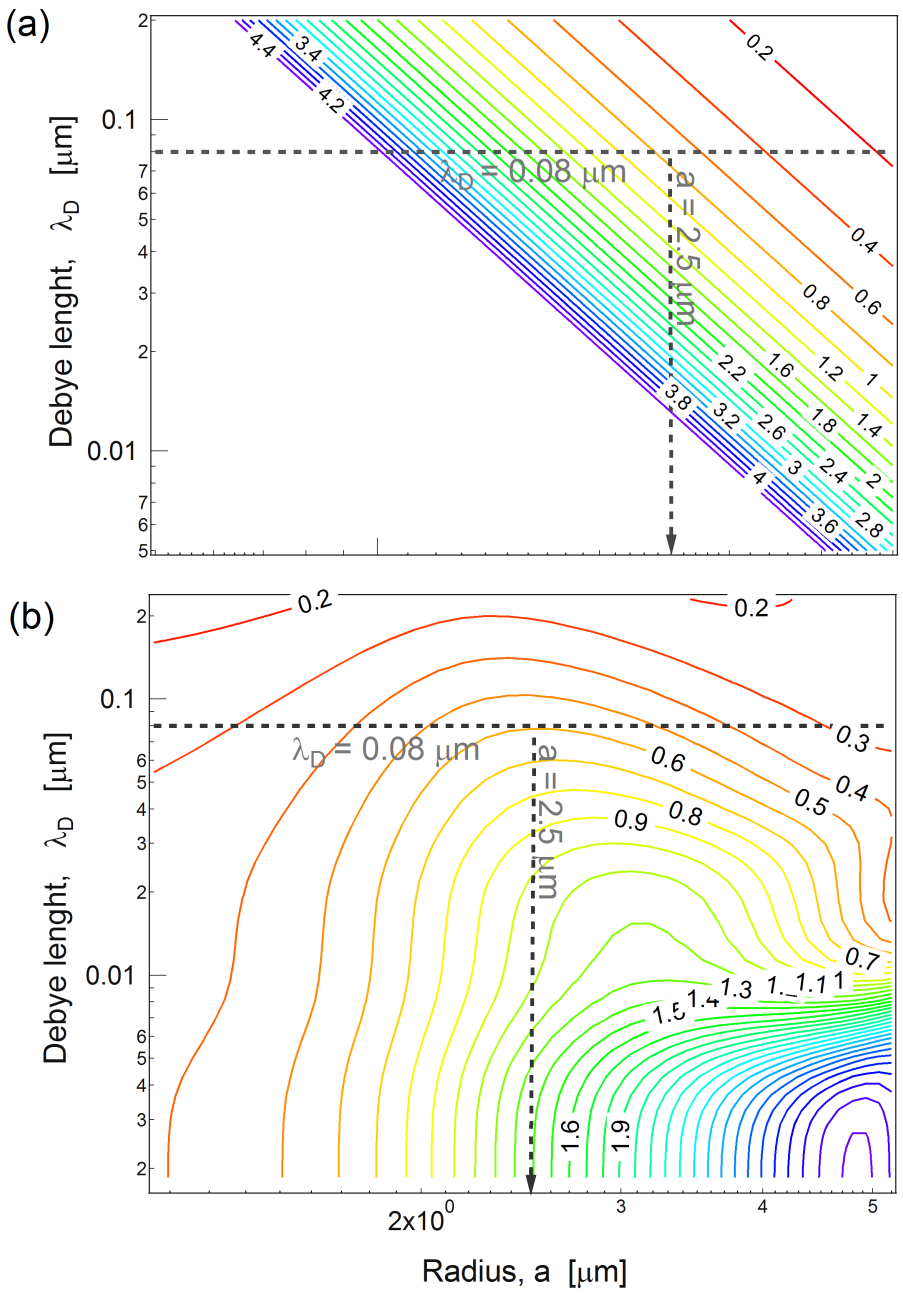

Figure 3.16: Contour plot of (a) the parameter ε and (b) kurtosis from simulations for the Debye length vs. the radius. Dotted lines shows the experimentally chosen parameters: $a = 2.5$ μm and $l_D = 0.08$ μm. Other parameters used in simulations are $B/k_BT = 15$, $\Delta t = 0.033$ s, $\Delta\rho = 0.055$ g/cc, $\eta = 0.0009$ kg/ms, and $T = 299K$.

expensive. The Debye length could be changed by applying salt to the samples, but this would lead to the beads sticking to the wall by van der Waals forces. This could be prevented by steric

stabilization. However, adding salt would also change some other parameters such as $\Delta\rho$, η and B , and it would be hard to keep track of all the parameters. We decided to change the radius since it strongly affects ε, and a variety of bead sizes are cheaply available commercially. Also, changing the radius does not have much effect on the other parameters, and the experiments can thus be done in a controlled manner.

Figure 3.16(a) shows a two-dimensional contour plot of the parameter ε for different values of a and l_D, with all other parameters determined from the experiment. Clearly, larger Debye lengths and larger bead sizes help satisfy condition (3.36). Figure 3.16(b) shows the corresponding contour plot for the excess kurtosis. Here, smaller Debye lengths maximize non-Gaussian dynamics, and the contours are peaked, as expected from the discussion in Sec. 3.4.2. From these graphs, we realized that the bead size $a = 2.5$ μm should be chosen for the experiment to be in the diffusing-diffusivity regime. This can be explained by studying the dotted lines in Fig. 3.16(a) and (b). The horizontal dotted lines indicate the value of the experimental Debye length. We note from Fig. 3.16(a) that $a = 2.5$ gives $\varepsilon = 0.4$ at the experimental value of l_D and, hence, satisfies Eq. (3.36). Figure 3.16(b) shows that $a = 2.5$ is also around the optimum kurtosis ($\kappa \approx 0.6$) for $l_D = 0.08$ μm. We then chose to change only the radius from the initial experiments to 2.5 μm, with all other parameters fixed.

3.5.2 Measurement Uncertainty

With the right parameters, we expect the bead's displacements to be non-Gaussian, as predicted by simulations. However, we have to consider some other factors that come into play in experiments. One is the presence of measurement uncertainty. In this section, we explore the effect of measurement noise on the dynamics, to see how much it changes the results from simulations.

In our experiments, there are two key contributions to measurement noise:

(i) *observation noise*: this comes from the equipment and the finite resolution of the optical microscope used;

(ii) *camera integration noise*: the position is typically measured by integrating a camera over a finite time Δt_s that is comparable to the experimental time Δt_{exp} (the time interval between the acquisition of images), and this introduces random error.

To simulate the experimental results, these effects can be included in the Langevin equation describing the observed position $\tilde{z}$ of the particle (z is the true position). Using the result from Yun and Bechhoefer [42], the observed positions $\tilde{z}_n$ of the particle at time intervals Δt_{exp} can be approximated by

$$\tilde{z}_{n+1} = \tilde{z}_n + \left.\frac{dD}{dz}\right|_{z=\tilde{z}_n} \Delta t_{\text{exp}} - \frac{1}{\gamma(\tilde{z}_n)} \left.\frac{\partial U(z)}{\partial z}\right|_{z=\tilde{z}_n} \Delta t_{\text{exp}} \; + \; \tilde{\xi}_n \; , \tag{3.37}$$

where $\tilde{\xi}_n$ is the sum of terms due to thermal fluctuations ξ_n, observation noise σ_n and camera integration noise χ_n. The effective noise $\tilde{\xi_n}$ is a linear combination of Gaussian random variables, and it is characterized by [42]

$$\langle \tilde{\xi}_n^2 \rangle = 2D(\tilde{z}_n)\Delta t_{\text{exp}} - \frac{2}{3}D(\tilde{z}_n)\Delta t_s + 2\sigma_n^2 \,, \tag{3.38a}$$

$$\langle \tilde{\xi}_n \tilde{\xi}_{n+1} \rangle = \frac{1}{3}D(\tilde{z}_n)\Delta t_s - \sigma^2 \,, \tag{3.38b}$$

$$\langle \tilde{\xi}_n \tilde{\xi}_{n+p} \rangle = 0, \qquad p \geq 2 \,. \tag{3.38c}$$

To simulate Eq. (3.37), we write $\tilde{\xi}_n$ in terms of uncorrelated Gaussian random variables $\psi_n \sim \mathcal{N}(0,1)$ [43]

$$\tilde{\xi}_n = c_+ \psi_{n+1} + c_- \psi_n, \qquad c_\pm = \frac{1}{2}\left(\sqrt{2D\Delta t_{\text{exp}}} \pm \sqrt{2D\Delta t_{\text{exp}} - \frac{4}{3}D\Delta t_s + 4\sigma^2} \right) \,. \tag{3.39}$$

The values of σ obtained from the experiment (to be discussed in Chapter 4) were $\sigma_x = 0.006$ μm and $\sigma_z = 0.012$ μm for horizontal and vertical diffusion, respectively. The camera exposure time was $\Delta t_s = 0.01$ s. Plugging these values into Eq. (3.39), we simulated the bead's trajectories using Eq. (3.37), with all parameters from the experiment. We compared the results to those for simulations without noise (with experimental parameters) in measurements. The results are shown in Fig. 3.17. We conclude that measurement noise has little impact on the displacement distributions at $\Delta t = 0.05$ s, and noise effects vanish at long time scales.

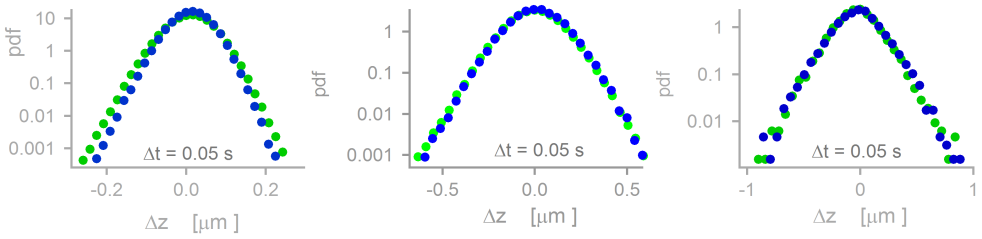

Figure 3.17: Comparison of simulations of the bead's dynamics with and without measurement noise for the displacement distributions. Blue lines/points represent simulations with measurement noise, and green lines/points are for simulations without measurement noise.

Chapter 4

Experimental Investigations

In this chapter, we report the results of direct measurements of hindered diffusion of latex beads in water near a flat wall. Measurements of colloidal diffusion have long been of interest for detailed study by optical methods, but Brownian motion prevents vertical observation of one single particle for extended periods because the target particle goes out of focus. Different techniques for measuring precisely vertical positions for near-wall diffusion have been reported in the literature. These include total internal reflection fluorescence microscopy [23], three-dimensional digital video microscopy [27], digital holographic microscopy [25], optical tweezers [44], optical Fourier processing [45], double-helix point-spread function technique [46], and off-focus imaging [47]. In this work, we designed and implemented a feedback tracking system to determine the vertical position of the latex bead near the wall. A feedback-controlled piezo vertical stage follows the bead as it diffuses up and down. This method enables us to measure the position of the particle over a wide range of heights, $z \approx 5\mu$m. We study the statistical properties of the displacements of the particle, as outlined in Chapter 3. A key point is to choose a sphere size and density such that the Boltzmann distribution due to the gravitational potential has a decay length comparable to the particle radius. As a result, the particle explores, over a reasonable time scale, a wide range of diffusion constants. The experimental parameters are chosen so that diffusion is in the diffusing-diffusivity regime, as discussed in Chapter 3.

We organize this chapter as follows: Section 4.1 introduces the basic parts of the setup used and the sample preparation. The measurement techniques for horizontal and vertical positions are presented in Sec. 4.2. In Sec. 4.3, we present results for the diffusing-diffusivity dynamics of the bead.

4.1 Experimental setup

We used and then improved the setup built by Schertel [48] and developed by Omelchenko [49]. The setup was mounted onto an air-damped optical table[1], supported by an anti-vibration base[2], to reduce low-frequency mechanical noise. A schematic diagram of our home-built microscope and feedback loop is shown in Fig. 4.1. All experiments were performed at room temperature. In this section, we outline the basic parts of the setup: the microscope, the sample, and the camera.

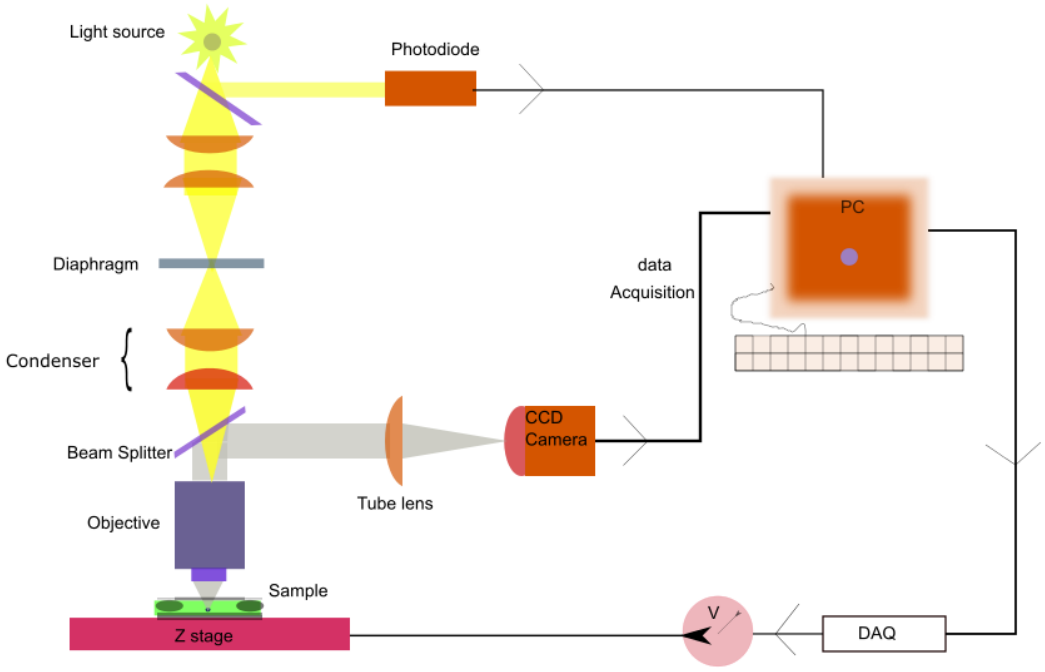

Figure 4.1: Schematic diagram of the microscope and feedback loop used to track the beads.

4.1.1 Microscope

We assembled a vertically aligned, bright-field microscope that imaged in reflection. A halogen bulb fiber-optic illumination[3] was used as a light source, made more uniform by putting a ground-glass plate in front of it. The path followed by light is shown in Fig. 4.1. Light from the illuminator was sent through two auxiliary lenses, the diaphragm, two lenses that form a condenser, and focused onto the back focal plane of the objective. We used a 60X water-immersion objective[4].

[1] Melles Griot, Rochester NY, USA.
[2] Model STL-3072-OPT, Newport Corporation, Irvine CA, USA.
[3] Model 190 Fiber-Lite Halogen Illuminator, Dela-Jenner Industries, Boxborough MA, US.
[4] UPlanSApo 60X/1.20W, NA=1.2, Olympus Corporation, Shinjuku, Tokyo, Japan

4.1.2 Sample

Samples were prepared as follows: Latex spheres were diluted and mixed with purified water, at volume fractions low enough ($\approx 10^{-6}$) that each bead can be considered to move independently from all others. We started with different bead sizes between 0.5 and 1.5 μm in radius. Sample chambers were made by placing four pieces of parafilm[5] between a microscope slide (1 mm thick) and a No. 1 coverslip ($\approx$ 0.17 mm thick). Samples were $\approx$ 60–80 μm in thickness, and the lateral separation between beads was $\approx$ 30 μm. The coverslip was first cleaned using a nitrogen gas ionizing gun[6] before use. The cell was partially sealed using parafilm melted on a hot plate, then filled (without bubbles) with the beads in solution. Finally, the cell was completely sealed with melted wax in order to avoid fluid flow due to evaporation or convection and allowed to cool.

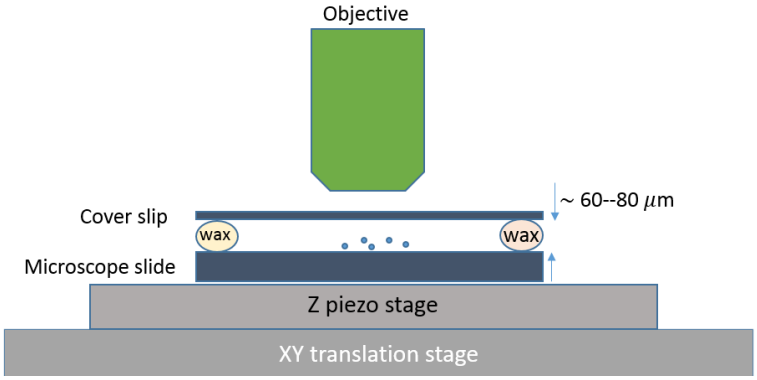

Figure 4.2: The design of the sample used in this experiment.

The sample was then placed on an XY translation stage[7], which moved the sample in search of beads to be captured by the camera. A feedback-controlled piezo stage[8] was used for tracking the z-positions of the bead. A schematic diagram of the sample design is shown in Fig. 4.2. In this design, light coming from the objective passed through the cover-slip, then through the fluid, and was either reflected by the bead or passed into the microscope. Some of the light was reflected at the fluid-microscope slide interface and returned to the objective as background light.

4.1.3 Camera

The reflected light from the sample was scattered and passed through the infinity-corrected objective and a beam splitter and was focused by a tube lens onto a CCD camera[9]. The image

[5] American National Can, Neenah WI, USA.
[6] Top Gun Static Neutralizer, SIMCO Inc., Hatfield PA, USA.
[7] 25 mm-ranged XY translation stage model 406, Newport Corporation, MT, Irvine CA, USA.
[8] Nano-drive 85, Mad City Labs, Madison WI, USA.
[9] Model FL3-FW-03S1M-C, Point Grey Research, Richmond BC, Canada.

acquired was processed via the computer, using *LabVIEW* software, to determine the position of the bead (see Sec. 4.2). The camera was triggered by the rising edge of a square wave from a function generator[10]. The camera's frame rate was set to 30 Hz, and the shutter speed was set to $\tau_s = 10$ ms. Intensities were digitized at 12-bit resolution ($2^{12} = 4096$) and mapped onto a 16-bit intensity scale ($2^{16} = 65536$). The field of view of the camera was about 60 μm $\times$ 40 μm. This imposed a limit to the amount of time the particle remained in the field of view and, therefore, the amount of data that was collected from a single particle. The average amount of time the particle spends within a one-dimensional distance l takes the form $\tau \sim l^2/2D$. For a bead of radius 3 μm freely diffusing in pure water, the diffusion constant $D \approx 0.1$ μm^2/s. Assuming that the bead started diffusing from the center of the field of view, the minimum distance the bead could travel is $l = 20$ μm. We can then estimate the total average time the bead spent within the field of view as follows: $\tau \approx (20\mu\text{m})^2/(2 \cdot 0.1\mu\text{m}^2/s) = 2000$ s, which corresponds to $\approx 66\,000$ time steps.

4.2 Position measurements

We acquired and processed images at fixed time intervals (33 ms) to determine the bead's trajectory. We did this until the bead diffused out of the field of view, or got stuck to the wall. In practice, we were able to collect data for up to 10000 s: When the monitored bead diffused out of the field of view, we used the XY stage to manually reset the bead's image to the center of the field of view and continued collecting data on the same bead. In the following, we describe how we determined the bead's horizontal and vertical positions.

4.2.1 Horizontal position measurements

To track the position of the bead in the xy-plane, we used the centroid-tracking algorithm from the IMAQ Vision module for LabVIEW, which locates a circular edge in a defined search area. The algorithm detects intersection points between a set of search lines defined by a spoke and the edge of an object. The intersection points are mainly determined based on the contrast in the image. This method works by first making an initial guess for the location of the bead. Next, any background intensity below some intensity threshold is set to zero, in order not to bias the center-of-mass calculation. Finally, a local region around the initial guess is selected, and the center of mass is used to estimate the center of the bead. Figure 4.3 shows the y-projection of the method for an image on the xy-plane. The pixel coordinates of the bead's center of mass were then converted to real units. To calibrate distances, we imaged a 2D grating with 5×5 μm grid squares, as shown in Fig. 4.4.

[10] 2 MHz Function Generator, Model 3011b, B&K Precision Corporation, Yorba Linda CA, USA.

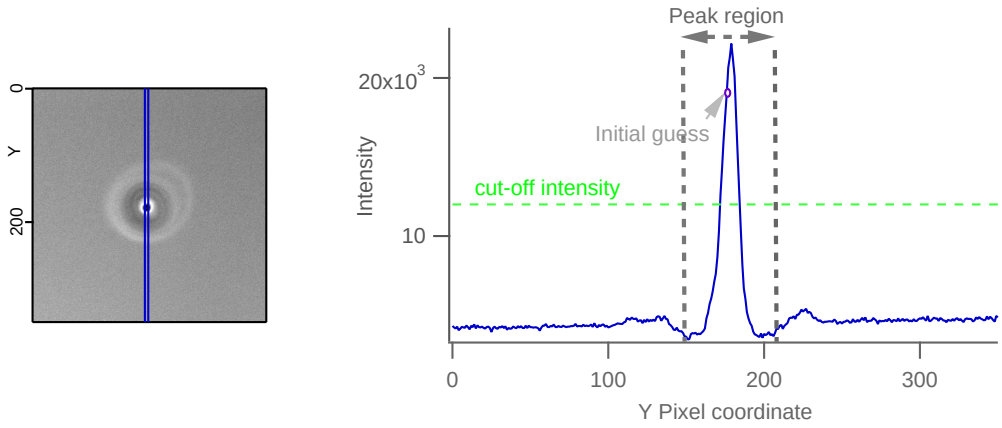

Figure 4.3: y-projection of the method used for locating the bead in the xy-plane.

We found that for x, 1 pixel = 0.125 μm; and for y, 1 pixel = 0.127 μm. Since we expect equal scale factors in both directions, we take our calibration factor to be

$$1 \text{ pixel} = 0.126 \pm 0.001 \ \mu\text{m} \ . \tag{4.1}$$

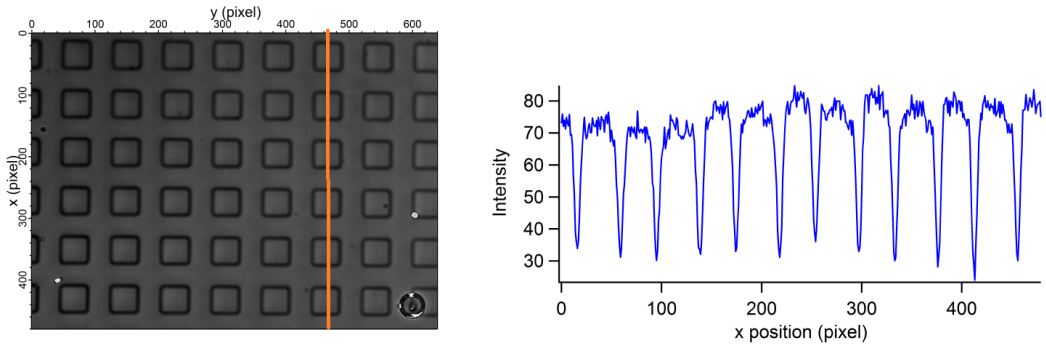

Figure 4.4: (a) An image of the calibration grating with 5×5 μm squares. (b) The related intensity profile across the calibration grating (along red line).

A typical 2D trajectory for a latex bead with radius $a = 2.5$ μm is shown in Fig. 4.5(a). Uncertainties in our measurements were introduced by the presence of measurement noise. To determine the size of displacements (Δx_n and Δy_n) introduced by measurement noise, we measured the positions $(\tilde{x}, \tilde{y})$ of an immobilized bead, stuck on the surface. The results are shown in Fig. 4.5(b). We found the position displacements of the stuck bead via $\Delta\tilde{x}_i = \tilde{x}_{i+1} - \tilde{x}_i$

and $\Delta\tilde{y}_i = \tilde{y}_{i+1} - \tilde{y}_i$. Assuming that the stuck bead measurement noise is not correlated in time, we attributed these displacements to measurement noise; i.e., $\Delta\tilde{x}_i = \Delta x_n$ and $\Delta\tilde{y}_i = \Delta y_n$. Plots of the measurement-noise displacements are shown in Fig. 4.5(c). We formed histograms of the displacements, finding Gaussian curves [see Fig. 4.5(d)]. The obtained width $\sigma^2_{\Delta xy}$ of the fitted Gaussian histograms gives the apparent displacement σ_{xy} due to measurement noise for horizontal motion. We found $\sigma_{\Delta xy} \approx 0.0089 \pm 0.00001$, implying $\sigma_{xy} = 0.0089/\sqrt{2} = 0.0062$ μm.

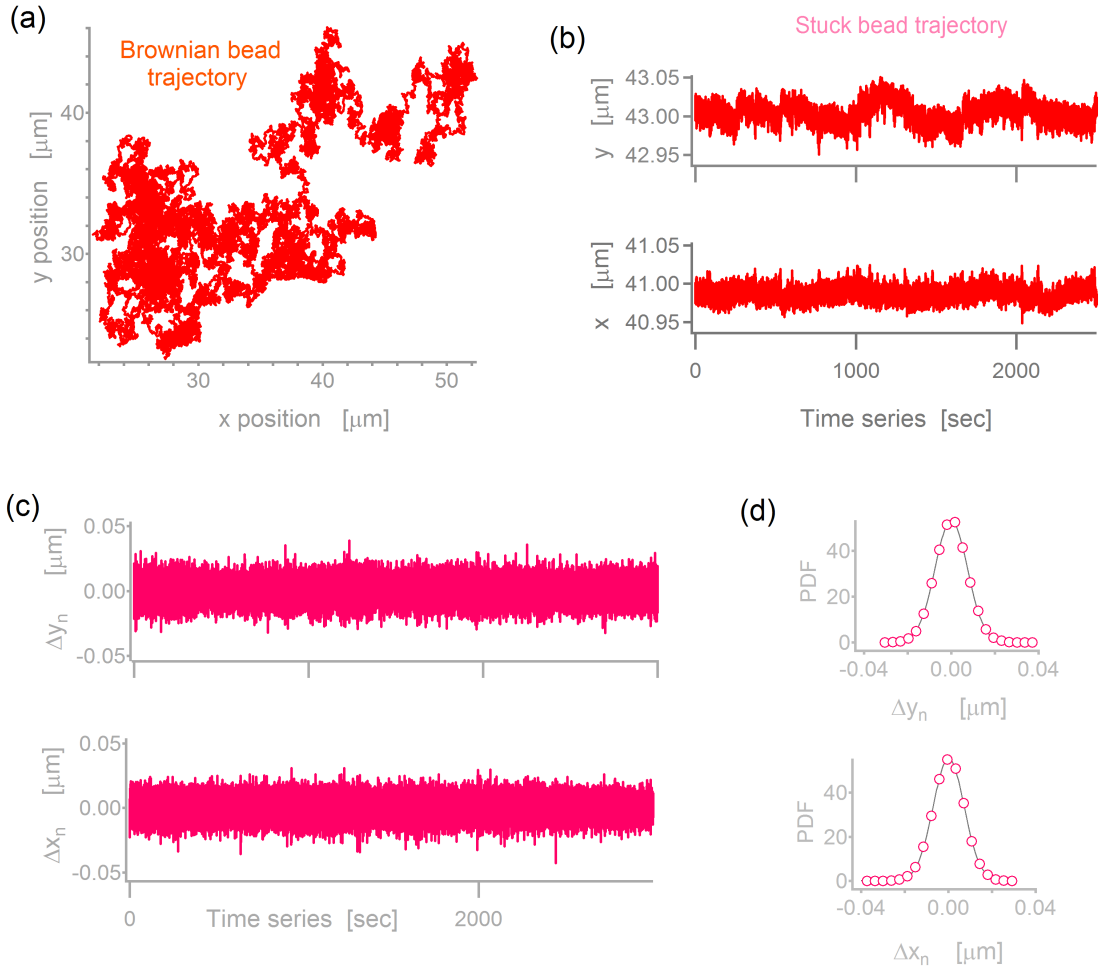

Figure 4.5: Bead trajectory and measurement noise determination. (a) Trajectory of a latex bead (radius = 2.5 μm). (b) x- and y-positions of a bead stuck to the microscope slide. (c) Apparent displacements of the stuck bead due to measurement noise. (d) Histograms of the noise displacements.

4.2.2 Vertical position measurements

The vertical position of the bead was found by measuring its intensity. A 3 μm bead would diffuse a vertical range of ≈ 4 μm after 20 minutes. This distance of 4 μm exceeds the depth

of focus of the microscope. To keep the bead in focus, we tracked it by a feedback loop (to be discussed below), which used a vertical piezo-stage to move the sample following the bead's motion. We recorded intensity measurements in a 3 × 3 pixel region centered on the pixel containing the bead's intensity maximum. This is shown in Fig. 4.6. We then took an average of these nine intensity values to give the intensity of the bead.

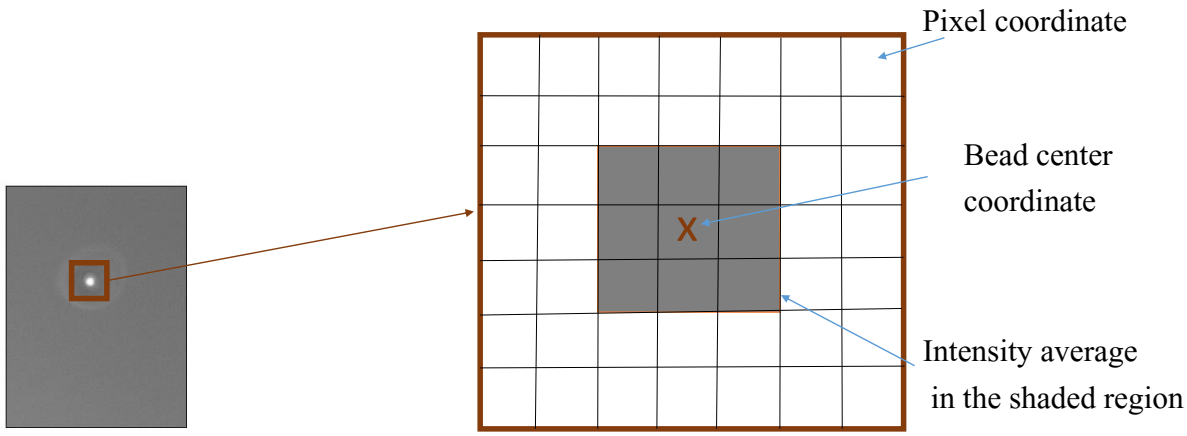

Figure 4.6: Intensity of a bead was found by averaging over a 3 × 3 pixel region around the bead's center xy-position.

Intensity profile and calibration

We first determined how the intensity of the bead changed with height. This was achieved by

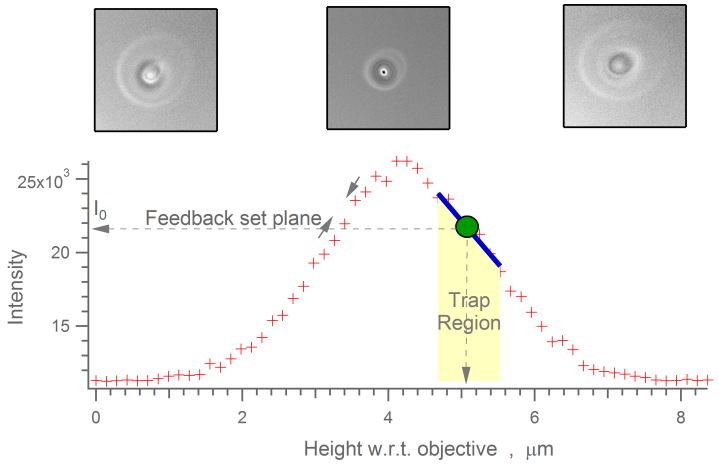

Figure 4.7: The intensity profile of a bead stuck to the microscope slide. Beads were trapped in the shaded (blue line) region, where displacements depended linearly on intensity values.

vertically moving an immobilized bead, using a voltage applied to a piezo-stage, and measuring the intensity of the bead from the images taken. Figure 4.7 shows the intensity of the bead with distance from the objective. The stage needed to be calibrated, as well, to find the relation between the applied voltages and actual distance. Using a Linear Variable Differential Transformer[11] (LVDT) gave a calibration of 1 V= 6.54 μm for the piezo-stage [48]. The intensity calibration was repeatedly performed for each set of measurements, as the setup would change if one tampers with it. We assumed that the optical properties of a diffusing bead are close to those of the stuck bead.

Feedback loop

We introduce the feedback loop used in the experiments. In the next subsection, we will see that the feedback was applied to a stuck bead, not a Brownian bead. For now, however, we study how the feedback works for any bead. The goal of the feedback loop was to keep the bead trapped at a fixed height z_0 from the objective, in the linear region shown in Fig. 4.7. This was

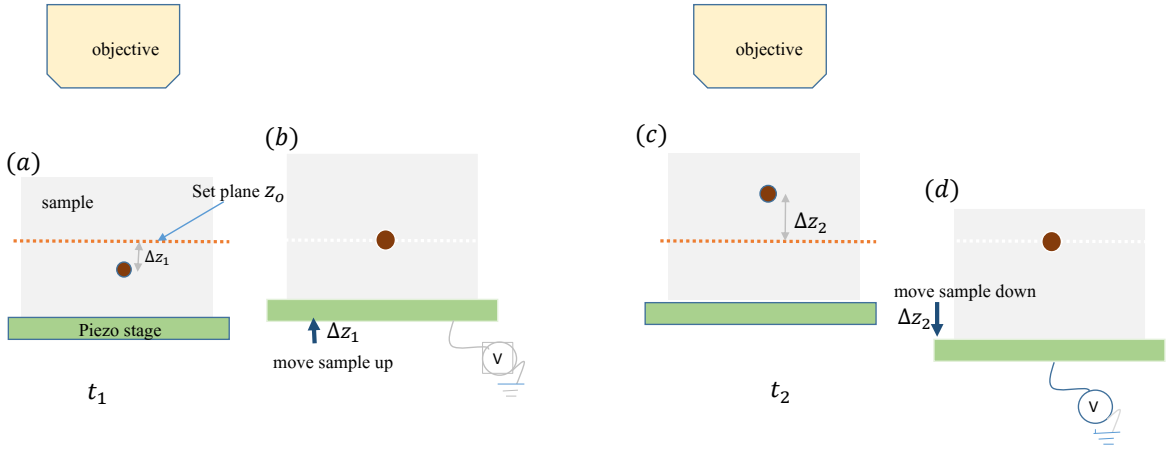

Figure 4.8: Schematic diagram of the feedback loop. (a) At time t_1 the bead is displaced a distance Δz_1 from the set plane z_0. (b) We apply a voltage to the piezo-stage to move the sample up a distance Δz_1 to bring the bead to z_0. (c). At a later time t_2 ($t_2 - t_1 = 33$ ms), the bead diffuses a new displacement Δz_2. (d). We then move the sample to bring the bead down to z_0 by the feedback voltage applied in the opposite direction, and the iteration continues.

achieved by applying a feedback via the piezo-stage to move the sample so that the intensity of the bead was kept near some value I_0 (corresponding to z_0). A schematic diagram of the feedback loop is illustrated in Fig. 4.8. We chose the region of steepest slope as the trap region, on either side of the intensity profile. This ensured that the bead had the highest sensitivity to intensity changes with height. Furthermore, the chosen region was slightly out of focus, to prevent any ambiguity about the sign of the required feedback. The bead's intensity changes

[11] Schaevitz/Measurement Specialties, Hampton VA, USA.

were then translated to actual distances moved by the bead using the linear fit of the intensity profile (see blue line in Fig. 4.7).

The feedback loop follows these steps:

- an image is taken;
- the LabVIEW program determines the bead's intensity I and calculates the difference $\Delta I = I - I_0$ from the desired set point intensity I_0;
- the slope b from a linear fit of the intensity profile is used to calculate the required voltage $v \propto \Delta I$ to move the particle back to the set plane. Via a LabVIEW Data Acquisition (DAQ) device[12], the voltage is applied to the stage to move the sample to keep the bead near z_0.

Correcting mechanical drift

One problem encountered in our feedback-based measurements came from mechanical drift due to temperature changes. These temperature changes caused thermal expansion or contraction of components of the microscope. Mechanical drift between the sample cell and the microscope objective was a serious problem, as it could produce large uncertainties in the height of the bead relative to the sample cell's bottom plate. As a consequence of the drift, the trap region in Fig. 4.7 shifted. The feedback was not robust to such drifts and would mistake the shift for a change in the bead's position. This drift was seen when we measured the intensity of a stuck bead. One would expect the recorded intensity values to have some experimental noise fluctuations around a constant value since the bead was stationary. However, we typically obtained results such as those shown in Fig. 4.9(a), which reveal a drift. Measurement noise resulted in uncertainty in the z-position of the stuck bead. To evaluate the apparent displacements Δz_n due to measurement noise, we first converted the intensity fluctuations of the stuck bead to z-position fluctuations. We then applied the same method we used for evaluating horizontal noise displacements: We took differences between successive z-positions of the stuck bead as the displacements due to measurement noise [see Fig. 4.9(b)], having assumed that the positions are not correlated in time. Figure 4.9(c) shows the histogram of the noise displacements, which is Gaussian. The width of the Gaussian fit was $\sigma_{\Delta z_n} \approx 0.018 \pm 0.0002$ μm. Hence, the standard deviation, for a single z-position measurement, was $\sigma_z \approx (0.018/\sqrt{2})$ μm $= 0.012$ μm.

To correct for this mechanical drift, we tracked two beads: a stuck bead and a freely diffusing *Brownian* bead, as shown in Fig. 4.10(a). We used the stuck bead as a reference from which the position of the Brownian bead could be determined. This enabled us to locate the bottom of the sample. To eliminate the mechanical drift, we applied the feedback loop to the stuck

[12]NI USB-6212, National Instruments, Austin TX, USA.

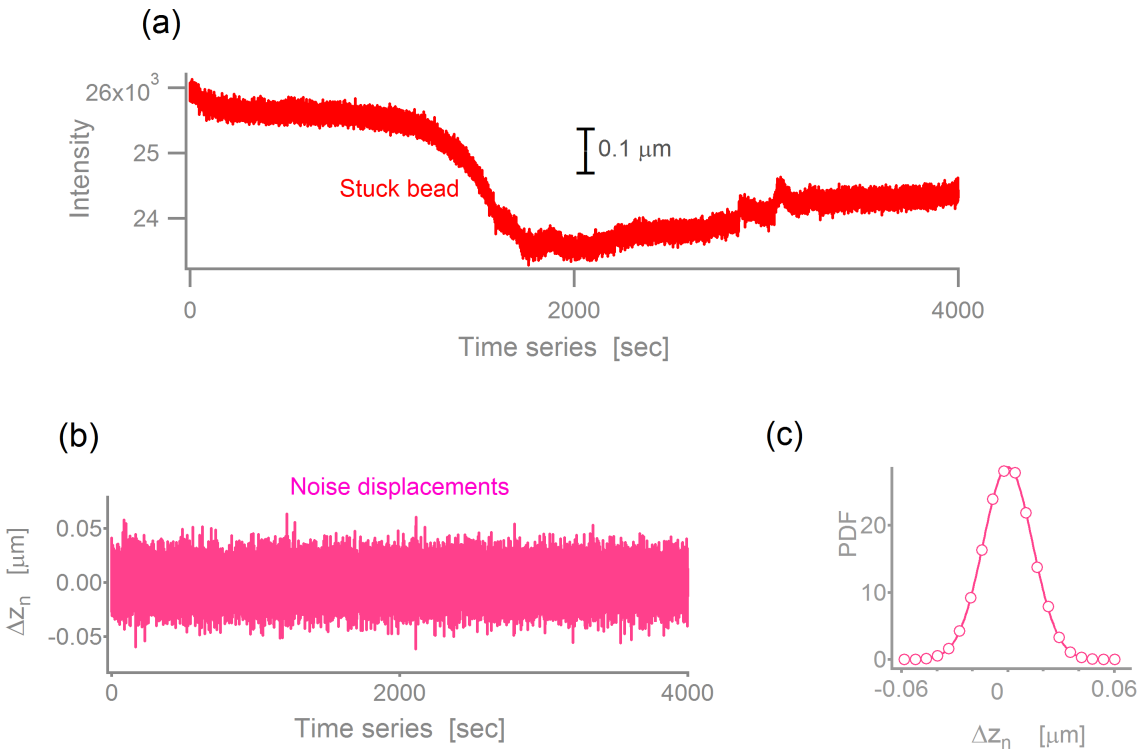

Figure 4.9: The intensity of a 5 μm latex bead stuck at the microscope slide. (a) The intensity values drift with time. (b) The measurement noise position displacements from intensity displacements. (d) Histogram of the noise displacements ($\sigma_{\Delta z} \approx 0.018 \pm 0.0002$ μm $\implies$ $\sigma_z = 0.0018/\sqrt{2}$ μm $= 0.012$ μm)

bead, controlling its vertical distance from the objective, while the Brownian bead's z-position was determined from the intensity difference between the two beads. We kept the two beads at the right side of the intensity profile, as illustrated in Fig. 4.10(b). This ensured that none of the beads had positions on the other side of the profile, which would lead to ambiguity in the bead's position, as the profile is almost symmetric at the peak. The intensity values of the stuck bead then should always be larger than those of the Brownian bead.

Practically, the Brownian bead would diffuse over the region fitted by the green curve in Fig. 4.10(b), which is not perfectly linear. To correctly determine the separation between the beads from the intensity values, we could fit a nonlinear function (from the green curve) for the measured intensity values. However, in our experiments, we mainly used larger beads, of radius $a = 2.5$ μm, where the maximum vertical separation between the two beads was $z_{\max} \approx 1.5$ μm. Hence, both beads would fall within the linear region of the intensity profile (shown as dotted black line in Fig. 4.10). We used a linear fit to convert intensities to actual separation distances between the beads. The systematic error from ignoring nonlinearities is proportional to the beads' separation distance z. At the maximum height ($z_{\max} \approx 1.5$ μm), the maximum error

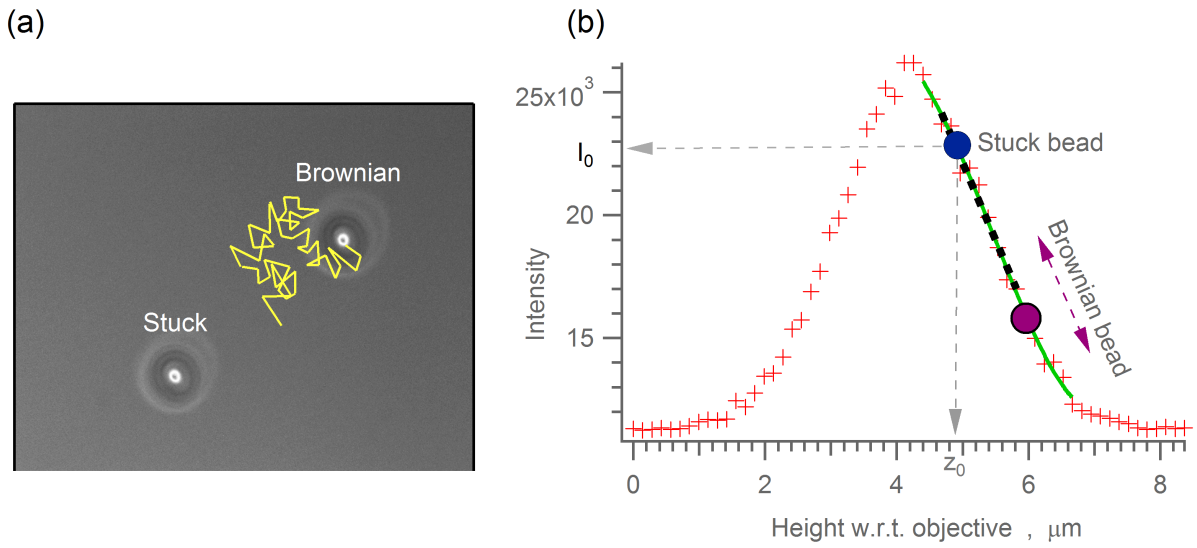

Figure 4.10: (a) Image of a stuck bead and a Brownian bead. (b) The beads on the intensity profile. The stuck bead was kept at height z_0 by a feedback loop, while the Brownian bead diffused above the stuck bead.

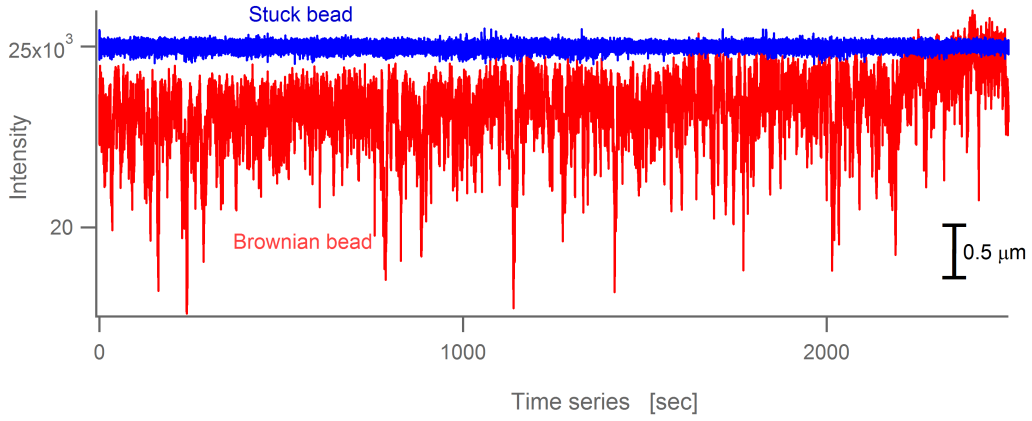

Figure 4.11: Intensity readings for a feedback-controlled stuck bead (blue) and a Brownian bead (red).

$\sigma_{\max} \approx 0.1$ μm. At the most-probable height $z_{\mathrm{mp}} \approx 0.4$ μm, $\sigma_{\mathrm{mp}} \approx 0.001$ μm. The error vanishes at $z = 0$. The uncertainty at z_{mp} was negligible. Clearly, using the slope b in our calibration had less effect on our measurements. The uncertainty at large z could be ignored since measurement accuracy is more important at small heights, and the bead spent less time at large heights.

Figure 4.11 shows the intensity values recorded for the stuck bead and the Brownian bead

of size 5 μm. We used the feedback loop to control the z-position of the stuck bead, which was controlled about a setpoint of $I_0 = 25,000$.

Correcting background illumination variations

Because the Brownian bead was always more out of focus than the stuck bead (see Fig. 4.10), it scattered less light. However, we notice from Fig. 4.11 that, after a long time, the Brownian bead sometimes was brighter than the stuck bead. We attribute this to uneven background illumination, as shown in Fig. 4.12. The intensity variation was mostly due to the microscope light source, which was brighter at the center of the image than at the edges.

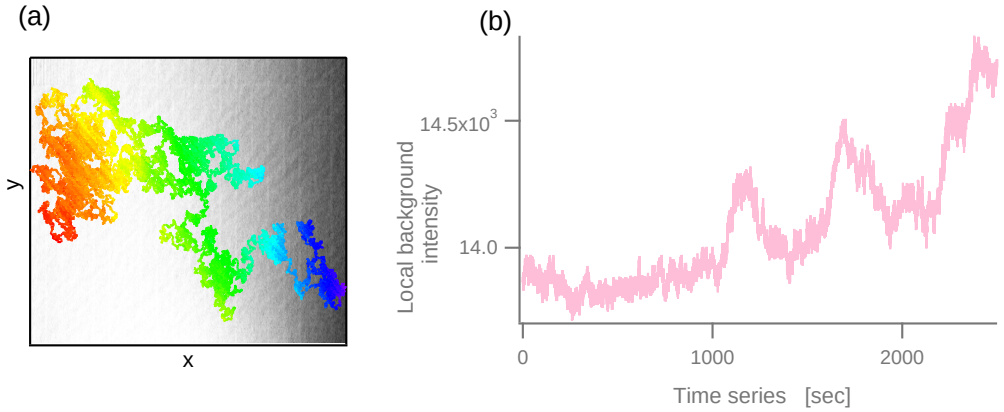

Figure 4.12: Non-uniform background illumination. (a) The Brownian bead motion on the xy-plane with uneven background illumination (The colors indicate changes in the local intensity as the bead diffuses). (b) The local background intensity over the bead's motion. (This data is from the same measurements as presented in Fig. 4.11).

To correct for uneven illumination, we took a background image from an average of 500 images with no bead in the field of view. This procedure was done before and repeated after the Brownian bead measurements were taken, to ensure that the background image stayed uniform throughout the experiment. Then the Brownian bead intensity was divided pixel by pixel by the corresponding intensity of the background image.

The light-source intensity would fluctuate, affecting the vertical position measurements of the bead. We corrected for this by recording the intensity of the illumination using a photodiode[13] (see Fig. 4.1). We then normalized by the measured illumination intensity. We reduced fluctuations in the illumination by building a box (black, lightweight panels used) over the microscope to block unwanted ambient light. The improvements due to blocking unwanted light can be seen in Fig. 4.13.

[13]PDA100A Si Amplified detector 400-1100 nm, Thorlabs Inc., Newton NJ, USA.

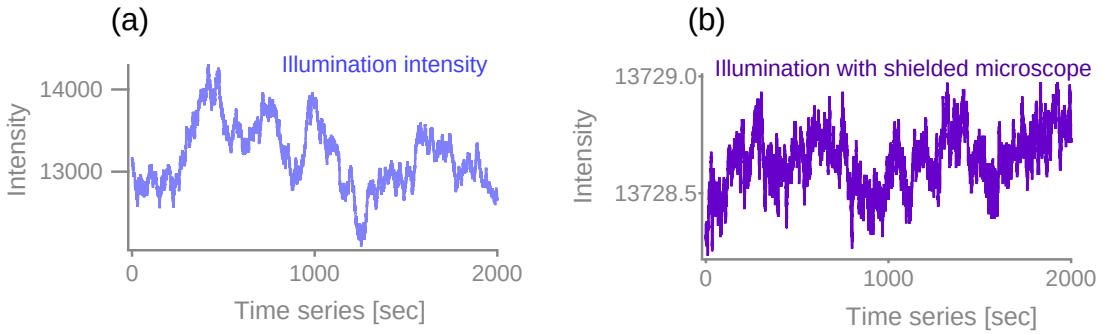

Figure 4.13: (a) Bead intensity as measured by the unshielded apparatus. (b) Reduced intensity noise for a shielded microscope setup. Note the 2000x decrease in scale.

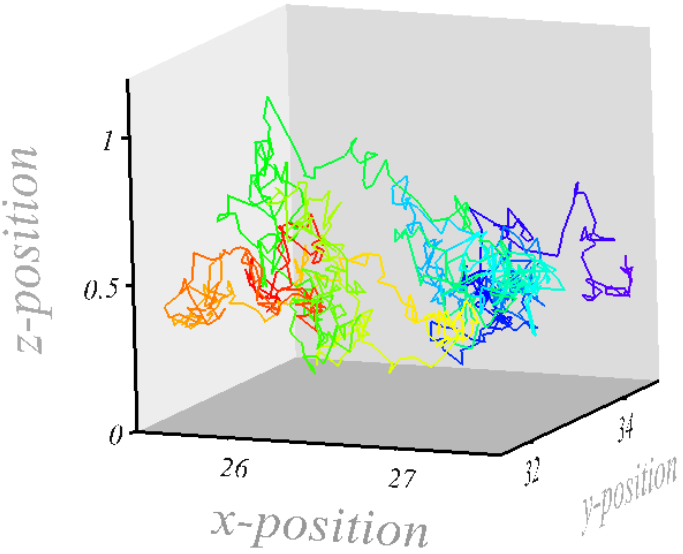

Figure 4.14: A portion (total time = 50 s) of the three-dimensional trajectory of the bead from experiment. The coloring of the trajectory represents time elapsed (all distances in μm).

4.2.3 Results

Let I_s, I_B, I_{back} and I_{ill} denote the stuck bead intensity, the Brownian bead intensity, the image background intensity, and the illumination intensity (from the photodiode), respectively. The position of the Brownian bead with respect to the stuck bead was then determined by

$$z_B = \frac{(I_s - I_B)}{b} \frac{1}{\tilde{I}_{\text{back}} \tilde{I}_{\text{ill}}}, \tag{4.2}$$

where $\tilde{I}_{\text{back}} = I_{\text{back}} / \langle I_{\text{back}} \rangle$ and $\tilde{I}_{\text{ill}} = I_{\text{ill}} / \langle I_{\text{ill}} \rangle$. The averages $\langle I_{\text{back}} \rangle$ and $\langle I_{\text{ill}} \rangle$ were taken over the neighborhood of intensity points (≈ 500 points) at which the corresponding intensities (I_{back} and I_{ill}) were evaluated. The slope b is taken from the linear feedback region of the

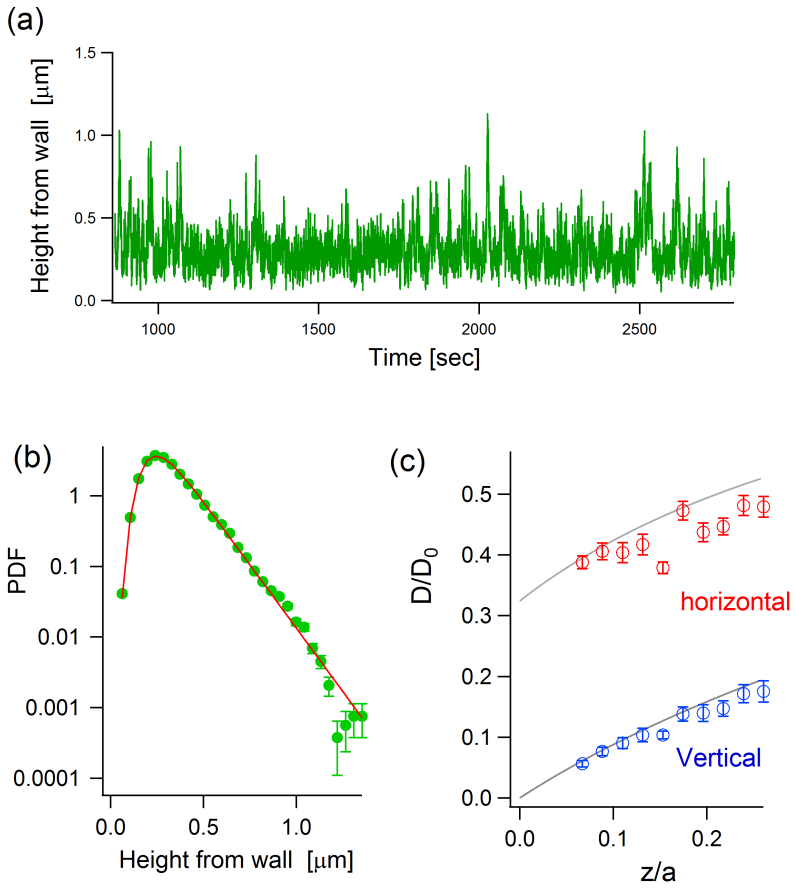

Figure 4.15: Experimental results. (a) A portion of the time series of bead heights. (b) The height distribution of the bead. Error bars represent the standard error. (d) Variation of the bead's horizontal and vertical diffusivity with height from, compared with theoretical curves. [Bead radius = 2.471 ± 0.004 μm, $\Delta t = 0.033$ s, N=119, 645 data points, total time = 3948 s.]

intensity profile. This was applied for situations where the separation between the two beads does not get very large. This worked well for 2.5 μm beads, which have a small gravitational decay length.

A portion of the bead's three-dimensional trajectory is shown in Fig. 4.14. Figure 4.15(a) shows part of the bead's trajectory along z. The distribution of heights is shown in Fig. 4.15(b). The solid line was obtained by fitting the distribution to the Boltzmann function (Eq. 2.26) taking into account the double-layer and the gravitational potentials. The variation of the bead's diffusivity with height from the wall is shown in 4.15(c). The diffusion coefficients are measured by conditional displacements Δz in a narrow interval (≈ 0.1 μm) centered on height z above the substrate. To compare our results with theory, we considered the uncertainty in the bead radius that was introduced by size variation in the latex beads. The other independent variable, temperature, could slowly vary over time due to changes in room temperature or fluctuations in

	l_g [μm]	l_D [μm]	$\frac{B}{k_BT}$
Experimental	0.1211 ± 0.0006	0.0767 ± 0.0007	15.2 ± 0.2
Theoretical	0.11 ± 0.02	–	–

Table 4.1: Values obtained for experimental parameters compared with theoretical values based on experimental material parameters.

illumination intensity. In addition, the temperature variation would affect the viscosity of water, which is a known function of temperature. Given this function, a temperature uncertainty of 1^oC would create a 2% uncertainty in the viscosity [50]. Table 4.1 shows the parameters obtained from the experiment, compared to theoretical values. To calculate the range of theoretical values, we used the bead radius $a = 2.5 \pm 0.1$ μm (as given by the manufacturer), temperature $T = 299 \pm 1$ K, bead density 1.055 ± 0.003 g/cc, and the dynamic viscosity of water $\eta = (0.88 \pm 0.02) \times 10^{-3}$ N s/m^2 (corresponding to measured $T = 298.5K$). The double-layer strength B/kT, the Debye length l_D and gravitational decay length l_g were obtained from fitting the height distribution with the Boltzmann function [see Fig 4.15(b)]. The range of expected values was primarily limited by the uncertainty in the size of the bead. Since the uncertainty in the measured value of l_g is less than the a priori uncertainty calculated from the range of sizes of the bead, we decided to use the measured Boltzmann distribution to estimate the size of each bead studied in the experiment.

4.3 Displacements and the diffusing-diffusivity dynamics

The bead's displacements Δx_n were obtained by subtracting successive positions. The minimum displacements obtained correspond to the minimum time resolution of our experiment, which is $\Delta t_{\text{exp}} = 0.033$ s. For longer time intervals $\Delta t > \Delta t_{\text{exp}}$, we picked those data points with the temporal spacing $\Delta t/\Delta t_{\text{exp}}$. Hence, $\Delta x_n = x_{i+n} - x_i = \Delta x(n\Delta t_{\text{exp}})$. To study the dynamics at long times, we needed a large number of data points to reduce noise from statistical error.

Typical horizontal displacements for the time intervals $\Delta t = 0.033$ s, 0.066 s, and 0.33 s are shown in Fig. 4.16, which are nearly Gaussian at all time scales. Figure 4.17 shows vertical displacements and their distributions, and all distributions were found to be non-Gaussian. Our goal was to see if these non-Gaussian dynamics could be seen in the diffusing-diffusivity regime identified in simulations.

4.3.1 Diffusing-diffusivity dynamics results

From 14 separate runs with different spheres (all having $a \approx 2.5\mu$m), we collected time series of position measurements to investigate non-Gaussian diffusing-diffusivity dynamics.

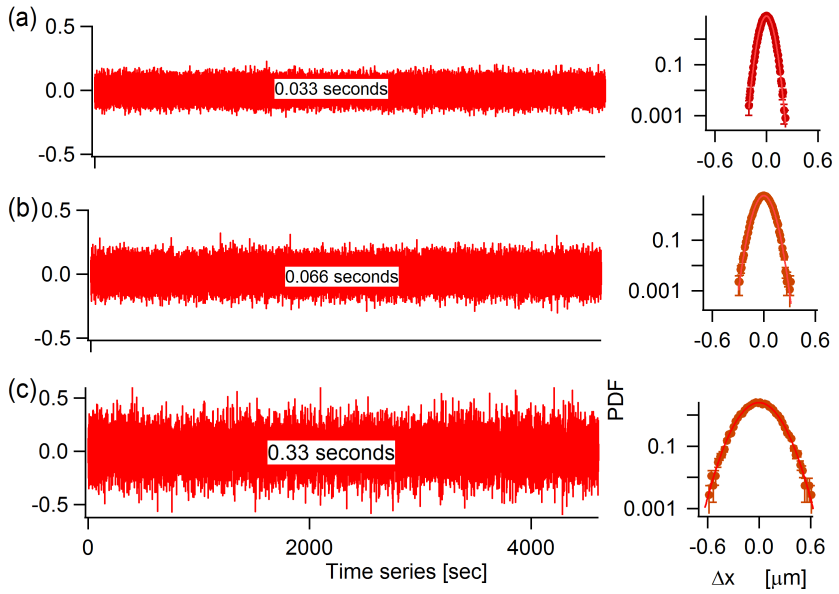

Figure 4.16: Horizontal displacements for (a) $\Delta t = 0.033$ s, (b) $\Delta t = 0.066$ s, and (c) $\Delta t = 0.33$ s. Corresponding displacement distributions are shown on the right column. Solid curves show results of Gaussian fits. Error bars come from the standard error for Poisson counting ($\sqrt{N}$). [These are from Run 10 in Table 4.2: Bead radius = 2.531 ± 0.004 μm, N=139, 716 data points, Total time = 4610 s]

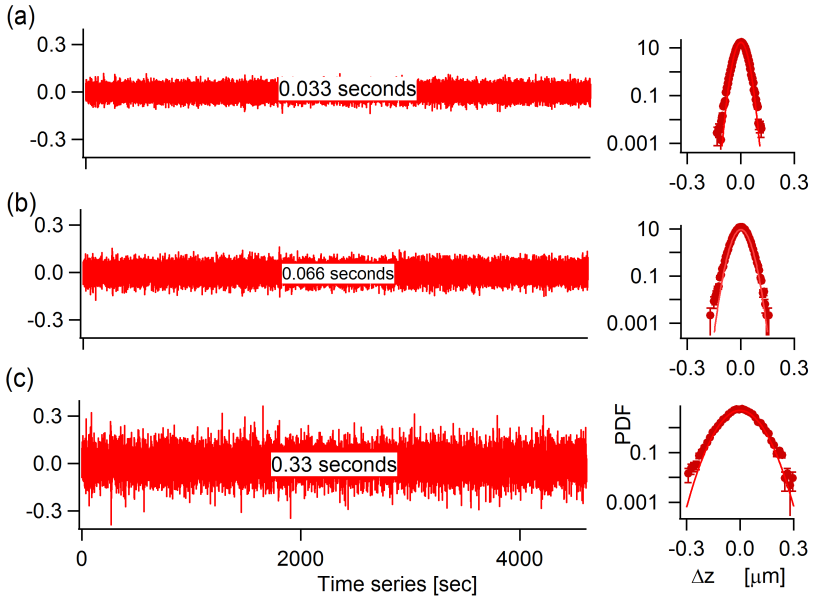

Figure 4.17: non-Gaussian vertical displacements corresponding to Fig. 4.16

We first looked at the mean-squared displacement (MSD) of the bead at different time scales

Run	N	l_g [μm]	l_D [μm]	$\frac{B}{k_BT}$	a [μm]	D_0 [$\mu m^2/s$]
1	68 966	0.1194(8)	0.0763(9)	14.7(2)	2.482(5)	0.087(3)
2	71 628	0.1185(8)	0.0793(9)	14.5(2)	2.488(6)	0.087(3)
3	100 394	0.1160(6)	0.0745(7)	16.0(2)	2.506(4)	0.086(2)
4	119 155	0.1209(6)	0.0818(8)	13.3(1)	2.472(4)	0.087(2)
5	123 603	0.1147(6)	0.0829(7)	14.2(1)	2.515(4)	0.087(2)
6	62 869	0.1157(8)	0.071(9)	15.9(2)	2.513(6)	0.087(3)
7	38 763	0.127(1)	0.075(1)	14.4(2)	2.467(7)	0.087(3)
8	34 892	0.104(1)	0.078(1)	13.9(2)	2.591(9)	0.086(3)
9	80 065	0.1169(7)	0.0782(8)	14.4(1)	2.499(5)	0.087(2)
10	139 716	0.1126(5)	0.0830(7)	14.0(1)	2.531(4)	0.087(2)
11	119 645	0.1211(6)	0.0767(7)	15.2(2)	2.471(4)	0.087(2)
12	82 324	0.1183(7)	0.0745(8)	14.7(2)	2.490(5)	0.087(2)
13	54 923	0.1053(8)	0.083(1)	15.2(2)	2.588(6)	0.087(3)
14	51 932	0.1054(8)	0.083(1)	15.4(2)	2.587(7)	0.087(3)
Mean	82 947	0.1151(5)	0.079(4)	14.82(7)	2.51(4)	0.087(2)

Table 4.2: Values obtained for experimental parameters from 14 different runs. N is the number of data points. The radius a is approximated using the measured temperature $T = 298.5K$, the latex bead density $\rho_{\rm b} = 1.055$ g/cc. and the l_g values found.

(normalized by l_g^2/D_0, where average values of l_g and D_0 were used). The results are shown in Fig. 4.18 for a single trajectory of duration ≈ 80 minutes, with parameters $B/k_BT = 14.0$, $l_g = 0.112$ μm and $l_d = 0.083$ μm. For horizontal motion, the MSD is linear with time for all explored time scales. For vertical diffusion, the mean-squared displacement curve is linear at short time scales, corresponding to the diffusing-diffusivity regime [see Fig. 4.18(b)], and it is nonlinear after $D_0\Delta t/l_g^2 \approx 5$ due to the bounding potential. At very large time scales, the MSD saturates. The solid lines in Fig. 4.18 correspond to the theoretical results obtained via

$$\mathrm{MSD} = 2D_{\rm eff}\Delta t = 2\Delta t \int_{z_{\rm min}}^{z_{\rm max}} P_B(z) D_{\parallel,\perp}(z) dz \ , \tag{4.3}$$

using the parameters obtained from the trajectory. The extreme heights $z_{\rm min}$ and $z_{\rm max}$ are taken from the measured positions, and their theoretical evaluations are discussed in Sec. 3.4.3.

We then explored the excess kurtosis at different time scales. Since kurtosis is calculated from the fourth moment of displacements, we faced the results obtained were too noisy. Hence, we needed lots of data points. We collected 14 sets of data for different trajectories averaging about 45 minutes (82 000 data points) each. Each set was fitted to the Boltzmann distribution to obtain 14 sets of the parameters l_g, l_d and B, ensuring that the parameter sets match and are consistent with theory. The results are summarized in Table 4.2. Notice that the standard deviation of the 14 results for all quantities is larger than the statistical uncertainty

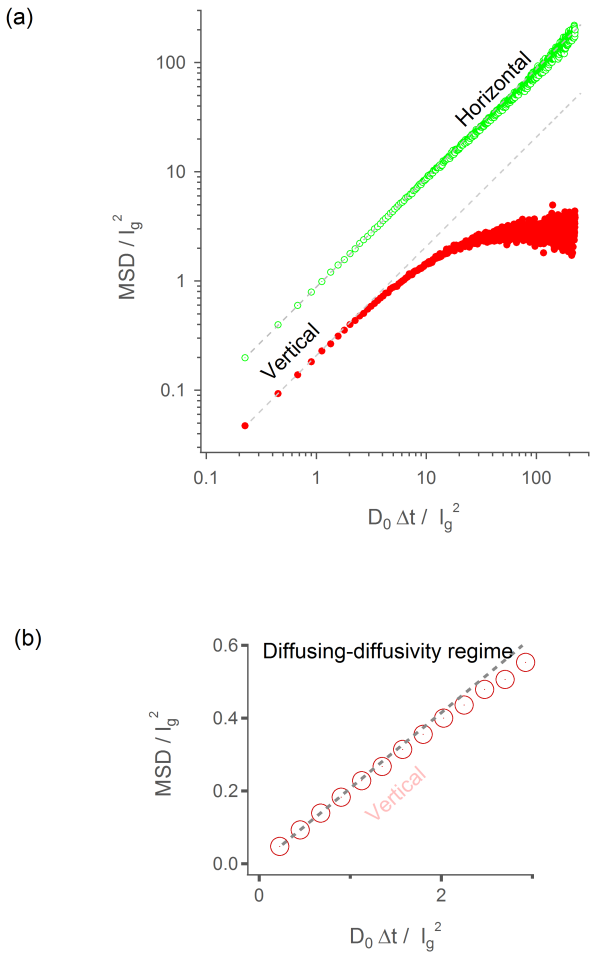

Figure 4.18: (a) Mean-squared displacements at different time scales for horizontal and vertical motion (dashed lines are theoretical results based on Eq. 4.3). (b) Short time MSD for vertical motion is nearly linear. Results are from Run 10.

of individual measurements. The added variation suggests that it arises mainly from bead-to-bead differences. Unfortunately, it was not possible in these experiments to visually distinguish between "new" and "old" beads, and it is likely that some of the runs were done on identical beads. The amount of variation seen in radius ($\approx 2\%$) is typical of manufacturer specifications for the coefficient of variation of the diameter.

The overall kurtosis was then obtained from the weighted average (weighted by the lengths of the trajectories) of the kurtosis from all the data sets. Each kurtosis curve, corresponding to each data set, was obtained as follows: Starting from N time series position measurements $z_1, z_2, \ldots, z_i, \ldots, z_N$; separated by the experimental time resolution $\Delta t_{\text{exp}} = 0.033$ s, we computed the displacements at time interval $\Delta t \equiv \Delta t_n = n\Delta t_{\text{exp}}$ using $\Delta z_n = z_{i+n} - z_i$, for $i = 0, 1, 2, \ldots, (N-n)$. These displacements were computed for each of equally spaced time in-

tervals, i.e., for $n = 1, 2, \ldots, n_{\max}$. Here, $n_{\max}$ determines the maximum time interval explored. From the resulting kurtosis vs. time calculations, we further reduced the noise by averaging neighbouring data points within successive intervals that grow logarithmically with the time scale.

The final kurtosis curves are shown in Fig. 4.19. We plotted the individual curves for the 14 different data sets; the black data points represent the weighted average from the individual curves. For vertical diffusion, we observed the two distinct time regimes: the diffusing-diffusivity and the Boltzmann regime. The transition between two regimes was at $D_0\Delta t/l_g^2 \approx 10$–$100$. Hence, for small time scales, the non-Gaussian dynamics obtained can be attributed to the fluctuations in D only. For $D_0\Delta t/l_g^2 > 100$, the non-Gaussian dynamics arises because of the bounding potential. The green lines show the theoretical kurtosis values for the diffusing-diffusivity and Boltzmann regimes predicted by Eqs. 2.52 and 2.53, respectively, given the parameters found from the experiment and their uncertainties. The results from both the diffusing diffusivity and the Boltzmann regime do match the theory. Our analysis of kurtosis leads to correlated errors in the Boltzmann regime, as demonstrated by the coherent fluctuations in asymptotic levels in individual kurtosis curves, resulting in a shift of the curve up and down in the Boltzmann regime, within the error indicated. The error is more pronounced in the Boltzmann regime. This is seen in the theory plots, where the shaded region indicates the error from the weighted standard deviation of the mean. Figure 4.19(b) shows the kurtosis for horizontal diffusion, which is almost zero at all time scales. The observed horizontal kurtosis dip at large time scales perhaps arises from insufficient statistics.

Finally, to give a direct demonstration of the diffusing-diffusivity mechanism, we sliced up the vertical positions (from run 10 in Table 4.2) of the bead into small-height intervals, of about 0.01–0.05 μm, and studied the displacement distribution in each interval. We analysed the corresponding displacements for every position measurements that begin in the particular interval. The results are shown in Fig. 4.20. We confirm the diffusing-diffusivity mechanism: The displacements are Gaussian at each interval (see the right-hand side of Fig. 4.20), while the overall distribution is non-Gaussian, as shown on the displacement distribution curve on the left side of Fig. 4.20.

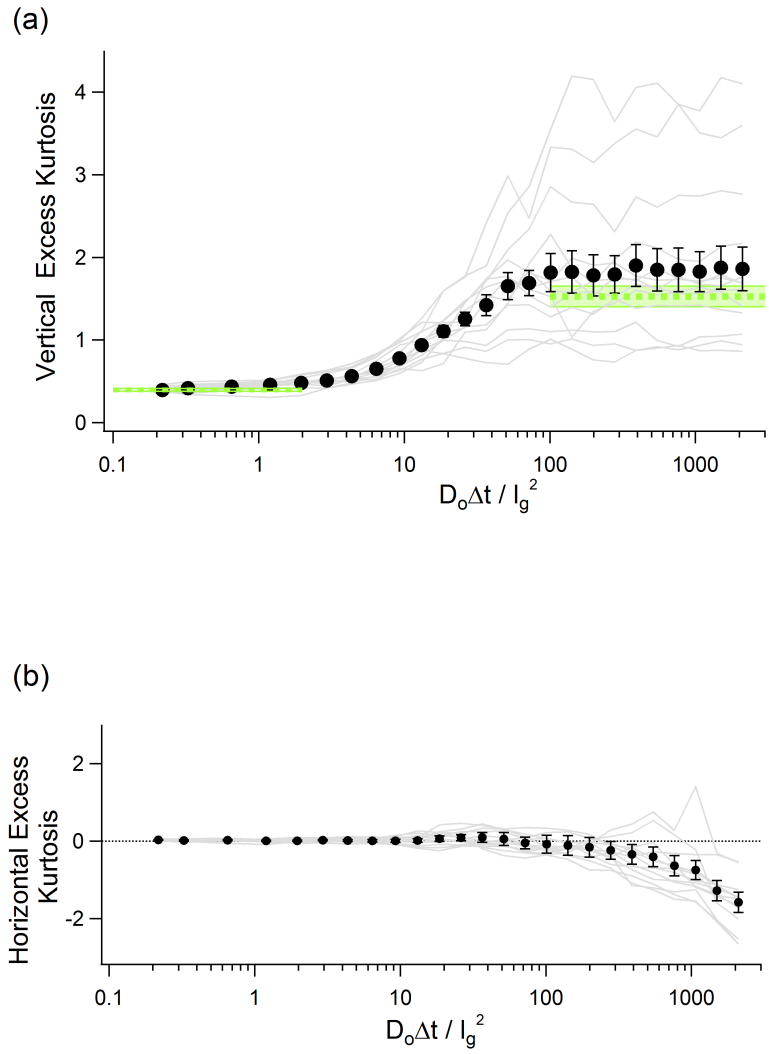

Figure 4.19: Excess kurtosis as a function of time interval for (a) vertical and (b) horizontal motion. Data points represent the average from the solid individual curves. Green dotted lines show the theoretical values. Error bars were obtained from the standard deviation of the mean (weighted by the amount of data for each trajectory).

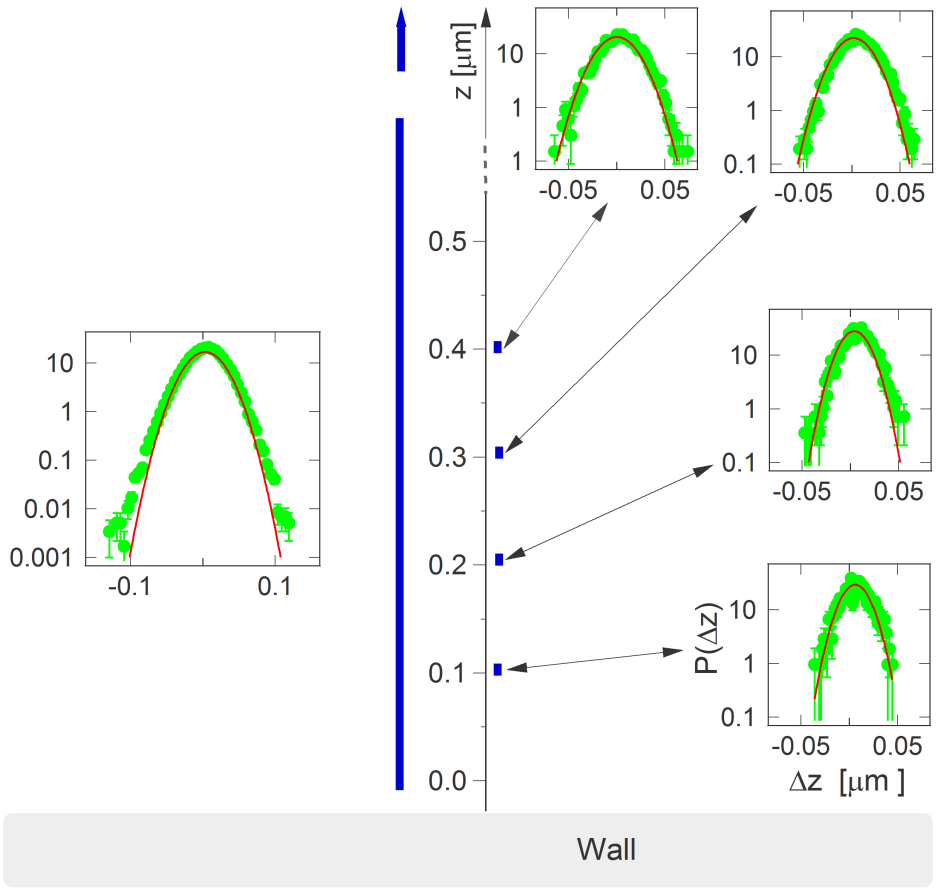

Figure 4.20: Displacements at intervals of ≈ 0.02 μm close to the wall. The right side shows the nearly Gaussian height conditional distributions, taken from the narrow range of heights indicated by the short vertical blue bars. The left side shows the non-Gaussian distribution from all heights explored by the bead.

Chapter 5

Conclusion

In this thesis, we investigated experimentally the Brownian motion of colloidal spheres near a wall. We showed that the mean-squared displacements can grow linearly with time and the displacements can be non-Gaussian distributed because of fluctuations in the diffusion coefficient D. This behavior has been previously observed in complex environments, where the form of D is unknown. In our near-wall-diffusion system, however, the spatial variation of D is known.

We first modeled the system by the overdamped Langevin equation, under the influence of the gravitational and double-layer forces in the vertical direction, and we ran simulations to understand the dynamics expected in experiments. We found that horizontal displacements are nearly Gaussian at all time scales, and vertical displacements were always non-Gaussian. The non-Gaussian dynamics in the vertical motion was attributed to two effects: the bounding potential and D fluctuations. Based on the mean-squared displacements, we classified the diffusion process into two main time regimes: the diffusing-diffusivity regime, at very small time scales where the dynamics is dominated by Brownian diffusion, and the Boltzmann regime, at long time scales where the bounding potential dominates.

In our work, we were more interested in the diffusing-diffusivity regime, where the non-Gaussian dynamics observed is a result of the diffusivity fluctuations only, and the dynamics should be at time scales small enough that it does not feel the potential. From simulations, we observed that controlling the shape of the potential, by varying parameters such as the particle size and the Debye length, changes the nature of the displacement distribution curves. We showed that the right combination of parameters can maximize the non-Gaussianity (as measured by excess kurtosis) of the distributions. This optimum is realized when the range of fluctuations in D is maximized. Based on the simulation results, we chose the right size of the bead that optimizes fluctuations in D and gives the diffusing-diffusivity dynamics at the smallest time resolution of our experiment ($\Delta t = 0.033$ s).

We then implemented experimentally a feedback tracking system, where a piezo vertical stage follows the bead's vertical motion. Our experimental results agreed with simulations. By

fitting the height distribution to the Boltzmann function, we obtained parameters that agree with theory. We confirmed the diffusing-diffusivity mechanism proposed by Chubynsky et al [22]: We obtained non-Gaussian displacements coexisting with mean-squared displacements that grow linearly with time. The conditional distributions at small heights from the wall were seen to exhibit nearly Gaussian dynamics.

The experimental investigations presented in this thesis have several possible future perspectives. Instead of studying rigid spheres, we could study the motion of fluctuating biomolecules, such as DNA, near a wall. The displacements for such molecules would then be explored. The experiment could be further improved for precise measurement of vertical positions using, for instance, digital holographic microscopy, that has extended depth of field [25]. An understanding of near-wall Brownian motion is important for its technological and biological relevance. The behavior of biomolecules diffusing near boundaries will determine their macroscopic properties and impact their biological functions, such as collective motion of sperm cells near interfaces [51] and swimming bacteria in thin films [52]. Near-wall flows of colloidal suspensions are also ubiquitous in industrial processes from food processing to petrol recovery [53].

Bibliography

[1] Robert Brown. A brief account of microscopical observations made in the months of June, July and August 1827, on the particles contained in the pollen of plants; and on the general existence of active molecules in organic and inorganic bodies. *Philos. Mag. Lett.*, 4:161–173, 1828.

[2] Albert Einstein. On the theory of the Brownian movement. *Annalen der Physik*, 4:371–381, 1906.

[3] John S Rigden. *Einstein 1905: The standard of Greatness*. Harvard University Press, 2005.

[4] Marian von Smoluchowski. *Sur le chemin moyen parcouru par les molécules d'un gaz et sur son rapport avec la théorie de la diffusion* (On the mean path of molecules of gas and its relationship to the theory of diffusion), *Bulletin International de l'Académie des Sciences de Cracovie*. pages 202–213, 1906.

[5] J Perrin. Brownian movement and molecular reality. 1910.

[6] Robert M Mazo. *Brownian Motion: Fluctuations, Dynamics, and Applications*, volume 2. Clarendon press Oxford, 2002.

[7] Norbert Wiener. *Selected Papers of Norbert Wiener: Including Generalized Harmonic Analysis and Tauberian Theorems*. MIT Pr., 1965.

[8] Daniel Thomas Gillespie and Effrosyni Seitaridou. *Simple Brownian Diffusion: An Introduction to the Standard Theoretical Models*. Oxford University Press, 2012.

[9] Mark G Raizen and Tongcang Li. The measurement Einstein deemed impossible. *Phys. Today*, 68:56–57, 2015.

[10] Simon Kheifets, Akarsh Simha, Kevin Melin, Tongcang Li, and Mark G Raizen. Observation of brownian motion in liquids at short times: Instantaneous velocity and memory loss. *Science*, 343:1493–1496, 2014.

[11] Iva Marija Tolić-Nørrelykke, Emilia-Laura Munteanu, Genevieve Thon, Lene Oddershede, and Kirstine Berg-Sørensen. Anomalous diffusion in living yeast cells. *Phys. Rev. Lett.*, 93:078102, 2004.

[12] Stas Burov, Jae-Hyung Jeon, Ralf Metzler, and Eli Barkai. Single particle tracking in systems showing anomalous diffusion: the role of weak ergodicity breaking. *Phys. Chem. Chem. Phys.*, 13:1800–1812, 2011.

[13] Jean Farago, Hendrik Meyer, and AN Semenov. Anomalous diffusion of a polymer chain in an unentangled melt. *Phys. Rev. Lett.*, 107:178301, 2011.

[14] Igor M Sokolov. Models of anomalous diffusion in crowded environments. *Soft Matter*, 8:9043–9052, 2012.

[15] Ralf Metzler and Joseph Klafter. The random walk's guide to anomalous diffusion: A fractional dynamics approach. *Phys. Rep.*, 339:1–77, 2000.

[16] Giuseppe Forte, Fabio Cecconi, and Angelo Vulpiani. Non-anomalous diffusion is not always Gaussian. *Eur. J. Phys. B*, 87:1–9, 2014.

[17] Gyemin Kwon, Bong June Sung, and Arun Yethiraj. Dynamics in crowded environments: Is non-Gaussian Brownian diffusion normal? *J. Phys. Chem. B*, 118:8128–8134, 2014.

[18] Bo Wang, Stephen M Anthony, Sung Chul Bae, and Steve Granick. Anomalous yet Brownian. *PNAS*, 106:15160–15164, 2009.

[19] Bo Wang, James Kuo, Sung Chul Bae, and Steve Granick. When Brownian diffusion is not Gaussian. *Nat. Mater.*, 11:481–485, 2012.

[20] Juan Guan, Bo Wang, and Steve Granick. Even hard-sphere colloidal suspensions display fickian yet non-Gaussian diffusion. *ACS Nano*, 8:3331–3336, 2014.

[21] Sukanya Bhattacharya, Dharmendar Kumar Sharma, Saumya Saurabh, Suman De, Anirban Sain, Amitabha Nandi, and Arindam Chowdhury. Plasticization of Poly (vinylpyrrolidone) thin films under ambient humidity: Insight from single-molecule tracer diffusion dynamics. *J. Phys. Chem. B*, 117:7771–7782, 2013.

[22] Mykyta V Chubynsky and Gary W Slater. Diffusing diffusivity: A model for anomalous, yet Brownian, diffusion. *Phys. Rev. Lett.*, 113:098302, 2014.

[23] Arindam Banerjee and Kenneth D Kihm. Experimental verification of near-wall hindered diffusion for the Brownian motion of nanoparticles using evanescent wave microscopy. *Phys. Rev. E*, 72:042101, 2005.

[24] John Happel and Howard Brenner. *Low Reynolds Number Hydrodynamics: With Special Applications to Particulate Media*, volume 1. Springer Science & Business Media, 1983.

[25] Prerna Sharma, Shankar Ghosh, and S Bhattacharya. A high-precision study of hindered diffusion near a wall. *Appl. Phys. Lett.*, 97:104101, 2010.

[26] Hannes Risken. *The Fokker-Planck Equation. Methods of Solution and Applications.* Springer Series in Synergetics, 1989.

[27] Yuncheng Liang, Nidal Hilal, Paul Langston, and Victor Starov. Interaction forces between colloidal particles in liquid: Theory and experiment. *Adv. Colloid Interface Sci.*, 134:151–166, 2007.

[28] David S Sholl, Michael K Fenwick, Edward Atman, and Dennis C Prieve. Brownian dynamics simulation of the motion of a rigid sphere in a viscous fluid very near a wall. *J. Chem. Phys.*, 113:9268–9278, 2000.

[29] Michael A Bevan and Dennis C Prieve. Hindered diffusion of colloidal particles very near to a wall: Revisited. *J. Chem. Phys.*, 113:1228–1236, 2000.

[30] Jacob N Israelachvili. *Intermolecular and Surface Forces*. Academic press, 2011.

[31] Nicolaas Godfried Van Kampen. *Stochastic Processes in Physics and Chemistry*, volume 1. Elsevier, 1992.

[32] Crispin Gardiner. *Stochastic methods*. Springer Berlin, 2009.

[33] Andy WC Lau and Tom C Lubensky. State-dependent diffusion: Thermodynamic consistency and its path integral formulation. *Phys. Rev. E*, 76:011123, 2007.

[34] Jose M Sancho. Brownian colloidal particles: Ito, Stratonovich, or a different stochastic interpretation. *Phys. Rev. E*, 84:062102, 2011.

[35] Oded Farago and Niels Grønbech-Jensen. Langevin dynamics in inhomogeneous media: Re-examining the Itô-Stratonovich dilemma. *Phys. Rev. E*, 89:013301, 2014.

[36] Ryzhik Gradshteyn. Table of Integrals, Series, and Products (Seventh Edition), 2007.

[37] Mauricio D Carbajal-Tinoco, Ricardo Lopez-Fernandez, and José Luis Arauz-Lara. Asymmetry in colloidal diffusion near a rigid wall. *Phys. Rev. Lett.*, 99:138303, 2007.

[38] Jim C Chen and Albert S Kim. Brownian dynamics, molecular dynamics, and Monte Carlo modeling of colloidal systems. *Adv. Colloid Interface Sci.*, 112:159–173, 2004.

[39] Henry C Thode. *Testing for Normality*, volume 164. CRC press, 2002.

[40] Laurens De Haan and Ana Ferreira. *Extreme Value Theory: An Introduction*. Springer Science & Business Media, 2007.

[41] EJ Gumbel. *Statistics of Extremes*. Columbia Univ. Press, New York, 1958.

[42] Yonggun Jun and John Bechhoefer. Virtual potentials for feedback traps. *Phys. Rev. E.*, 86:061106, 2012.

[43] Momčilo Gavrilov, Yonggun Jun, and John Bechhoefer. Real-time calibration of a feedback trap. *Rev. Sci. Instrum.*, 85:095102, 2014.

[44] Chungil Ha, HD Ou-Yang, and Hyuk Kyu Pak. Direct measurements of colloidal hydrodynamics near flat boundaries using oscillating optical tweezers. *Physica A*, 392:3497–3504, 2013.

[45] Adam S Backer and WE Moerner. Extending single-molecule microscopy using optical fourier processing. *J. Phys. Chem. B*, 118:8313–8329, 2014.

[46] Michael A Thompson, Jason M Casolari, Majid Badieirostami, Patrick O Brown, and WE Moerner. Three-dimensional tracking of single mRNA particles in Saccharomyces cerevisiae using a double-helix point spread function. *PNAS*, 107:17864–17871, 2010.

[47] Michael Speidel, Alexandr Jonáš, and Ernst-Ludwig Florin. Three-dimensional tracking of fluorescent nanoparticles with subnanometer precision by use of off-focus imaging. *Opt. Lett.*, 28:69–71, 2003.

[48] Lukas Schertel. Development of a 3D feedback trap for colloidal particles and biological molecules. Bachelor's thesis, Simon Fraser Univ./Univ. of Konstanz, 2012.

[49] Paul Omelchenko. 3D feedback colloidal tracking method to measure hindered diffusion. Bachelor's thesis, Simon Fraser Univ., 2014.

[50] Marco A Catipovic, Paul M Tyler, Josef G Trapani, and Ashley R Carter. Improving the quantification of Brownian motion. *Am. J. Phys.*, 81:485–491, 2013.

[51] Ingmar H Riedel, Karsten Kruse, and Jonathon Howard. A self-organized vortex array of hydrodynamically entrained sperm cells. *Science*, 309:300–303, 2005.

[52] Andrey Sokolov, Igor S Aranson, John O Kessler, and Raymond E Goldstein. Concentration dependence of the collective dynamics of swimming bacteria. *Phys. Rev. Lett.*, 98:158102, 2007.

[53] William B Russel, Dudley A Saville, and William R Schowalter. *Colloidal Dispersions*. Cambridge University Press, 1992.